UiT The Arctic University of Norway

Faculty of Science and Technology
Department of Physics and Technology

Frequency Dependence of Ionospheric Electron Heating Around the Third Double Resonance

Ingeborg Frøystein

FYS-3931 Master's Thesis in Space Physics 30 SP
June 2022

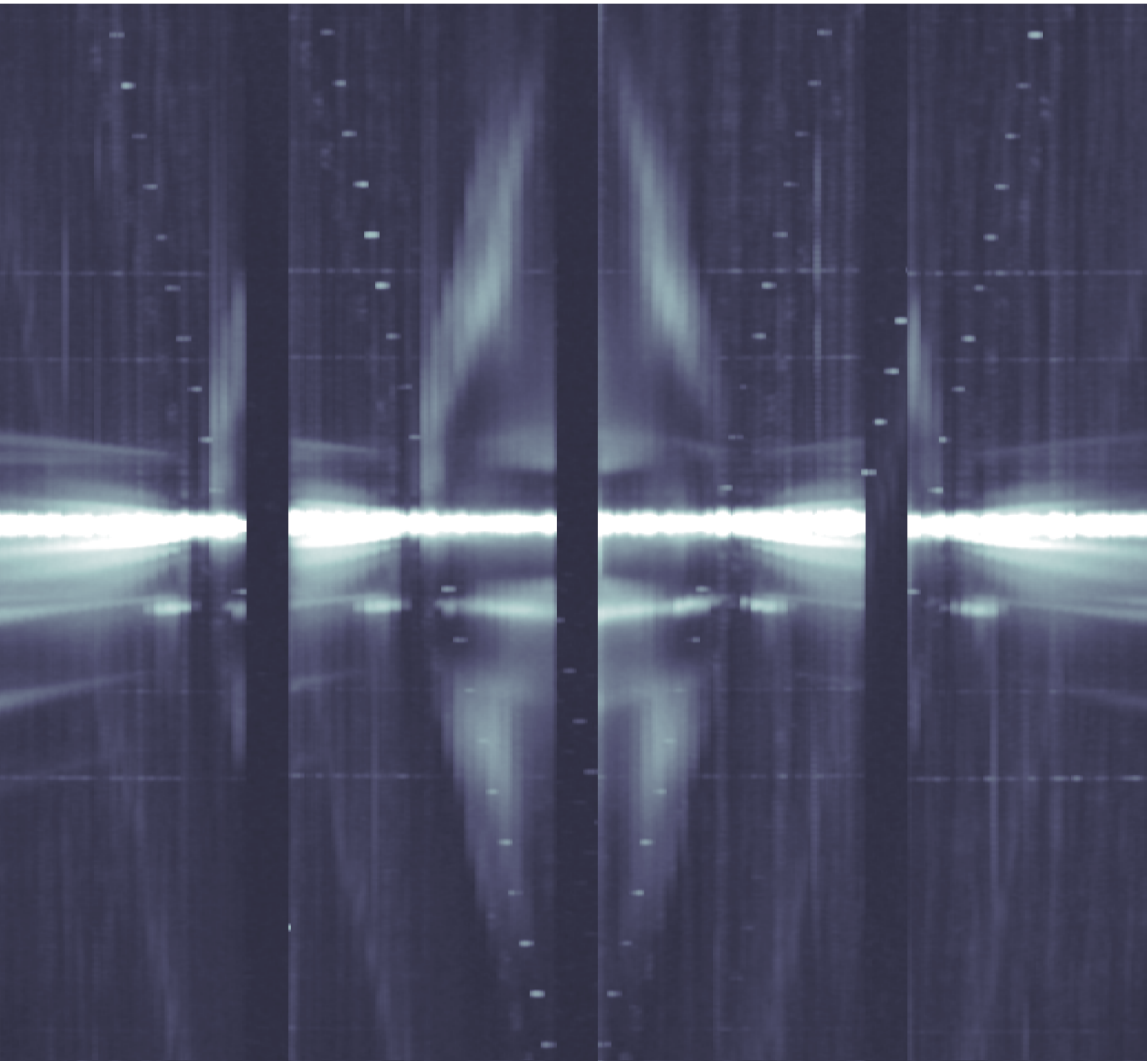

The front page shows an excerpt from an exceptionally beautiful SEE spectrogram from an EISCAT Heating experiment done on the 8th of October 2021. Full spectrograms are presented in chapter 4.

Abstract

The partly ionized ionosphere responds differently to high power, high frequency radio waves based on the wave frequency, the wave power, the wave polarization, and the propagation angle relative to the magnetic field. Ionospheric modification experiments are conducted to investigate the responses and their dependencies, setting experimental constraints on the contributions from non-resonant collisional interactions and resonant wave-plasma processes. The objective of the work detailed in this thesis was to examine the time and altitude variation of ionospheric electron heating around the third double resonance frequency, that is where the HF pump frequency matches the Upper Hybrid frequency as well as the third multiple of the electron gyration frequency, and determine possible hysteresis effects as the HF pump wave frequency is stepped up or down through the third double resonance. This thesis presents three new EISCAT Heating experiments where the frequency is stepped in 4.79 kHz steps up and down through the third double resonance frequency, which varied on the interval $[4.151, 4.187]$ MHz during the three experiments. Electron temperature enhancements of up to 2000 K were achieved. The time and altitude variation of the HF heat source were estimated by assuming parameterizations for the HF heat source and solving a simplified electron energy equation for model temperatures. The parameterizations were estimated by non-linear least squares optimization of the model temperatures against the observed temperatures for each frequency step in each pulse, yielding a set of parameters per step in frequency. Due to a high level of measurement noise in the measurements we were not able to draw firm conclusions. However, the parameter estimates show indications of possible asymmetry in the HF heat source and its parameters when the HF pump frequency is stepped up and down through the third double resonance frequency. Most notable is the indication that the hysteresis effect observed by Carozzi et al. in 2002 [8] and Najmi et al. in 2014 [28] in Broad Upshifted Maxima strength might also be present in the column integrated heating rates when stepping the HF pump frequency up and down through the third double resonance frequency.

Acknowledgements

First and foremost, I would like to thank my exceptional supervisor Professor Björn Gustavsson for introducing me to this interesting topic. Thank you for all help, guidance and feedback, and for including me in a series of exciting EISCAT Heating experiments. I have learned a lot and for that I am thankful.

I would also like to thank Juha Vierinen for helping me with the SEE and for letting me borrow some much-needed computation power for my analysis.

A big thanks is also owed to my fellow master's students for good vibes in the office, and especially to Andrea for accepting the role as my rubber duck.

Last but not least, I would like to thank my mother Anne and my father Nils Åge for proofreading this thesis on very short notice.

Contents

List of Figures

List of Tables

List of Abbreviations

ACF	Auto Correlation Function
BUM	Broad Upshifted Maxima
COH	Center Of Heating
DM	Downshifted Maxima
EB	Electron Bernstein
EISCAT	European Incoherent SCATter
ERP	Effective Radiated Power
HF	High Frequency
HFIL	High Frequency Enhanced Ion Lines
HFPL	High Frequency Enhanced Plasma Lines
IGRF	International Geomagnetic Reference Field
IRI	International Reference Ionosphere
ISR	Incoherent Scatter Radar
LT	Langmuir Turbulence
MF	Medium Frequency
MSIS	Mass Spectrometer and Incoherent Scatter radar
OTSI	Oscillating Two-Stream Instability
PDI	Parametric Decay Instability
PDS	Power Density Spectrum
RF	Radio Frequency
SDR	Software Defined Radio
SEE	Stimulated Electromagnetic Emissions
UH	Upper Hybrid
UHF	Ultra High Frequency
UHR	Upper Hybrid Resonance
UHT	Upper Hybrid Turbulence
UV	Ultraviolet
VHF	Very High Frequency

1 Introduction

The ionosphere is the partly ionized region of the Earth's upper atmosphere. It is primarily ionized by solar radiation through photoionization. At high latitudes it is also ionized through auroral particle precipitation. On the other hand, ions and electrons are lost in recombination. At all times, the ionospheric electron density is the result of the balance between ionization and recombination. The existence of the ionosphere was proved in 1924 through a study on the reflection of radio waves from the ionosphere [5]. However, the ionosphere was hypothesized as early as 1902, only one year after physicist Guglielmo Marconi's famous transatlantic radio signal transmission. Since then, significant advances have been made in both radio science and ionospheric research.

Radio waves with different frequencies and polarizations will propagate differently through the ionosphere because it is partly ionized. Further, the ionosphere itself will respond differently to interactions with these different radio waves. To study the ionospheric response to high power, high frequency (HF) radio waves, *ionospheric modification* experiments are conducted. Observations and modeling of the responses are fundamental to understanding the processes and phenomena which occur when the radio waves interact with the ionospheric plasma. One such ionospheric response is enhancements of the ionospheric electron temperature, which is the response of interest in this thesis.

Through ionospheric modification experiments several important findings have been made, in regard to the ionospheric response as a function of radio wave

power, frequency, and propagation angle to the Earth's magnetic field. First, the efficiency of ionospheric electron heating has been shown to increase with radio wave power [7]. Also, the anomalous absorption of the diagnostic signal, which is linked to resonant electron heating, exhibit hysteresis effects when increasing and decreasing the power of the HF pump wave [19, 32, 39]. Second, enhancements in electron temperature are strongest when the transmitted radio wave propagates toward magnetic zenith [16, 31]. This is also the case for the electron heating rates [16]. Third, enhancements in temperature depend strongly on the radio wave frequency offset from a *double resonance* frequency [16, 18, 20, 33], that is where the HF heating wave frequency matches both the upper hybrid frequency and a multiple of the electron cyclotron frequency. The enhancements maximize around the second double resonance [20] and minimize around the third and fourth double resonance [16, 18, 33].

Further work has been done on electron heating around the third and fourth double resonance frequency to attempt to explain the physical processes behind the enhancement minima for harmonics $n > 2$. Najmi et al. [27] successfully simulated how the electron velocity distribution depend strongly on the proximity to the fourth double resonance frequency. They show that electron heating above and below the double resonance are dominated by different wave modes. The different wave modes, upper hybrid and electron Bernstein waves, give rise to different electron velocity distributions. This clearly shows that the heating mechanisms might differ above and below the double resonance frequency.

Another important feature of the ionospheric response to HF radio wave modification around double resonance frequencies is the SEE signatures. How these signatures vary with proximity to the fourth double resonance were well illustrated by Carozzi et al. in 2002 [8]. In their experiment analysis they observed *hysteresis* effects in signature strengths when passing the double resonance frequency from above and from below. This opens an interesting question: can hysteresis effects be observed in electron heating rates when sweeping the heater frequency up and down through a double resonance frequency?

This thesis presents three new EISCAT Heating experiments conducted in October 2021. The experiments were designed to investigate the frequency dependence of ionospheric electron heating when sweeping the pump frequency up and down through the third double resonance frequency. Further, we present modeled electron heating rates and electron temperatures as a function of frequency offset from the third double resonance frequency and sweep direction. One additional experiment was conducted in March 2022. This experiment was designed to compare election heating when sweeping the pump frequency up through the third and fourth double resonance frequency. Unfortunately, this experiment was not fruitful. However, the experiments con-

ducted in October 2021 were successful, as evidence of the pump frequency passing the third double resonance frequency was found in both up-sweeps and down-sweeps.

1.1 Thesis Structure

Chapter 2 covers the necessary background theory for the experiments and analysis elaborated in this thesis.

Chapter 3 presents the 4 EISCAT Heating experiment conducted for this thesis and their designs. A presentation of the EISCAT facility is also included.

Chapter 4 presents the observations from the 4 different experiments. The observations include ionospheric parameters and SEE spectrograms.

Chapter 5 details the method used in the analysis and modeling done for this thesis. Some problems that arose and how they were solved are also presented.

Chapter 6 presents the results of the modeling and the analysis, including estimates of parameter uncertainties, following the method detailed in chapter 5.

Chapter 7 presents a summary of the work done in this thesis and some concluding remarks. Suggestions for future work on this topic are also presented.

2 Background

This chapter contains the necessary theoretical background for the experiments and the analysis detailed in this thesis. The topics include (1) plasma physics fundamentals, (2) the ionosphere, (3) electron heating and (4) incoherent scatter radar.

2.1 Plasma fundamentals

A plasma is a gas that is ionized, i.e. we have free electrons and positive ions. However, most gases are ionized to some degree. Plasmas are therefore required to fulfill several additional criteria. These criteria vary, but following [9] there are two criteria: (1) A plasma needs to be *quasineutral*. This means that there can exist local charge clusters within a plasma, but the overall charge is zero. (2) A plasma needs to exhibit *collective behavior*. This means that behavior, or movement, of a particle within the plasma depends on the behavior of the particles around it, both locally and in the plasma as a whole. This collective behavior arises from long distance Coulomb forces that are results of local electric fields within the plasma.

For this collective behavior to arise, the scale length of the plasma needs to be significantly greater than the *Debye length*. In addition, the number density of electrons within a *Debye sphere* needs to be significantly larger than one. These two conditions can be written as

$$\begin{aligned} L_p &>> \lambda_D \\ n_D &>> 1 \end{aligned} \tag{2.1}$$

where L_p is the plasma scale length, λ_D is the Debye length and n_D is the number density inside the Debye sphere. Further, for this collective behavior to be sustainable, the collision frequency must be significantly smaller than the *plasma frequency*, that is

$$\nu_{\text{coll}} << \omega_p \tag{2.2}$$

where ν_{coll} is the collision frequency and ω_p is the plasma frequency.

The Debye length, λ_D, is a characteristic length within a plasma and is the scale over which local charge densities can exist. The Debye length is therefore the radius of the *Debye sphere* surrounding a charge in the plasma. The Debye length can be derived from the one-dimensional Poisson's equation [9, 24] and further expanded to three dimensions under the assumption that the potential only varies with radial distance from the spherical central charge. The one-dimensional Poisson's equation is

$$\mathbb{PE}: \ \nabla^2\phi = -\frac{e}{\epsilon_0}(n_i - n_e) \tag{2.3}$$

where $\nabla = \frac{d^2}{d^2x}$, ϕ is the potential due to some test charge, e is the electron charge, ϵ_0 is the vacuum permittivity, n_i is the ion density and n_e is the electron density. The resulting potential ϕ as a function of a distance vector $\boldsymbol{r}$ from a spherical charge in the plasma is

$$\phi(\boldsymbol{r}) = \frac{q}{4\pi\epsilon_0|\boldsymbol{r}|}\exp\left(-\frac{|\boldsymbol{r}|}{\lambda_D}\right) \tag{2.4}$$

where $\boldsymbol{r}$ is the distance vector from the center charge, q is the charge of the center charge and λ_D is the Debye length which is defined as

$$\lambda_D = \sqrt{\frac{\epsilon_0 k_B T_e}{n_0 e^2}} \tag{2.5}$$

where k_B is the Boltzmann constant, T_e is the electron temperature and n_0 is the density.

Finally, a plasma is *fully ionized* if there only are electrons and ions, and no remaining neutral particles. The ionospheric plasma is an example of a plasma that is *partly ionized*, i.e., there are neutrals as well as ions and electrons.

2.1.1 Phase Space and The Boltzmann Equation

The Boltzmann equation describes the evolution of the *phase space density* $f_s(\boldsymbol{r}, \boldsymbol{v}, t)$ for species s as a function of position $\boldsymbol{r}$ and velocity $\boldsymbol{v}$ [34]. It is important to note that the Boltzmann equation only considers the change of the density function f_s and not single particle motion.

$$\mathbb{BE}: \ \frac{\partial f_s}{\partial t} + \boldsymbol{v}_s \cdot \boldsymbol{\nabla} f_s + \frac{\boldsymbol{F}}{m_s} \cdot \frac{\partial f_s}{\partial \boldsymbol{v}_s} = \left(\frac{\partial f_s}{\partial t}\right)_c \tag{2.6}$$

$\partial f_s / \partial t$ is the change with time in the phase space density f_s, $\boldsymbol{v}_s \cdot \boldsymbol{\nabla} f_s$ is the time dependent change in f_s due to particle drifts, $(\boldsymbol{F}/m_s) \cdot (\partial f_s / \partial \boldsymbol{v}_s)$ is the change in f_s due to acceleration from an external force and $(\partial f_s / \partial t)_c$ is the change in f_s due to collisions. The force term can be substituted by the Lorentz force under the assumption that the only forces are electromagnetic forces. The terms are illustrated for a one-dimensional phase space $f_s(x, v_x, t)$ in Figure 2.1, that is a phase space with one spatial dimension and one velocity dimension.

The Boltzmann equation is the origin for the derivation of the fluid equations in plasma. By taking the *velocity moments* of the phase space distribution function f_s equations for each moment are obtained. These moments can in general be expressed as

$$\langle \xi_s(\boldsymbol{v}_s) \rangle = \frac{1}{n_s} \int \mathrm{d}^3 v_s f_s(\boldsymbol{r}, \boldsymbol{v}_s, t) \xi_s(\boldsymbol{v}_s) \tag{2.7}$$

where $\xi_s(\boldsymbol{v}_s)$ is a function of the velocity $\boldsymbol{v}_s$ [34], n_s is the number density of species s and $\mathrm{d}^3 v_s$ is a velocity space volume element for species s.

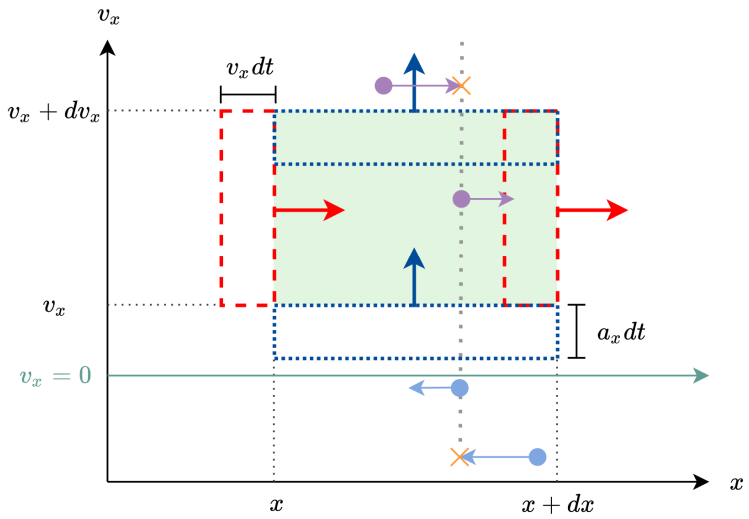

Figure 2.1: Flux in and out of phase space $f_s(t, x, v_x)$ (green); flux due to diffusion (red) and flux due to an external force (blue). The blue and purple particles show an example collision resulting in the purple particle entering $f_s(t, x, v_x)$.

2.1.2 Fluid Equations

The following descriptions of the fluid equations follow the descriptions given by Schunk and Nagy [34]. The zeroth moment of the Boltzmann equation yields the continuity equation $\mathbb{CE}_s$ for species s, which describes the change in number density,

$$\mathbb{CE}_s : \frac{\partial n_s}{\partial t} + \nabla \cdot (n_s \boldsymbol{u}_s) = \frac{\delta n_s}{\delta t} \tag{2.8}$$

where $\boldsymbol{u}_s$ is the average drift velocity for species s and $\frac{\delta n_s}{\delta t}$ is the change due to collisions, i.e. the difference between sources and losses.

Further, the first moment yields the momentum equation $\mathbb{ME}_s$ for species s which describes the change in momentum,

$$\mathbb{ME}_s : n_s m_s \left[\frac{\partial}{\partial t} + \boldsymbol{u}_s \cdot \nabla \right] \boldsymbol{u}_s + \nabla \cdot \boldsymbol{P}_s - n_s m_s \boldsymbol{G} - n_s e_s (\boldsymbol{E} + \boldsymbol{u}_s \times \boldsymbol{B}) = \frac{\delta M_s}{\delta t} \tag{2.9}$$

where m_s is the mass of species m, $\nabla \cdot \boldsymbol{P}_s$ is the pressure gradient, $\boldsymbol{G}$ is the acceleration due gravitational forces, e_s is the electron or ion charge, $\boldsymbol{E}$

is the electric field, $\boldsymbol{B}$ is the magnetic field and $\frac{\delta M_s}{\delta t}$ is the change due to collisions.

Finally, the second moment yields the energy equation for species s which describes the change in energy,

$$\mathbb{EE}_s : \left[\frac{\partial}{\partial t} + \boldsymbol{u_s} \cdot \nabla\right]\left(\frac{3}{2} p_s\right) + \frac{3}{2} p_s(\nabla \cdot \boldsymbol{u}_s) + \nabla \cdot \boldsymbol{q}_s + P_s : \nabla \boldsymbol{u}_s = \frac{\delta E_s}{\delta t} \quad (2.10)$$

where p_s is the partial pressure, $\boldsymbol{q}_s$ is the heat flow vector, P_s is the pressure tensor and $\frac{\delta E_s}{\delta t}$ is the change in energy due to collisions.

2.1.3 The electron energy equation

Equation 2.10 can be rewritten as a partial differential equation (PDE) for the electron temperature, that is

$$\frac{3}{2} k_b n_e \left(\frac{\partial}{\partial t} T_e + \boldsymbol{u}_e \cdot \nabla T_e\right) + k_b n_e T_e \nabla \boldsymbol{u}_e = \nabla(\kappa_e \nabla T_e) + Q - L \quad (2.11)$$

where κ_e is the electron heat conductivity, Q is the local energy source and L is the local energy loss or cooling rate.

Further, the ionospheric electrons conduct heat mainly along the magnetic field lines [36]. This allows for further simplifications when performing electron heating experiments in polar regions, that is it is safe to assume that the heating beam, the radar beam, and the direction of the electron heat conductivity are parallel to the magnetic field and therefore also each other. Following [36] the electron energy equation reduces to a one-dimensional energy equation

$$\frac{3}{2} k_b n_e \left(\frac{\partial T_e}{\partial t} + v_e \frac{\partial T_e}{\partial z}\right) + k_b n_e T_e \frac{\partial}{\partial z} v_e = \frac{\partial}{\partial z}\left(\kappa_e \frac{\partial T_e}{\partial z}\right) + Q_{\mathrm{HF}} + Q_0 - L \quad (2.12)$$

where v_e is the electron drift velocity along the magnetic field, Q_{HF} and Q_0 is the HF heat source and the background heat source respectively, and L is the electron heat loss or cooling rate. Equation 2.12 can be simplified further under the assumption of negligible heat transfer due to convection [26]. This assumption is valid if the field aligned plasma drifts v_e are negligible.

$$\frac{3}{2}k_b n_e \frac{\partial T_e}{\partial t} = \frac{\partial}{\partial z}\left(\kappa_e \frac{\partial T_e}{\partial z}\right) + Q_{\mathrm{HF}} + Q_0 - L \tag{2.13}$$

This resulting, simplified electron energy equation is the equation we use for modeling electron temperatures and estimating heat sources in the analysis performed for this thesis.

2.1.4 Waves in plasma

Countless different waves can exist and propagate in a plasma. They can have oscillating electric fields and oscillating magnetic fields, they can have small and large amplitudes and propagate in different directions relative to an external magnetic field. In this section, brief descriptions of a few relevant plasma waves are presented, sorted from least complex to most complex in terms of their derivations and dispersion relations. The descriptions are based on [3, 9, 34].

Electron plasma waves and plasma oscillations

Fluctuations in the background electron density will give rise to electric fields that will counter these fluctuations by pulling the straying electrons back toward their equilibrium position. Because the electrons have inertias, they will overshoot their equilibrium positions which will give rise to new electric fields. These back-and-forth motions, or oscillations, move with the plasma frequency ω_p which is derived from $\mathbb{CE}_e$, $\mathbb{ME}_e$ and $\mathbb{PE}$. We assume that there is no magnetic field, no thermal motion and that the ions are fixed due to their larger inertias. This yields ω_p

$$\omega_p = \sqrt{\frac{n_0 e^2}{\epsilon_0 m}} \tag{2.14}$$

where m is the electron mass. The remaining variables are previously defined. The oscillations do not depend on wavenumber $\boldsymbol{k}$, i.e. the group velocity is zero and the oscillations do not propagate. These oscillations are called plasma oscillations.

Electron plasma waves, or *Langmuir waves*, are electrostatic waves that can propagate in any direction in unmagnetized plasmas, but that will propagate along an external magnetic field if one is present. These waves can be seen as

an extension of the plasma oscillations if thermal pressure is included in $\mathbb{ME}_e$. If there is a pressure gradient between two regions in a plasma with different temperatures, electrons from the hotter region will stream into the region with the lower temperature. The streaming electrons will oscillate as they stream into the other region. The dispersion relation for electron plasma waves is derived from the same set of equations and under the same assumptions as the plasma oscillations, except thermal motion is included. The resulting dispersion relation is

$$\omega^2 = \omega_p + \frac{3}{2} v_{\text{th}}^2 \boldsymbol{k}^2 \tag{2.15}$$

where $v_{\text{th}} = \sqrt{\frac{2k_b T_e}{m}}$ is the electron thermal velocity and $\boldsymbol{k}$ is the wave vector.

Electron plasma waves are important in relation to Langmuir turbulence which in turn is related to resonant electron heating which is discussed in section 2.3.2. In addition, they are important for the Incoherent Scatter Radar (ISR) technique which will be discussed in section 2.4.2.

Ion acoustic waves

Due to their larger mass, ions do not partake significantly in high frequency plasma oscillations and are not included in the derivation of the electron plasma waves. However, we can have ion acoustic waves that can be considered a lower frequency variant of the electron plasma waves. The derivation of the dispersion relation for the ion waves obviously includes ion motion. Contrary to the derivation of the electron plasma waves, we also need to include electron motion when considering the ion motion. This is due to the electrons' lower inertias that allow them to follow the ion motion.

The dispersion relation for ion acoustic waves is derived from $\mathbb{CE}_s$ and $\mathbb{ME}_s$ for both ion and electrons. The derivation also makes use of the *plasma approximation* which states that $n_i = n_e = n$ and that the gradient of the electric field is non-zero. Both of these assumptions are generally appropriate to make, as long as a low frequency wave with wavelength larger than λ_D is assumed. This means that we operate on timescales large enough for both ion motion and electron motion to be considered. Finally, the dispersion relation for ion acoustic waves is

$$\omega^2 = \boldsymbol{k}^2 C_s^2 \tag{2.16}$$

where

$$C_s = \sqrt{\frac{\gamma_i k_b T_i + \gamma_e k_b T_e}{m_i}} \tag{2.17}$$

is the ion acoustic speed. γ_i and γ_e are the adiabatic indices for ions and electrons, respectively and m_i is the ion mass. Usually, $\gamma_e = 1$ can be assumed as the electrons can be assumed to be isothermal due to their high velocity compared to the ion acoustic waves.

Ion acoustic waves are important for the ISR technique which will be discussed in section 2.4.2.

Upper hybrid waves and upper hybrid oscillations

Upper hybrid oscillations are high frequency oscillations across the magnetic field $\boldsymbol{B}$. The high frequency means that only electrons are considered, as with the plasma oscillations. The resulting dispersion relation will also only consider local oscillations because we no pressure gradient, and therefore no thermal motion, is included. Including thermal motion leads to upper hybrid waves. Contrary to the plasma oscillations, upper hybrid oscillations only exist in magnetized plasma and oscillate perpendicular to the magnetic field. The same goes for electron plasma waves and upper hybrid waves; upper hybrid waves only propagate across magnetic field $\boldsymbol{B}$.

The dispersion relation for the upper hybrid oscillations is derived from $\mathbb{ME}_e$, $\mathbb{CE}_e$ as well as $\mathbb{PE}$ under the assumptions that there is no thermal motion, that the oscillations are perpendicular to $\boldsymbol{B}$ and that the ions are at rest due to the high frequency of the oscillation. This yields

$$\omega^2 = \omega_{\mathrm{UH}}^2 = \omega_p^2 + \omega_c^2 \tag{2.18}$$

where ω_{UH} is the upper hybrid frequency and ω_c^2 is the electron cyclotron frequency.

Including thermal motion yields the dispersion relation for upper hybrid waves

that propagate *purely* $\perp \boldsymbol{B}$.

$$\omega^2 = \omega_{\mathrm{UH}}^2 + \frac{3}{2} v_{\mathrm{th}}^2 \boldsymbol{k}^2 \tag{2.19}$$

It is important to note that this is the simplest case of upper hybrid waves, where they propagate purely perpendicular to the magnetic field. However, upper hybrid waves can also propagate at angles oblique to the magnetic field. The dispersion relation for these waves is

$$\omega^2 = \omega_{\mathrm{UH}}^2 + \frac{3 v_e^2 \omega_p^2 k_x^2}{\omega_p^2 - 3\omega_e^2} - \frac{\omega_c^2 \omega_p^2}{\omega_{\mathrm{UH}}^2} \frac{k_z^2}{k_x^2} \tag{2.20}$$

where k_x is the wave number $\perp \boldsymbol{B}$ and k_z is the wave number $||\boldsymbol{B}$ [23].

Upper hybrid waves are important in relation to resonant electron heating which will be discussed in section 2.3.2.

Electron Bernstein waves

Electron Bernstein oscillations are a type of *electron cyclotron oscillation* that can arise from harmonics of the electron cyclotron frequency. These oscillations have frequencies that are multiples of the electron cyclotron frequency ω_c. The multiples of the electron cyclotron frequency, or harmonics, arise when particles' cyclotron orbits are disturbed due to the wave's electric and magnetic fields. Electron Bernstein waves are propagating electron Bernstein oscillations that arise from included thermal motion.

The derivation of the dispersion relation of electron Bernstein waves is lengthy and complicated and will not be discussed here. It can be found in [9]. The dispersion relation is

$$\frac{k_\perp^2}{k_D^2} = 2\omega_c^2 \sum_{n=1}^{\infty} \frac{e^{-b} I_n(b)}{\omega^2 - n^2 \omega_c^2} n^2 \equiv \alpha(\omega, b) \tag{2.21}$$

where $k_\perp$ is the wave number perpendicular to $\boldsymbol{B}$, k_D is defined as $k_D = 2\omega_p^2 / v_{\mathrm{th}}^2$, b is defined as $b = k_x^2 v_{th}^2 / 2\omega_c^2$ where k_x is the wave number in the plane perpendicular to $\boldsymbol{B}$, $I_n(b)$ is n-th order Bessel function of imaginary argument and n is the harmonic number.

The function $\alpha(\omega, b)$ is plotted for $b = 1$ for the first few harmonics n in Figure 2.2. The shaded area shows where $\alpha(\omega, b) = k_\perp^2/k_D^2 > 0$ which gives the allowed frequencies ω for the EB wave. Allowed regions start barely above each harmonic frequency and stop below the next harmonic. This means that there are *forbidden* regions below each harmonic in which the wave cannot propagate. Note the that the gaps below each harmonic decreases in width for increasing harmonic number n. It is important to note that this is only true for all harmonic numbers $n > 2$, that is there are no forbidden gaps for $n \leq 2$. This is not shown in Figure 2.2. It is visible in the full dispersion relations (2.21) for different relationships ω_p^2/ω_c^2.

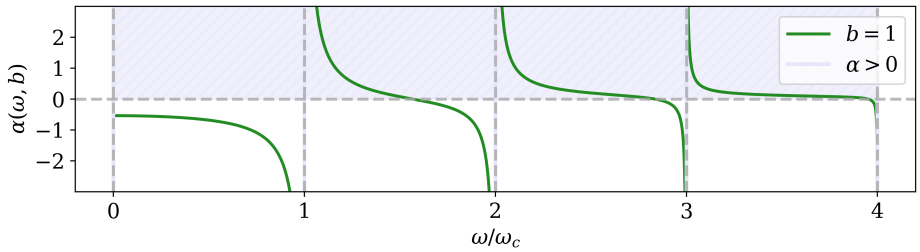

Figure 2.2: Function $\alpha(\omega, b)$ (in equation 2.21) for $b = 1$. After [9].

Like UH waves, EB waves are important in relation to resonant heating which will be discussed in section 2.3.2. Interestingly, the fluid limit of equation 2.21 is the upper hybrid oscillation and show that they are strongly related.

2.1.5 Instabilities in plasma

Numerous instabilities can arise in a plasma. For this thesis, brief descriptions of two of these instabilities are necessary. These are the Oscillating Two Stream Instability (OTSI) and the Parametric Decay Instability (PDI).

A streaming instability, like the OTSI, can arise when different species in the plasma have drifts relative to each other [9]. This can occur when energetic particles stream through a plasma, or when there is a current in the plasma. In a streaming instability, waves can be excited. These waves are excited by the drift energy, which is dependent on the relative drift velocity between the two streams. In the PDI an incident wave decays into another, or several other, wave modes.

2.2 The ionosphere

This section gives an overview over the structure of the ionosphere and how radio waves propagate in the ionosphere. The descriptions are based on [5, 34].

2.2.1 Structure

The ionosphere is partly ionized. The dominant ionization process is photoionization from solar radiation, in the form of extreme Ultraviolet (UV) photons. This means that the degree of ionization, and therefore also the ionospheric electron density, is highly variable with time of day, season, and solar cycle. At polar latitudes, the ionosphere is also ionized in collisions with high-energy particles precipitating into the ionosphere during auroral events.

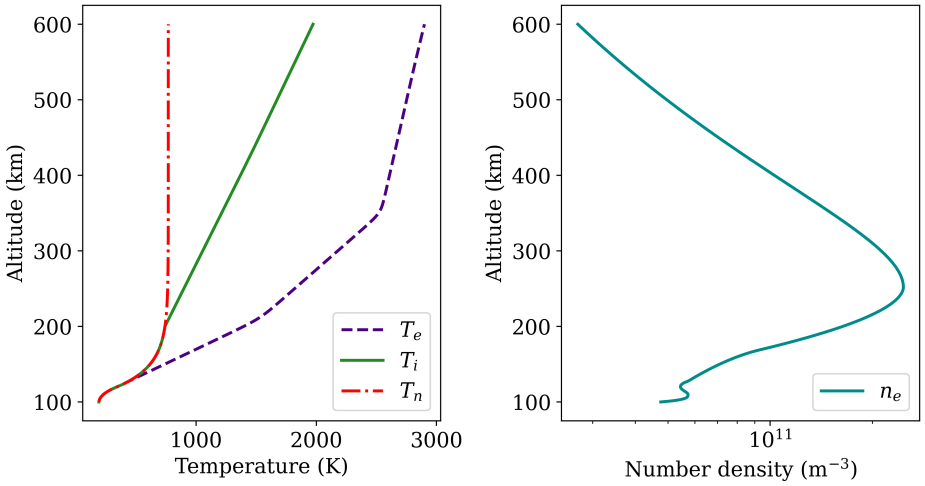

Figure 2.3: IRI model ionospheric parameters from the 8th of October 2020 at 11:00:00 UT.

An ionospheric electron density profile is shown in the right panel in Figure 2.3. The electron density is retrieved from the International Reference Ionosphere (IRI) model [11] for the 8th of October 2020. The density has a clear peak at about 250 km. Due to the high variability of atmospheric convection and thermospheric conditions which cause ionization at different altitudes, this peak can shift to both higher and lower altitudes. The electron density also has a smaller local peak slightly above 100 km. These local peaks are also highly variable and can be the results of auroral events which cause ionization at these lower altitudes. The electron density as a function of altitude is to the first order

the balance between ionization and recombination at that altitude.

Ionospheric electron, ion and neutral temperature profiles are shown in the left panel in Figure 2.3, also retrieved from the IRI model for the 8th of October 2020. The high electron temperatures are a result of the absorption of UV radiation and production of super-thermal photoelectrons which heat the bulk of the ionospheric electrons. Because of their low mass and high mobility, electrons are not as effectively cooled by neutrals as the ions. Therefore, the electron temperatures are higher. When neutral particles are ionized by UV radiation, the resulting ion and electron can carry some left-over energy. The resulting ions similar masses to the neutrals and will therefor transfer their energy to the neutrals more efficiently in collisions. This leads to the ion temperature being higher than the neutral temperature. Just as the ionospheric electron density, the ionospheric temperatures are also highly variable with time of day, season, and solar cycle.

The ionosphere can be separated into three distinct regions: The D-region, the E-region, and the F-region. The regions differ in their compositions, ionization rates and recombination rates and the boundaries between the regions are not strictly defined. Brief descriptions based on [5, 34] are presented in the three following sections.

F-region

The F-region is the top region of the ionosphere and spans upwards from approximately 150 km. The F-region typically have the highest electron density of the three regions and remains during night-time. The recombination processes in the F-region are simple. Due to the low F-region ion densities, only recombination with O^+ ions needs to be considered. This recombination happens in two different two-stage process. In the first process an O^+ ion participates in a charge exchange with molecular oxygen, creating an O_2^+ ion and atomic oxygen before the O_2^+ ion recombines with an electron to form two oxygen atoms.

$$\begin{aligned} &\text{(a)} \qquad O^+ + O_2 \rightarrow O_2^+ + O \\ &\text{(b)} \qquad O_2^+ + e^- \rightarrow 2O \end{aligned} \tag{2.22}$$

In the second process an oxygen ion reacts with molecular nitrogen, creating a NO^+ ion and atomic nitrogen. Next, the NO^+ ion recombines with an electron, creating a nitrogen atom and an oxygen atom.

$$\begin{aligned} &\text{(a)} \quad O^+ + N_2 \rightarrow NO^+ + N \\ &\text{(b)} \quad NO^+ + e^- \rightarrow N + O \end{aligned} \tag{2.23}$$

The F-region is the region of interest in this thesis.

E-region

The E-region is the middle region of the three ionospheric regions and spans from approximately 80 km to about 150 km. The E-region differs from the F-region in that only some ionization remains during night-time. The E-region was the first layer of the ionosphere that was discovered [34] because it can reflect electromagnetic radio waves, hence the name the *E-region*. The recombination processes in the E-region include a higher number of processes than in the F-region. The dominant recombination processes are direct dissociative recombination with NO^+ and O_2^+ ions which dominate the E-region. The two recombination processes are shown in the second steps in equations 2.22 and 2.23.

D-region

The D-region is the lowest of the three ionospheric regions and is typically said to span from about 60 km to about 80 km in altitude. What characterizes the D-region is that it has the highest pressure of the three regions and that it is dominated by collisions. This yields the highest recombination rates among the three regions and therefore a lower electron density. The recombination processes are many, and in general the chemistry in the D-region is incredibly complicated and involve electrons, positive ions, negative ions, and cluster ions.

The D-region is important because the high collision frequencies means that radio waves in both the Medium Frequency (MF) and High Frequency (HF) ranges can be absorbed. In experiments where it is of interest to investigate the F-region it is therefore important to have a lower D-region density. For night-time experiments this is of no concern. The high recombination rates make the D-region disappear in the absence of photoionization during the night. For day-time conditions, however, the D-region remains and can influence experiments by absorbing HF radio waves.

2.2.2 Propagation of radio waves in the ionosphere

How a radio wave propagates in the ionosphere depends on the wave mode [9, 29]. The two wave modes most commonly used in ionospheric modification experiments are the Ordinary Wave (O-mode) and the Extraordinary Wave (X-mode). Both O-mode and X-mode waves are electromagnetic waves with wave vector $\boldsymbol{k}$ perpendicular to magnetic field $\boldsymbol{B}_0$, that is $\boldsymbol{k} \perp \boldsymbol{B}_0$ [9]. However, they differ in the way that O-mode waves are linearly polarized, that is $\boldsymbol{E} \parallel \boldsymbol{B}_0$, while X-mode waves are partly transverse and partly longitudinal, that is $\boldsymbol{E} \perp \boldsymbol{B}_0$. The dispersion relations for O-mode and X-mode waves are presented in equation 2.24 [9].

$$\begin{aligned} &\text{O-mode:} && \omega^2 = \omega_p^2 + c^2\boldsymbol{k}^2 \\ &\text{X-mode:} && \frac{c^2\boldsymbol{k}^2}{\omega^2} = 1 - \frac{\omega_p^2}{\omega^2}\frac{\omega^2 - \omega_p^2}{\omega^2 - \omega_{\mathrm{UH}}^2} \end{aligned} \tag{2.24}$$

It is important to note that these descriptions and dispersion relations are only valid under the constraint that $\boldsymbol{k} \perp \boldsymbol{B}_0$ and are therefore a simplification. However, if all propagation angles between perpendicular and parallel to $\boldsymbol{B}_0$ are considered, the two waves will both be elliptically polarized and the dispersion relations becomes dispersion *surfaces*, well visualized by Rexer in 2021 (see Figures 4.1 and 4.2 in [29]).

The different dispersion relations give rise to different propagations in the ionosphere and yields two different cutoff frequencies. The cutoff frequencies are found when $\boldsymbol{k} \to 0$, that is when the wave stops propagating, it is *cut off*. For the O-mode wave and X-mode wave these frequencies, denoted ω_O and ω_X respectively, are

$$\begin{aligned} &\text{O-mode:} && \omega_O = \omega_p \\ &\text{X-mode:} && \omega_X = \frac{1}{2}\left[\omega_c + \left(\omega_c^2 + 4\omega_p^2\right)^{1/2}\right] \end{aligned} \tag{2.25}$$

The cutoff frequencies are plotted as a function of altitude in Figure 2.4. The altitude dependence comes from the fact that $\omega_p \propto \sqrt{n_e}$ (from equation 2.14) where n_e varies with altitude (shown in Figure 2.3). This leads to different cutoff altitudes for the two modes, dependent on the plasma frequency for both, and dependent also on the electron cyclotron frequency ω_c for the X-mode wave. In Figure 2.4 it is clear that an X-mode wave with some frequency ω will be reflected at a lower altitude than an O-mode wave with the same frequency ω.

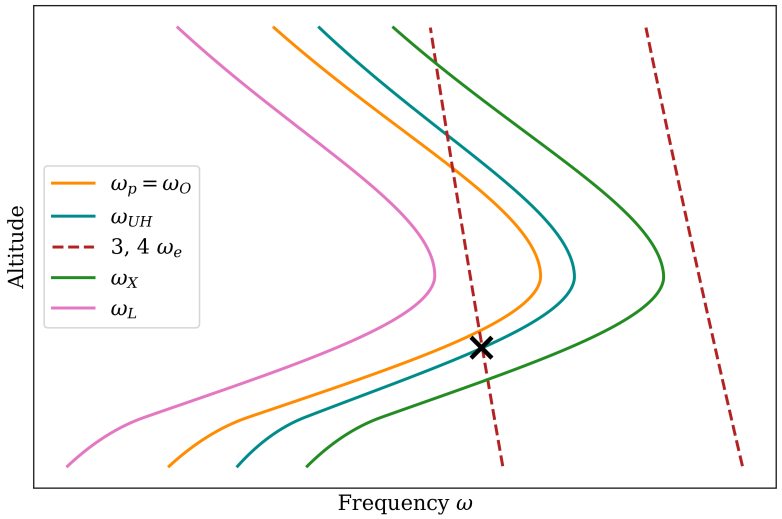

Figure 2.4: Ionospheric frequencies as a function of altitude, plasma frequency and O-mode cutoff (orange), upper hybrid frequency (blue), 3rd and 4th electron gyroharmonic frequency (dashed dark red), X-mode cutoff (green) and L-mode cutoff (pink). The black cross mark the third double resonance. The magnitudes on both axes are omitted due to this figure being of purely illustrative purposes.

Though O-mode and X-mode waves are used in ionospheric modification experiments, another wave mode is also important. This mode is the L-mode. As an O-mode wave transmitted into the ionosphere approaches its reflection altitude, it is continuously refracted up to its reflection altitude where $\omega_O = \omega_p$. Through refraction the wave will at some point be oriented with $\boldsymbol{E} \parallel \boldsymbol{B}_0$. From this point the propagation of the wave will follow one of two possible propagations. First, if the decomposition of $\boldsymbol{k}$ onto $\boldsymbol{B}_0$, $\boldsymbol{k}_\perp$, is nonzero, and the wave is propagating at an angle oblique to or perpendicular to $\boldsymbol{B}_0$, the wave is reflected. However, if $\boldsymbol{k}_\perp$ is zero, the dispersion surfaces of the O-mode wave and the L-mode wave meet [29]. This means that the O-mode wave can *switch surfaces* and continue propagation in the L-mode. This means that the wave is not reflected. This possible loophole is important for research on the top side of the ionosphere and is called the *radio window* [29]. The two-dimensional dispersion relation and the cutoff frequency of the L-mode is presented in equation 2.26 and is plotted in Figure 2.4 [9].

$$\text{L-mode:} \qquad \begin{aligned} \frac{c^2\boldsymbol{k}^2}{\omega^2} &= 1 - \frac{\omega_p^2}{\omega^2}\frac{1}{1+\frac{\omega_c}{\omega}} \\ \omega_L &= \frac{1}{2}\left[-\omega_c + \left(\omega_c^2 + 4\omega_p^2\right)^{1/2} \right] \end{aligned} \tag{2.26}$$

From Figure 2.4 it is clear that an L-mode wave will be reflected at a higher altitude than both the O-mode wave and the X-mode wave, unless it does not meed ω_L and is not reflected at all.

2.3 Electron heating

Electrons can be heated artificially in ionospheric modification experiments when a high frequency radio wave is transmitted into the ionosphere. Electron heating can be split into two types: nonresonant heating and resonant heating. These two types will be discussed in sections 2.3.1 and 2.3.2, respectively. The heating depends strongly on the pump wave frequency, propagation angle relative angle to the Earth's magnetic field and the pump wave power. These dependencies will be discussed briefly.

2.3.1 Nonresonant heating

Nonresonant heating, sometimes also called underdense heating, is the only heating effect resulting from a pump wave with frequency above the upper hybrid frequency at all altitudes z, that is

$$f_{\text{pump}} > f_{\text{UH, peak}} = \sqrt{f_{p,\text{ peak}}^2 + f_e^2} \tag{2.27}$$

where f_{pump} is the pump wave frequency, $f_{\text{UH, peak}}$ is the peak upper hybrid frequency, $f_{p,\text{ peak}}$ is the peak plasma frequency and f_e is the electron cyclotron frequency. Pump waves with these frequencies are not reflected in the ionosphere and propagates through the ionosphere. Then there will not be any resonant interactions between the pump wave and the ionospheric plasma. Even though there are no resonant interactions between the pump wave and the ionospheric plasma, the pump wave will still heat the electrons through ohmic heating [17].

Because it is ionized, a current will be induced when the pump wave passes through the ionosphere. A sketch of this process is shown in Figure 2.5. The energy deposition from the wave into the plasma is given as a time averaged Poynting flux, that is

$$\langle Q \rangle = \langle \boldsymbol{E} \cdot \boldsymbol{J} \rangle \tag{2.28}$$

where $\boldsymbol{Q}$ is the deposited energy, $\boldsymbol{E}$ is the electric field and $\boldsymbol{J}$ is the current [9].

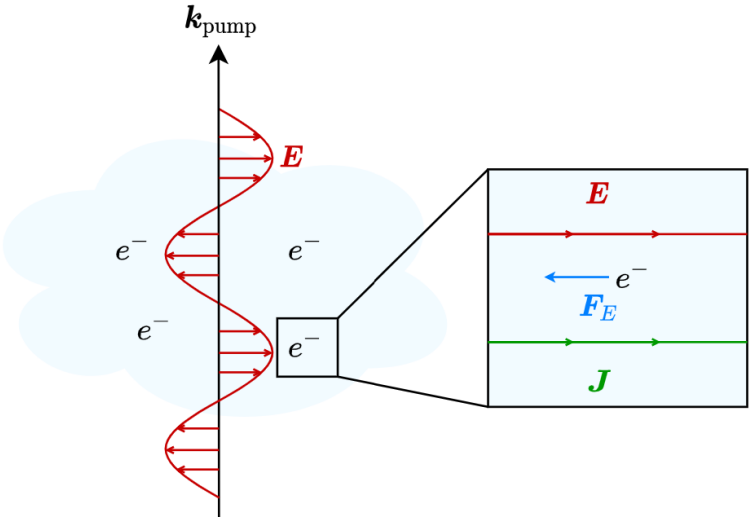

Figure 2.5: Sketch of a pump wave with frequency $f_{\text{pump}} > f_{\text{UH, peak}}$, wavenumber $\boldsymbol{k}$, and electric field $\boldsymbol{E}$ propagating through the ionosphere. The blue cloud shows the ionospheric plasma, and the blue box show how the ionospheric electrons are accelerated (or deaccelerated) by the pump wave electric field and the resulting induced current $\boldsymbol{J}$ (green).

The induced current will oscillate with the same frequency as the pump wave frequency. In a collisionless plasma the current $\boldsymbol{J}$ will be in anti-phase with the electric field, that is their phases will be separated by 90^o. This mean that the energy deposition into the plasma, given in equation 2.28, is zero. However, the ionosphere is not collisionless. Because the electrons participate in collisions their motion is randomized, and the induced current is phase shifted. This yields a non-zero energy deposition into the plasma which heats the electrons. Figure 2.6 shows an electric field $\boldsymbol{E}$, collisionless current $\boldsymbol{J}$ and a collisional current $\boldsymbol{J}_{\text{coll}}$. $\Delta\phi$ is the phase shift between the collisional current and the noncollisional current.

The nonresonant heating can also be expressed as

$$Q_\Omega = \frac{1}{2} \text{Re} \left[\boldsymbol{E}^* \cdot \bar{\sigma} \cdot \boldsymbol{E} \right] \tag{2.29}$$

where Q_Ω is the ohmic heating rate, $\boldsymbol{E}$ is the electric field and $\bar{\sigma}$ is the conductivity tensor [17]. Note that both the pump wave electric field and the conductivity tensor depend on the pump wave polarization. The electric field is dependent on the refractive index ϵ, altitude z, pump wave number k_0 and the ionosphere refractive index $\mathcal{N}$.

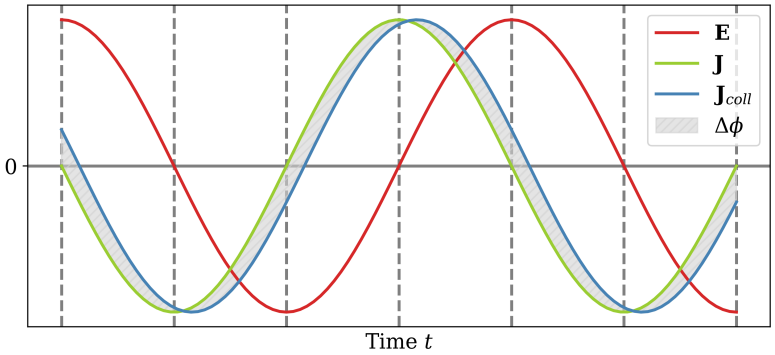

Figure 2.6: Illustration of electric field $\boldsymbol{E}$, noncollisional current J, collisional current $\boldsymbol{J}_{\text{coll}}$ and phase shift $\Delta\phi$.

Nonresonant heating has been investigated on several occasions. It was modeled by Gustavsson et al. in 2010 [17]. They found that ohmic heating can be accurately modeled from the convectionless and one-dimensional electron energy equation (equation 2.13) and equation 2.29. They observed temperature enhancements up to 800 K. Enhancements in the range 300 K - 400 K were observed by Löfås et al. in 2008. [26].

2.3.2 Resonant heating

Resonant heating, sometimes also called overdense heating, involves several complicated non-linear processes [23, 31]. This section provides an overview of the involved processes. An illustration of the involved processes is shown in Figure 2.7. Resonant heating occurs when the frequency of the pump wave is smaller than the peak upper hybrid frequency, that is

$$f_{\text{pump}} < f_{\text{UH, peak}} \tag{2.30}$$

Because the cutoff altitude of an X-mode wave always is lower than the upper hybrid resonance height (shown in Figure 2.4 as ω_{UH}), O-mode waves, and

not X-mode waves, are used in experiments when it is desired to investigate resonant heating. When the O-mode pump wave approaches its reflection altitude at the plasma frequency, the phase velocity decreases towards zero, that is $v_\phi \to 0$. This results in a larger electric field amplitude, simply due to energy conservation [23]. This process is called *swelling*.

Slightly below the reflection altitude, the pump wave frequency passes the upper hybrid frequency, that is $f_{\text{pump}} = f_{UH}$. Around this altitude, called the UHR altitude, UH waves are excited from frequency matching with the pump wave frequency. This process is called Upper Hybrid Resonance. UH waves are continuously excited by the pump wave as long as the pump wave is transmitted. Because they propagate across the magnetic field, the excited UH waves can get trapped in natural striations in the electron density [31]. This continuous excitation leads to a also continuously increasing UH wave amplitude of the trapped wave. The energy dissipation of the trapped UH wave into the plasma heats the electrons. The increase in the electron temperature within the striation leads to a pressure gradient that pushes plasma out of the striation. This results in a larger depletion in the electron density and the depth of the striation increases. This leads to a more effective trapping of the UH wave which further increase the wave amplitude and energy dissipation into the plasma. Clearly, this process is a positive feedback loop that will continue until the pump wave is no longer transmitted and UH waves are no longer excited. The continuously increasing UH wave amplitude can result in Upper Hybrid Turbulence (UHT) which result in an *explosion* of non-linear processes that are outside the scope of this thesis. However, it is important to note that UHT also lead to electron heating.

The induced striations in the electron density also lead to focusing of the pump wave due to refraction on the striations [31]. The refraction focus the pump wave and therefore UH wave excitation into smaller regions. This focusing increases the energy deposition into these smaller regions. It is also worth noting that the electrons are heated by EB waves which arise when the pump frequency approaches harmonics of the electron cyclotron frequency. However, these waves propagate along the magnetic field and are not trapped in the electron density striations as the striations are field-aligned.

Right below the reflection altitude, where $f_{\text{pump}} = f_{\text{O}} = f_p$, electron plasma waves which have frequency f_p can be excited. This can result in Langmuir Turbulence (LT). LT can arise from striations in the electron density of a plasma [1]. A decrease in density in some region in the plasma will lead to a higher refractive index in the same region, which can lead to a concentration of wave energy inside the region. This can again decrease the density as plasma is pushed out of the region, which again increase the refractive index. Electron plasma waves trapped in the density striations accelerate electrons. However,

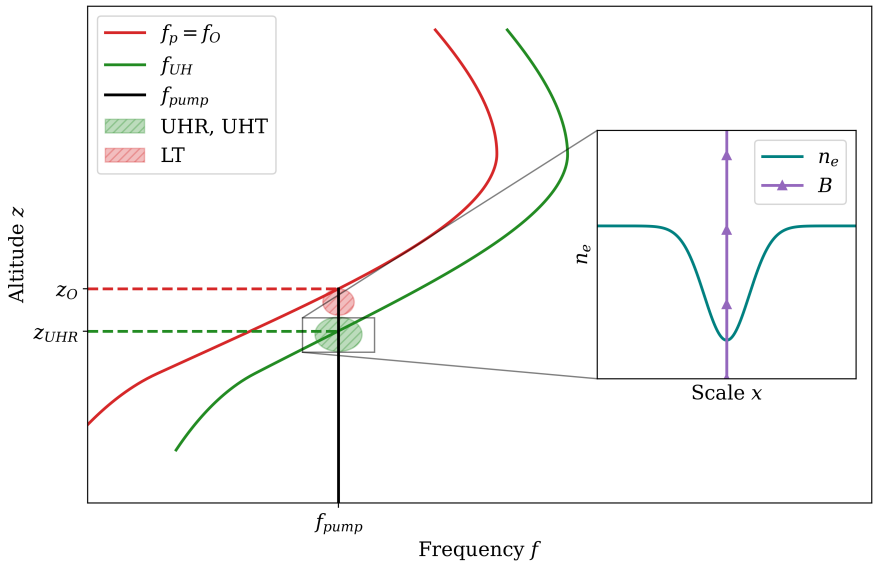

Figure 2.7: Overview of the processes and phenomena involved in resonant heating. The shaded areas show where UHR, UHT and LT occur. The inserted axis shows a sample field aligned electron density striation. Note that this figure is only for illustrative purposes and is not to scale.

LT is not as sensitive to density striations as UHT and grows faster than UHT. Also, LT can induce the PDI. A large amplitude electron plasma wave can decay into a smaller amplitude electron plasma wave with opposite wave number and an ion acoustic wave [9].

As mentioned previously, the resonant electron heating has strong dependencies. First, the efficiency, η, depends on the power of the transmitted pump wave. This was found by both Bryers et al. in 2012 [7] and Senior et al. [35] in 2013. By estimating the heater flux at the UHR altitude and comparing this to the modeled column integrated heating rate, they estimated the power variation of η. The increase in efficiency for the nonresonant heating is explained by an increase in striations in the electron density. The increased striations are a result of the higher power which yields a larger electric field amplitude. The increased striations trap UH waves more effectively. This leads to a higher rate of energy dissipation into the ionospheric plasma which heats the electrons. The efficiency increases non-linearly with increased power, which is different from the non-resonant heating, where the efficiency increases linearly. Also, hysteresis effects in anomalous absorption when sweeping the pump power up and down have been observed [19, 32, 39].

Further, the nonresonant heating depend on the angle to the magnetic field.

Enhancements in electron temperature are largest when the pump beam is pointed towards magnetic zenith [31]. The temperature enhancements are also largest around magnetic zenith, regardless of whether the heater beam is pointed toward magnetic zenith or not [22, 31]. This was also found to be true for the column integrated heating rate [22]. This can be explained by mode conversions in density ducts in the electron density close to magnetic zenith. In these ducts an O-mode wave can be transformed to an L-mode wave which is able to propagate to higher altitudes before reaching its cutoff frequency. This yields to heating at higher altitudes and therefore an increased column integrated heating rate.

Finally, the difference between nonresonant and resonant heating was modeled by Bryers et al. in 2013 [6]. In their experiment they heated the ionosphere with O-mode pump waves as well as X-mode pump waves. Because the reflection height of an X-mode wave is below the UHR height, ohmic heating is the only heating effect. By comparing the total heating in X-mode periods and O-mode periods, they found that the nonresonant heating is smaller than the resonant heating by a factor between 2 and 5.

2.3.3 Electron cooling

Ionospheric electrons loose energy to neutrals in the background atmosphere and to ions. Dominant cooling rates for the ionosphere are shown in Figure 2.8. The dominant cooling rates in the ionosphere, from [17], are energy loss in elastic collisions with ions (L(e-ion)), energy loss in elastic collisions with neutrals ($L(O_2$, el), $L(N_2$, el) and L(O, el)), excitation of rotational states in nitrogen and oxygen molecules ($L(N_2$, rot) and $L(O_2$, rot)), excitation of vibrational states in nitrogen and oxygen molecules ($L(N_2$, vib) and $L(O_2$, vib)), excitation of fine structure levels in atomic oxygen (L(O, fs)) and finally excitation of oxygen to its lowest electronic state ($L(O(^1\,D))$). The importance of each of the cooling rates vary [34] with the ionospheric conditions like altitude, season, time of day, solar activity and geomagnetic activity, but depend mostly on T_e, T_i, T_n and the neutral densities.

The cooling rates in Figure 2.8 are calculated based on electron temperatures, ion temperatures and electron densities during HF ON and HF OFF periods during the experiment done on the 8^{th} of October 2021. It is clear that the cooling rates are highly variable with both altitude and electron temperature. At high altitudes, the dominant cooling process is energy loss in elastic collisions with ions. At lower altitudes, the dominant cooling processes are (1) excitation of vibrational states in molecular oxygen and molecular nitrogen, as well as (2) excitation of fine structure levels in atomic oxygen and (3) excitation of rotational states in molecular nitrogen. It is also important to note that the

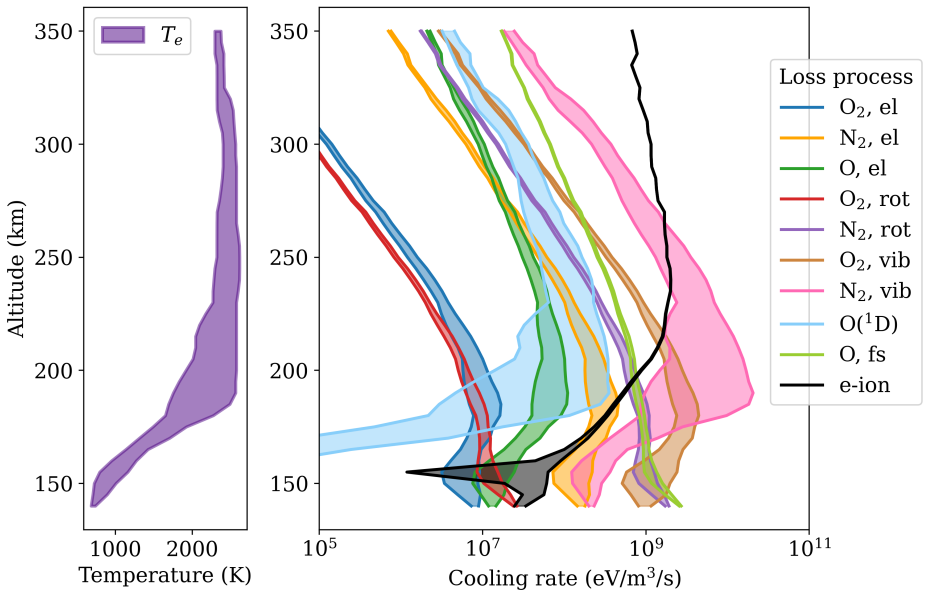

Figure 2.8: Electron cooling rates as a function of altitude z for both ambient electron temperatures and HF heated electron temperatures. The left panel shows electron temperatures from the experiment on the 8$^{\text{th}}$ of October 2021 (used for illustrative purposes), from ambient (minimum) temperatures to HF heated (maximum) temperatures. The left panel shows cooling rates calculated from n_e, T_e and T_i from the experiment on the 8$^{\text{th}}$ of October 2021. The outlines correspond to minimum electron temperatures (left outline) and maximum electron temperatures (right outline). The colored area shows cooling rates for temperatures between the minimum and maximum temperatures.

dominant process depends on the electron temperature. It is clear in Figure 2.8 that the dominant process for the hottest electrons is $L(\mathrm{N_2}, \mathrm{vib})$ at lower altitudes while the dominant process for the coolest electrons at the same altitudes is $L(\mathrm{O_2}, \mathrm{vib})$. This means that the dominant cooling rates are different during HF ON and HF OFF periods during a heating experiment.

2.3.4 Stimulated Electromagnetic Emissions (SEE)

Stimulated Electromagnetic Emissions (SEE) are high frequency secondary radiation that can be stimulated by high frequency radio waves propagating into the ionosphere and are the result of numerous wave interactions in the ionospheric plasma [8]. The frequencies of the SEE are close to the frequency of the HF radio wave, usually within 100 kHz below and above the pump frequency. In addition, SEE signatures typically appear at specific frequency

shifts from the pump frequency. To illustrate the evolution of SEE signatures, a time-frequency spectrogram can be produced from received SEE. These spectrograms can include a myriad of different *SEE signatures*. The possible signatures have been reviewed in great detail by Leyser in 2001 [22]. The most important signatures for the experiments detailed in this thesis are the Downshifted Maxima (DM) and the Broad Upshifted Maxima (BUM). Their descriptions follow the descriptions given by Leyser [21] and Carozzi et al. [8], and are presented below.

DM are maxima that are shifted *down* in frequency from the HF pump frequency f_0 with frequencies $\Delta f_{\mathrm{DM}} = 2 \times 10^{-3} f_0$. DM are suppressed when f_0 is close to, or at, a gyro harmonic frequency. BUM differ from DM in that they span a broad range of frequencies, *upshifted* from HF frequency f_0. They are only found in narrow intervals above gyro harmonic frequencies. Both DM and BUM are useful and can be used to identify gyro resonance frequencies from a SEE spectrogram. Spectrograms from the experiments detailed in this thesis will be presented in chapter 4. As well as their heavy frequency dependence, SEE signatures also vary with the HF radio wave power and ionospheric conditions.

2.3.5 Electron heating around the double resonances

As previously mentioned, electron heating depends strongly on the HF pump frequency, primarily on how close the pump frequency is to a *double resonance* frequency. This is the focus of this thesis. Where the upper hybrid frequency ω_{UH} match harmonics of the electron cyclotron frequency $n\omega_c$, that is

$$\omega = \omega_{\mathrm{UH}} = n\omega_c \tag{2.31}$$

we have *double resonances*. The third double resonance, where $\omega = \omega_{\mathrm{UH}} = 3\omega_c$, is marked with a black cross in Figure 2.4.

Enhancements in electron temperature maximize around the second double resonance [20] and minimize around the third and fourth double resonance [16, 18, 33]. The minima around the third and fourth double resonances can be explained by the suppression of UH and EB excitation. The physical processes behind the suppression is explained in great detail by Grach et al. in 1994 [14]. They conclude that possible solutions to dispersion relations for both UH waves and EB waves decrease when the frequency approach double resonances $n > 2$. A decrease in possible solutions to the dispersion relations means that the possible existences of the two waves also decrease. When UH waves cannot

exist, density striations in the electron density are not excited.

The size of the regions in which the waves can not exist decrease with harmonic number. This means that the forbidden frequency gaps when varying the pump frequency narrow with increasing harmonic number $n > 2$. This also means that expected gaps in enhanced electron temperature enhancements narrow with increasing $n > 2$ [14]. This was observed experimentally by Robinson et al. in 1996 [33].

Finally, it is worth noting that there are indications of asymmetry around these double resonances [8, 14, 27]. Different wave modes, primarily upper hybrid and Bernstein electron waves, which are the main contributors to resonant electron heating, are dominant above and below the fourth double resonance, respectively [27]. Asymmetry and hysteresis in SEE signatures during frequency sweeping through the fourth double resonance has also been observed [8, 28]. The strength BUM were observed to be stronger when sweeping the frequency upwards than the strengths when sweeping the pump frequency downwards. Finally, Honary et al. [18] observed asymmetry in anomalous absorption, which is linked to resonant heating, when sweeping the frequency up and down through the third double resonance frequency.

2.4 Incoherent scatter radar

Incoherent Scatter Radar (ISR) is a powerful diagnostic tool used for investigating the ionosphere. This section gives a brief overview of the mechanisms behind ISR and the ISR spectrum. The descriptions follow [4, 13].

2.4.1 Incoherent scatter

When waves with wavenumber $\boldsymbol{k}^2 >> 1/\lambda_D^2$ and frequency $f >> f_p$ are transmitted into the ionospheric plasma, we do not get a response like the heating effects detailed in section 2.3. However, due to electrons being charged particles, ionospheric electrons will be slightly accelerated by the incident wave. The accelerating electron will radiate an electric field, or a *scattered* field. The combined scattered field from electrons within a *scattering volume* depend on density fluctuations $\mathcal{N}(\boldsymbol{k})$ within the scattering volume. It is important to note that even though the electrons, and not the ions, scatter the incident wave, the scattered field contains information about the ion motion. This is because the electrons follow the ion motion in shielding clouds, or Debye spheres, around the ions.

When ISR is used as a diagnostic tool, Ultra High Frequency (UHF) or Very High Frequency (VHF) waves are transmitted into the ionosphere, and a scattered field is received. For a monostatic radar, the relation between the transmitted signal and the received signal is given by the *radar equation* including backscatter gain, which is

$$P_r = P_t \frac{A_{\text{bs}}}{8\pi R^2} c T_p \sigma_{\text{radar}} \tag{2.32}$$

Where P_r is the received power, P_t is the transmitted power, A_{bs} is the effective antenna area which is related to the antenna beam pattern dependent backscatter gain, R is the range, c is the speed of light, T_p is the pulse period and σ_{radar} is the radar cross section.

The radar cross section is dependent on the ionospheric parameters and can be expressed as

$$\sigma_{\text{radar}} = 4\pi r_e^2 \sin^2 \chi N(\boldsymbol{k}) \tag{2.33}$$

where r_e is the electron radius, $\sin^2 \chi$ is the polarization factor and $N(\boldsymbol{k})$ is the ionospheric density fluctuations that include fluctuations in both the ion and electron densities.

The received signal is processed at reception to remove the radar frequency from the received signal. Finally, one can produce a power density spectrum (PDS) or an autocorrelation function (ACF) from which information about ionospheric parameters can be extracted.

2.4.2 The incoherent scatter spectrum

The incoherent scatter spectrum, or PDS, is the Fourier transform of the ACF. A sample F-region PDS is shown in Figure 2.9. The outer panels show the *plasma lines* while the middle panel shows the *ion line*. Note the different frequencies at which we find the ion line and the plasma lines. The description of the PDS given here follow [4].

The PDS shows how the total energy scattered from the scattering volume is distributed in frequency. The shape and size of the PDS depend on the presence of ionospheric waves in the scattering volume. These waves, usually ion acoustic waves and Langmuir waves, lead to an ordered motion of the ions

and electrons. This ordered motion results in enhanced scattering at the wave frequencies [4].

The plasma lines are the signatures of Langmuir waves. The upshifted plasma line is found at $f = f_p$ and corresponds to waves propagating toward the radar. The downshifted plasma line is found at $f = -f_p$ and is the result of waves propagating away from the radar. As the plasma lines are found at the plasma frequency, a reliable estimate of the electron density can be found from the plasma lines. However, the echo power of the plasma lines is usually weak and therefore they can be difficult to measure.

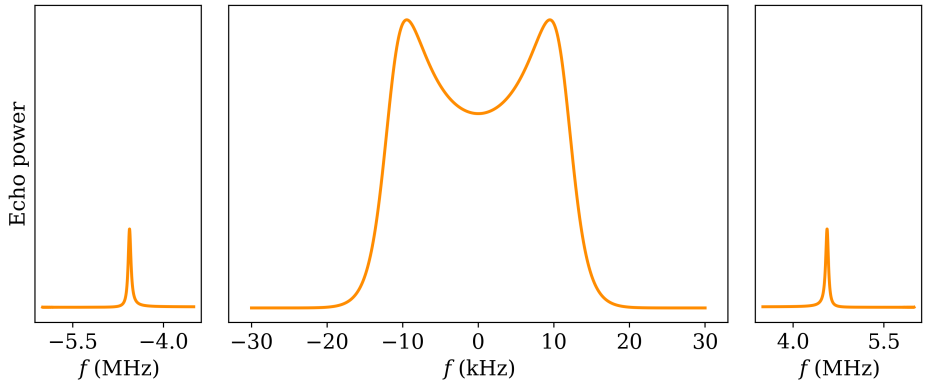

Figure 2.9: Sample F-region downshifted plasma line (left panel), ion line (middle panel), and upshifted plasma line (right panel) for $n_e = 2{\times}10^{11}$ m^{-3}, $T_e = 2000$ K, $T_i = 1200$ K, and radar frequency $f_R = 966$ MHz. Note the different units on the frequency axes and that the echo powers of the plasma lines and the ion line are not to scale.

The ion line is the signature of damped ion acoustic waves. The peaks of the ion line occur at approximately $f = \pm kC_s$. The height of the peaks above the middle of the spectrum gives information on the degree of damping and therefore information on the ratio between the electron temperature and the ion temperature. This is because the ions and electrons interact more if their temperatures are closer. The ion drift velocity, v_i, is found from the frequency shift away from 0 if the ion line is not symmetric around 0. The electron density n_e is proportional to the total scattered energy, that is the integral of the entire PDS. Altitude profiles for the different ionospheric parameters are constructed through pulse coding of the radar pulse, which makes it possible to distinguish between received signals from different altitudes [13].

HF enhanced ion lines

When conduction heating experiments, one can excite HF Enhanced Ion Lines (HFIL). This excitation happens slightly below the reflection altitude [31], and usually in the beginning of a HF pulse transmission. The excitation is a result of the PDI which results in both ion acoustic waves and Langmuir waves. The PDI arises from Langmuir turbulence as explained in section 2.3.2.

As explained previously, the ion line in the PDS is a measure of ion acoustic waves. Therefore, excitation of ion acoustic waves from the PDI result in an enhanced ion line. This yields falsely large estimates for the ionospheric parameters. Figure 2.10 shows two PDS as a function of altitude. The top panels show a typical ion spectrum, while the bottom panels clearly show an HFIL at approximately 200 km. HF Enhanced Plasma Lines (HFPL) can also be excited, due to electron plasma waves resulting from the PDI.

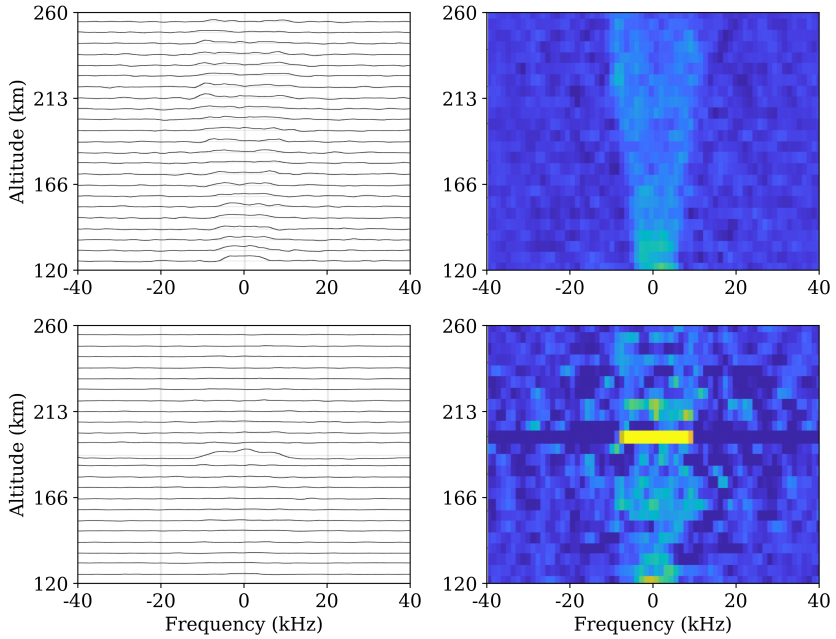

Figure 2.10: Ion lines as a function of altitude from the experiment done on the 8th of October 2021 (used for illustration). The top panels show standard (not enhanced) ion lines. The bottom panels show an HF induced ion line around 200 km. The scales of the echo power are omitted as this figure is only for illustrative purposes.

3

EISCAT Heating Experiment

This chapter gives an overview of the EISCAT UHF radar, the EISCAT Heating facility and other diagnostic tools used for the experiments detailed in this thesis. Further, the designs of the experiments conducted in October 2021 and March 2022 are presented.

3.1 EISCAT

European Incoherent SCATter Scientific Association (EISCAT) is an organization which operates four research radar facilities located in Kiruna, Sweden, at Ramfjordmoen outside Tromsø, Norway, in Sodankylä, Finland and close to Longyearbyen, Svalbard. The radar facilities are used for conducting experiments in which the ionosphere is investigated. The new experiments detailed in this thesis were conducted at the EISCAT Tromsø site.

The Tromsø site consists of a VHF radar, a UHF radar, and an ionospheric heating facility. The UHF Radar and the heating facility were used in our experiments and are described briefly below.

3.1.1 Heating facility

The EISCAT Heating facility consists of twelve Radio Frequency (RF) transmitters and three antenna arrays. An overview of the facility is sketched in Figure 3.1.

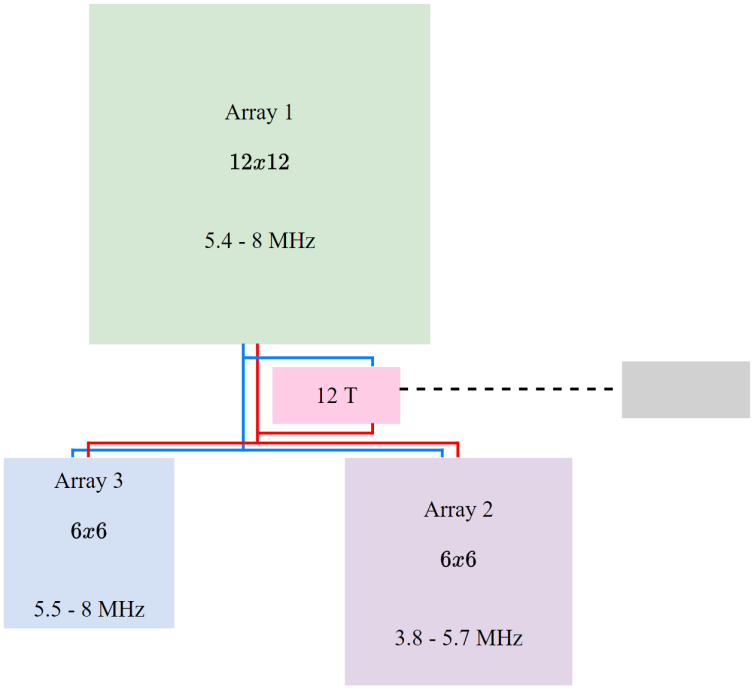

Figure 3.1: Overview of the EISCAT Heating facility. The sketch shows the transmitters (pink), control room (grey), array 1 (green), array 2 (blue) and array 3 (light purple). The blue and red lines show the paths of the co-axial transmission lines connecting the transmitters and the antenna fields. Based on [30].

Each of the twelve transmitters have a peak power of 100 kW, yielding a maximum possible Effective Radiated Power (ERP) of 1200 MW. The antenna gain, and therefore also the ERP, depends on which cross-dipole antenna field is used with the transmitters [29]. The arrays also have different frequency ranges, shown in Figure 3.1. Array 2 was used in the experiments in this thesis. Its specifications are presented in Table 3.1.

Note that the beam width and also the antenna gain increase slightly with frequency. This leads to a frequency dependent ERP. This means that the heat flux reaching the UHR height will increase slightly when the frequency is stepped upwards and decrease slightly when the frequency is stepped downwards.

Frequency range (MHz)	3.8 - 5.7
Number of antennas	6x6
Maximum ERP (MW)	300
Beam width (degrees)	14
Antenna gain (dBi)	≈ 23

Table 3.1: Array 2 specifications

3.1.2 UHF Radar

The UHF radar is used to both transmit and receive radar pulses. The parabolic antenna has a diameter of 32 meters and is fully steerable. Its specifications are presented in Table 3.2.

Frequency band (MHz)	930
Transmitter peak power (MW)	2
Duty cycle (%)	12.5
Minimum pulse length (μs)	1
Maximum pulse length (ms)	10

Table 3.2: UHF radar specifications

3.1.3 Other diagnostic tools

In addition to the UHF radar and the heating facility at the EISCAT Tromsø site, SEE observations were made using the SHIRE-HF antenna system located in Skibotn outside Tromsø, at 69.3° N and 20.4° E. The antenna system consists of a configuration of 6 linear dipole antennas with a crossed dipole antenna at the center. An approximate schematic of the configuration is shown in Figure 3.2.

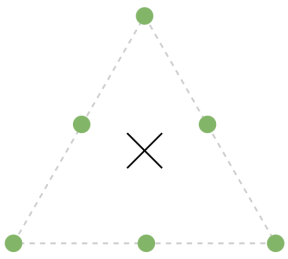

Figure 3.2: Configuration of the 6 linear dipole antennas (green points) and the crossed dipole antenna (black cross) of the SHIRE-HF antenna system.

The antenna system uses Software Defined Radio (SDR) receivers, which means that the system is highly flexible in terms of center frequency, bandwidth, and integration period.

3.2 Experiment design

3.2.1 October 2021

A series of 3 heating experiments were conducted on the 8th, 14th and 15th of October 2021. The experiments were designed to investigate possible hysteresis effects when sweeping the HF pump wave frequency through the third double resonance frequency from below and above. This was done by stepping the frequency in steps of $\approx$ 4.79 kHz every five seconds during HF ON periods. The frequency steps were split into in three partly overlapping sweeps with different frequency ranges. The overlaps make it possible to pass a double resonance frequency in a higher number of sweeps. If the double resonance frequency is passed towards the end of a sweep, it will also be passed in the following sweep.

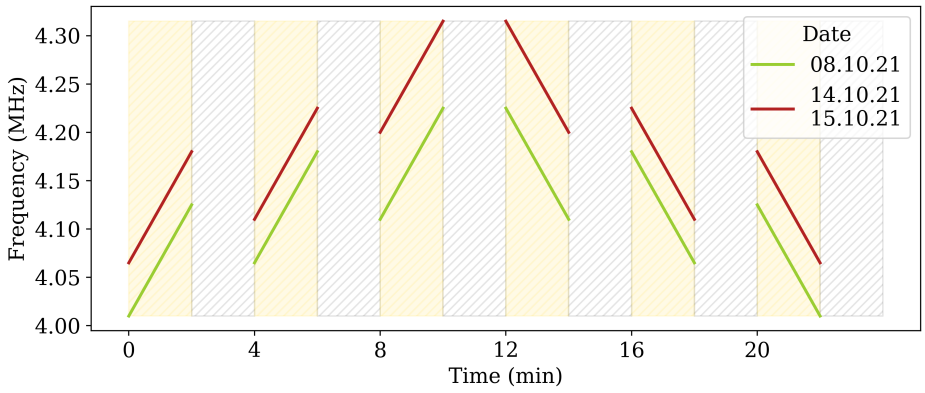

Figure 3.3: Frequency sweeps done on the 8th of October 2021 (green) and the 14th and 15th of October 2021 (red). The yellow regions mark the HF ON periods of 2 min duration where the frequency is swept. Grey shaded regions show the HF OFF periods, also of 2 min duration. One HF ON period plus the following HF OFF period yields one cycle of 4 min duration.

The heater was operated in a 2 min on, 2 min off cycle. Each 2 min on period contain one sweep of 24 frequency steps spanning 115 kHz. The first three sweeps were done with increasing frequency, whereas the following three were done with decreasing frequency. This cycle of 6 sweeps covers

each frequency range twice, once with increasing frequency and once with decreasing frequency. The pattern is shown in Figure 3.3.

The frequency ranges used on the 8th of October 2021 are shown in Table 3.3, and the frequency ranges used on the 14th and 15th of October are shown in Table 3.4. The sweep number denotes the frequency range and the arrow (↑ /↓) denote whether the frequency is swept up or down. The frequencies used on the 14th and 15th are higher than those used on the 8th, because it was noted that the double resonance was passed during the highest frequency sweep during the experiment on the 8th. The ionospheric conditions on the 14th and 15th were similar to those on the 8th, so the frequencies were increased to possibly increase the number of double resonance passes. All sweeps and experiment start and stop times for all three experiments are shown in Figure 3.4. Note that due to an error the overlap between sweeps 3 and 4 is smaller than the overlap between sweeps 2 and 3.

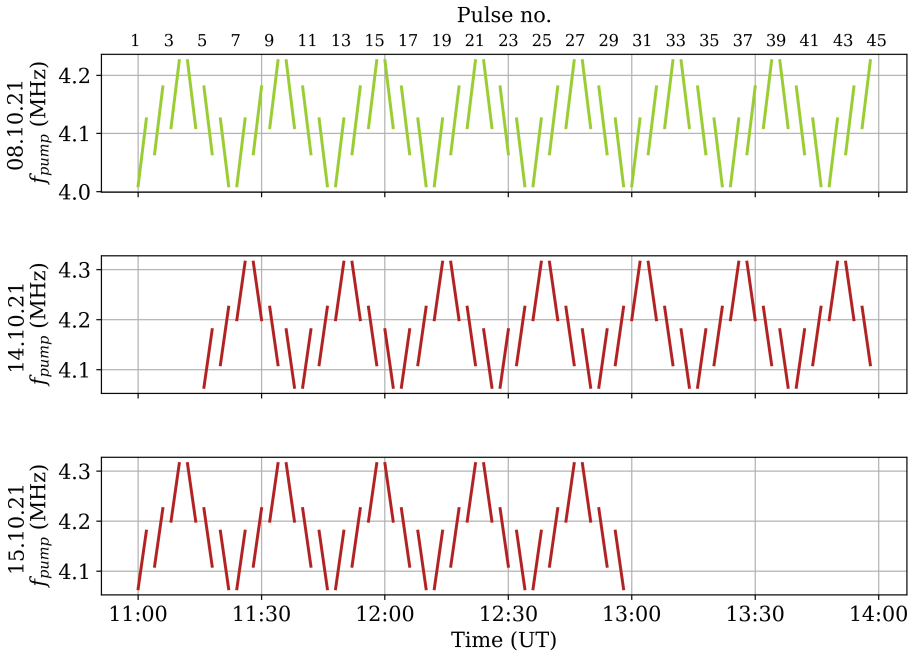

Figure 3.4: Full sweep sequences for the experiments done on the 8th (green) and the 14th and 15th (red) of October 2021.

For each of the three experiments the 12 RF transmitters were transmitting a power of 80 kW. High power yields higher electron heating efficiency [7]. Due to the different frequencies used in the experiments and the frequency dependent gain for the heating antennas, the transmitted ERP was between

171 and 178 MW for the 8th of October 2022 and between 175 and 183 MW for the 14th and 15th of October 2022.

Both the heater and the UHF radar were pointed toward the magnetic zenith because enhancements in temperature are observed to be larger with them both pointed toward magnetic zenith [22, 31]. For the Tromsø facility, which is located at 69.6° N and 19.2°, this is approximately at 12°. The UHF radar ran the Beata pulse coding program. Note that due to a fault in the heater set up the experiment was restarted at 11:16:00 UT on the 14th.

Sweep	Minimum frequency (MHz)	Maximum frequency (MHz)
1↑/1↓	4.010	4.125
2↑/2↓	4.065	4.180
3↑/3↓	4.110	4.225

Table 3.3: Minimum and maximum frequencies for sweeps 1↑/1↓, 2↑/2↓ and 3↑/3↓ used on the 8th of October 2021.

Sweep	Minimum frequency (MHz)	Maximum frequency (MHz)
2↑/2↓	4.065	4.180
3↑/3↓	4.110	4.225
4↑/4↓	4.200	4.315

Table 3.4: Minimum and maximum frequencies for sweeps 2↑/2↓, 3↑/3↓ and 4↑/4↓ used on the 14th and 15th of October 2021.

3.2.2 March 2022

One experiment was conducted on the 16th of March 2022. Its design is different from the experiments done in October 2021. The frequency was stepped in wide frequency ranges to possibly cover both the third and the fourth double resonance. The sweeps and the HF ON/off periods are shown in Figure 3.5 The heater was operated in a 3 min on, 3 min off cycle. The frequency was stepped in steps of 20 kHz every 10 seconds, yielding a total frequency variation of 360 kHz per sweep. Contrary to the experiments in October 2021 the frequency was only swept upwards. The objective was to investigate and compare the frequency variation of the ionospheric electron heating when sweeping the frequency up through the third and fourth double resonance.

The transmitted ERP for this experiment was between 172 MW and 258 MW. The larger gap compared to the series of experiments done in October 2021 is due to the larger range in frequency. As for the experiments done in October 2021, the heater and the UHF radar were pointed towards magnetic zenith. The

UHF radar ran the Beata pulse coding program.

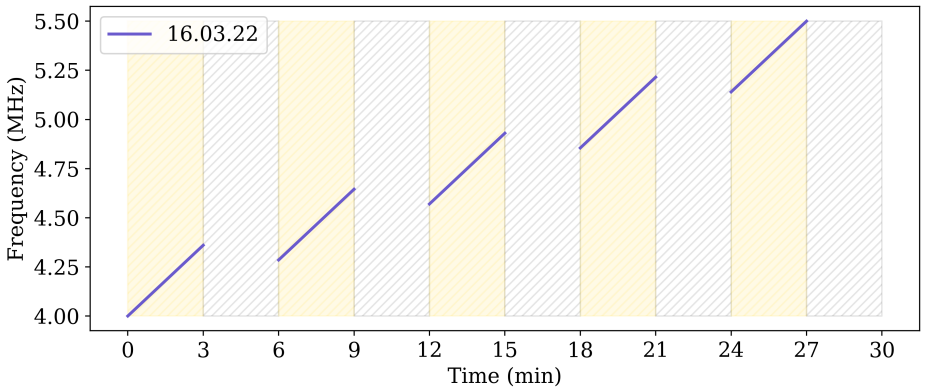

Figure 3.5: Frequency sweeps done on the 16th of March 2022. The yellow regions mark the HF ON periods of 3 min duration where the frequency is swept. Grey shaded regions show the HF OFF periods, also of 3 min duration. One HF ON period plus the following HF OFF period yields one cycle of 6 min duration.

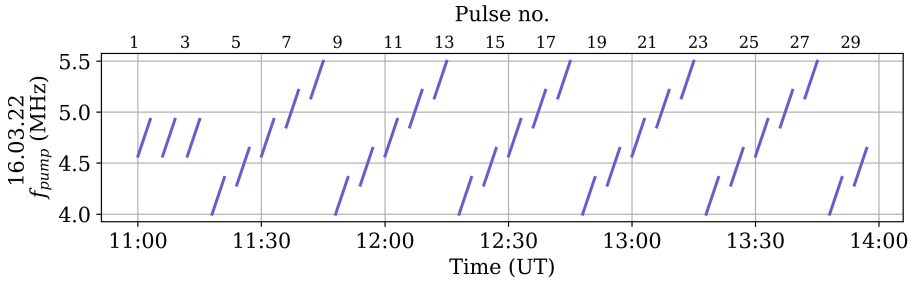

Figure 3.6: Full sweep sequence for the experiment done on the 16th of March 2022.

Sweep	Minimum frequency (MHz)	Maximum frequency (MHz)
A	4.003	4.363
B	4.288	4.648
C	4.573	4.933
D	4.858	5.218
E	5.143	5.503

Table 3.5: Minimum and maximum frequencies for sweeps A, B, C, D and E used on the 16th of March 2022.

The full sweep sequence is shown in Figure 3.6. The sweeps in this experiment will be referred to as sweeps A through E to avoid confusion with the numbering

of the October 2021 sweeps. The specific frequency ranges of sweeps A through E are shown in Table 3.5. Note that due to a fault in the heater set up, sweep C was repeated three times in the beginning of the experiment.

4

Observations

In this chapter the observations from the four EISCAT Heating experiments are presented. In section 4.1 the observed ionospheric parameters are presented. In section 4.2 the observed SEE signatures are presented.

4.1 Ionospheric parameters

Figures 4.1, 4.2, 4.3 and 4.4 show observations from the experiments conducted on the 8th, 14th, 15th of October 2021 and the 16th of March 2022, respectively. The panels, from top to bottom, show the altitude and time variation of (1) the electron temperature T_e, (2) the electron density n_e, (3) the ion temperature T_i and (4) the ion drift velocity v_i. The top panel also show the frequency sweep sequence (white lines) as well as possible resonance frequencies found from the corresponding SEE spectra (pink lines). Segments of these SEE spectra are presented in section 4.2. Figure 4.5 shows closer views of a selection of pulses.

First and foremost, we observe unmistakable enhancements in the electron temperature in the observations from all four experiments. The achieved enhancements reach at most up to 2000 K above the ambient temperatures. It is also clear that the temperatures vary with sweep frequency. The temperature enhancements where the HF pump wave frequency does not pass a double resonance frequency are even throughout the pulse. This is visible in the pulses

starting at 13:20:00 (1↓) and 13:24:00 (1 ↑) on the 8th of October 2021. These two pulses are shown in the top row of Figure 4.5. It is also easy to see that the enhanced temperatures increase with increasing frequency in the observations from the 16th of March 2022. This is likely due to an increase in the pump wave ERP. As described in section 3.2.2 the range in ERP for the March experiment is large, from 172 MW to 258 MW.

The electron temperature enhancements in pulses were the HF pump frequency pass a double resonance frequency can be sorted into two categories. First, there are pulses where we see enhanced temperatures in the beginning and the end of a pulse. This is visible in the pulse stating at 13:56:00 (3 ↑) on the 8th of October 2021 and 12:52:00 (3↓) on the 15th of October 2021. These two pulses are shown in the second row in Figure 4.5. Second, there are pulses in which we only have temperature enhancements on the beginning or the end of the pulse. This is clear in the pulses starting at 12:40:00 (2↑) on the 15th of October 2021 and 12:52:00 (2↑) on the 8th of October 2021. These pulses are shown in the third row in Figure 4.5.

In all four experiments we note generally stable F-region electron densities. n_e decreases slightly over the course of the experiment done on the 8th of October 2021, and it increases slightly over the course of the experiment done on the 15th of October 2021. n_e clearly decreases towards the end of the experiment done on the 14th of October 2021. This is due to observed plasma inflow from the east where the F-region is in night-time conditions with a generally lower n_e. This explains the first increasing temperature enhancements as the HF pump energy is distributed between fewer electrons. As the density decreases further, the F-region critical frequency $foF2$ decreases to below the HF pump wave frequency, which means we no longer get resonant electron heating, as explained in section 2.3.2. This is clearly visible after approximately 13:45:00 where we have no clear temperature enhancements.

The D-region electron densities vary during the experiments done on the 8th and 15th and as expected we have larger enhancements where the D-region density is low. The D-region density is stable during the experiment done on the 15th of October 2021 and enhancements in temperature are lower. On the 16th of March 2022 the D-region density is extremely stable and low. However, the F-region electron density is higher than for the October experiments which explains why the T_e enhancements are not higher in March 2022 than in October 2021.

We also note slight increases in observed electron density during some HF ON periods. First and foremost, we observe small points of significantly higher density at around 200 km during all experiments, most noticeable approximately halfway into the experiment done on the 14th of October 2014.

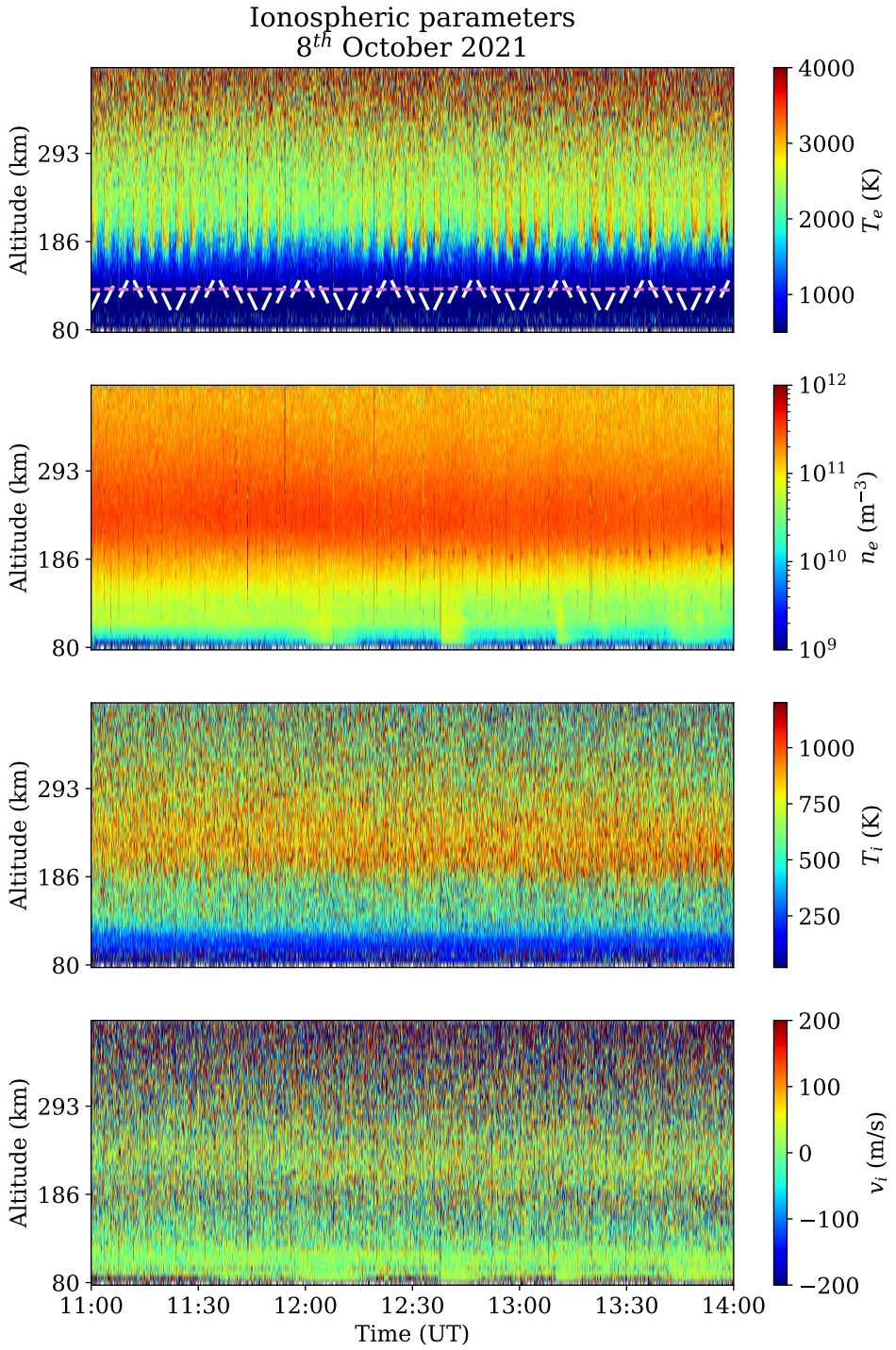

Figure 4.1: Results from the experiment on the 8th of October. The first panel shows the altitude and time variation of the electron temperature T_e, the second panel shows the altitude and time variation of the electron density n_e, the third panel shows the altitude and time variation of the ion temperature T_i and the fourth panel shows the altitude and time variation of the ion drift velocity v_i. The white lines indicate the sweeps in frequency. The pink lines indicate the third double resonance frequency.

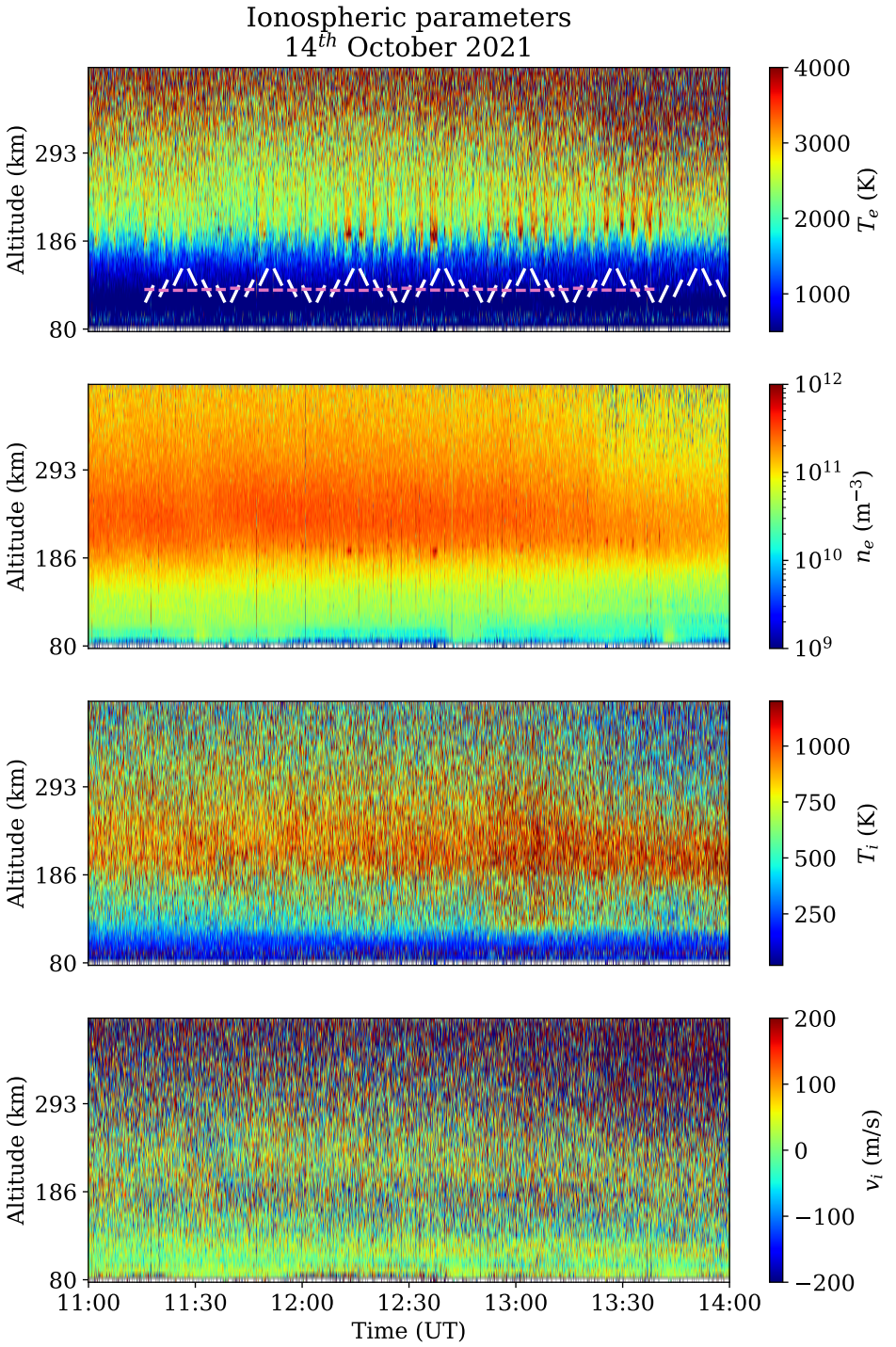

Figure 4.2: Results from the experiment on the 14th of October. The first panel shows the altitude and time variation of the electron temperature T_e, the second panel shows the altitude and time variation of the electron density n_e, the third panel shows the altitude and time variation of the ion temperature T_i and the fourth panel shows the altitude and time variation of the ion drift velocity v_i. The white lines indicate the sweeps in frequency. The pink lines indicate the third double resonance frequency.

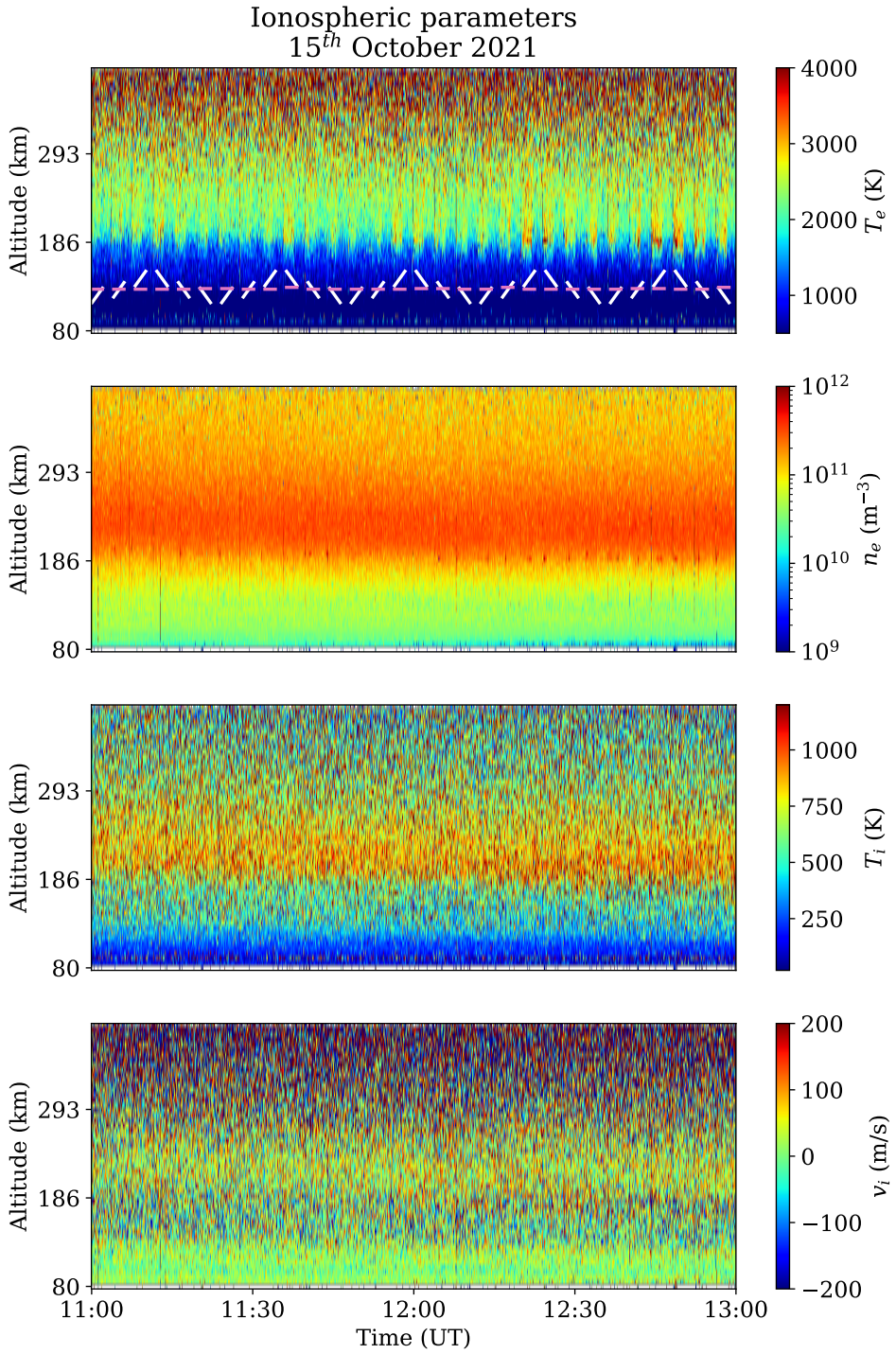

Figure 4.3: Results from the experiment on the 15th of October. The first panel shows the altitude and time variation of the electron temperature T_e, the second panel shows the altitude and time variation of the electron density n_e, the third panel shows the altitude and time variation of the ion temperature T_i and the fourth panel shows the altitude and time variation of the ion drift velocity v_i. The white lines indicate the sweeps in frequency. The pink lines indicate the third double resonance frequency.

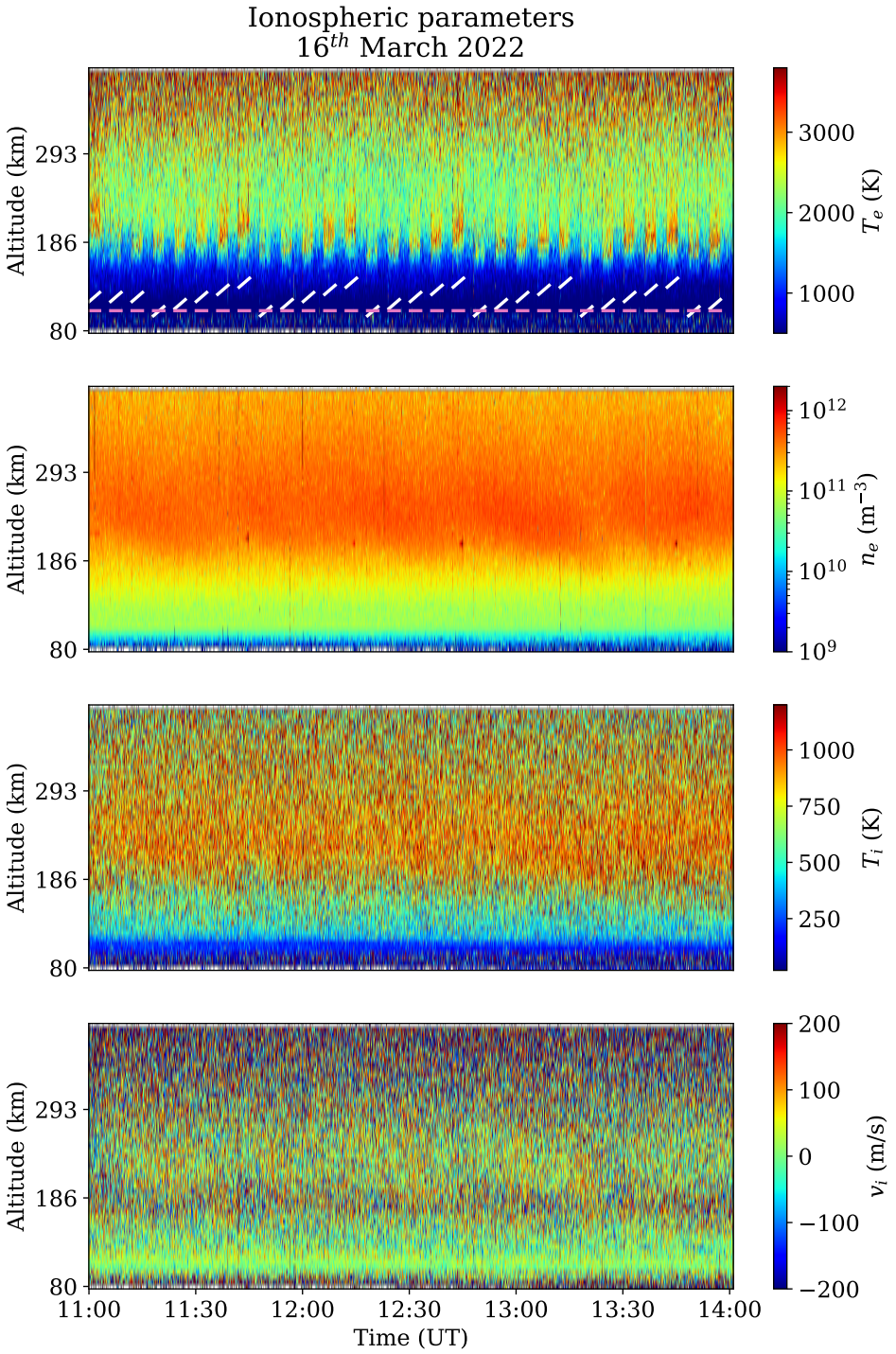

Figure 4.4: Results from the experiment on the 16th of March 2022. The first panel shows the altitude and time variation of the electron temperature T_e, the second panel shows the altitude and time variation of the electron density n_e, the third panel shows the altitude and time variation of the ion temperature T_i and the fourth panel shows the altitude and time variation of the ion drift velocity v_i. The white lines indicate the sweeps in frequency. The pink lines indicate the third double resonance frequency.

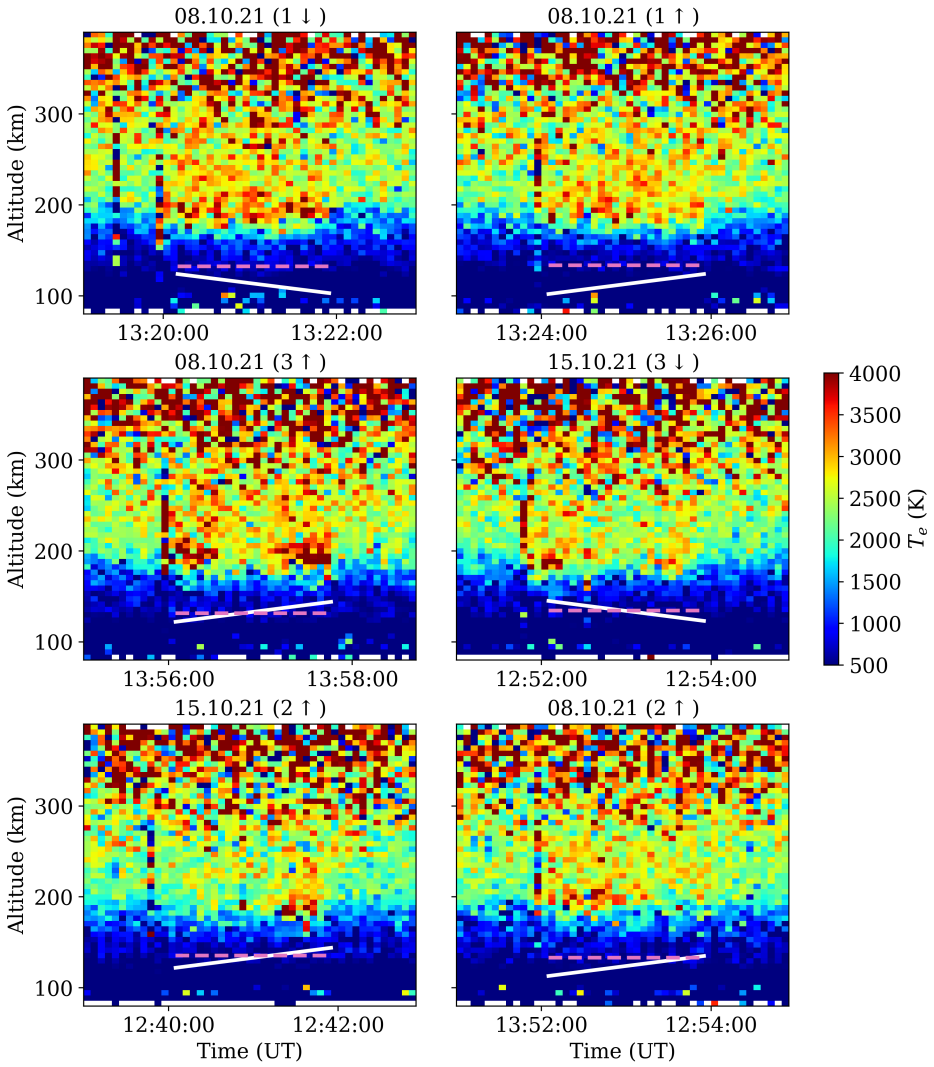

Figure 4.5: Zooms of electron temperatures T_e during 6 selected pulses. The date and sweep number/direction is shown above each plot. The white lines indicate the pump frequency, and the dashed pink lines indicate the third double resonance frequency.

These n_e increases are likely not true increases and simply results of HFIL.

We also see clear variation in the electron density during the experiment done on the 16th of March 2022. The variation seems to be linked to each $A-B-C-D-E$ sweep pattern, in which the temperature increases greatly. The increase in the electron density can be explained by a decrease in the recombination rates due to higher electron temperatures. When the electron temperature increases, the recombination rates in the lower F-region decrease,

leading to higher electron densities [2].

The ion drift velocities fluctuate around and average to zero, and are therefore negligible for all 4 experiments, expect for after 13:45:0 UT on the 14th of October 2021. When integrating equation 2.13 for the electron temperature it is important to recall that it is rewritten for negligible convection due to negligible plasma drifts. This means that the data from 13:45:00 UT in this experiment cannot be used in the further analysis and when integrating 2.13.

4.2 SEE

Figures 4.6, 4.7 and 4.8 show excerpts from the time-frequency spectrograms from the experiments done in October 2021. Each figure contains signatures from 6 sweeps, 1↑, 2↑, 3↑, 3↓, 2↓, 1↓ for the 8th of October, 2↓, 2↑, 3↑, 4↑, 4↓, 3↓ for the 14th of October and 2↑, 3↑, 4↑, 4↓, 3↓, 2↓ for the 15th of October.

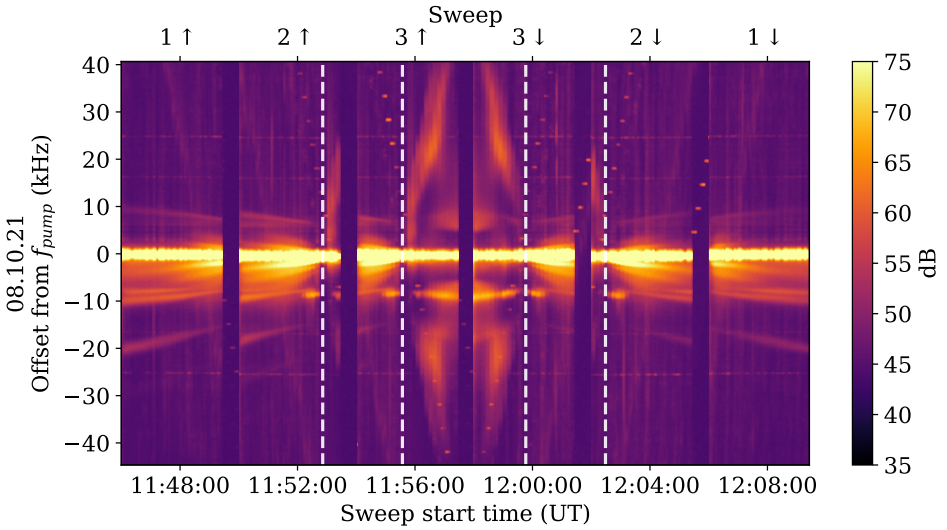

Figure 4.6: SEE spectrogram from the experiment done on the 8th of October 2021. The frequency axis shows the offset from HF pump frequency f_{pump}. The white dashed lines show where the HF pump frequency passes the third double resonance frequency.

The dashed white lines indicate where the HF pump frequency passes the third double resonance frequency. We see this where the DM cease to exist and BUM appear when sweeping the frequency up, and where the BUM cease to exist and the DM appear when sweeping the frequency down. Because we pass the third double resonance both when sweeping the frequency up and down in all three experiments, it should be possible to investigate possible asymmetry

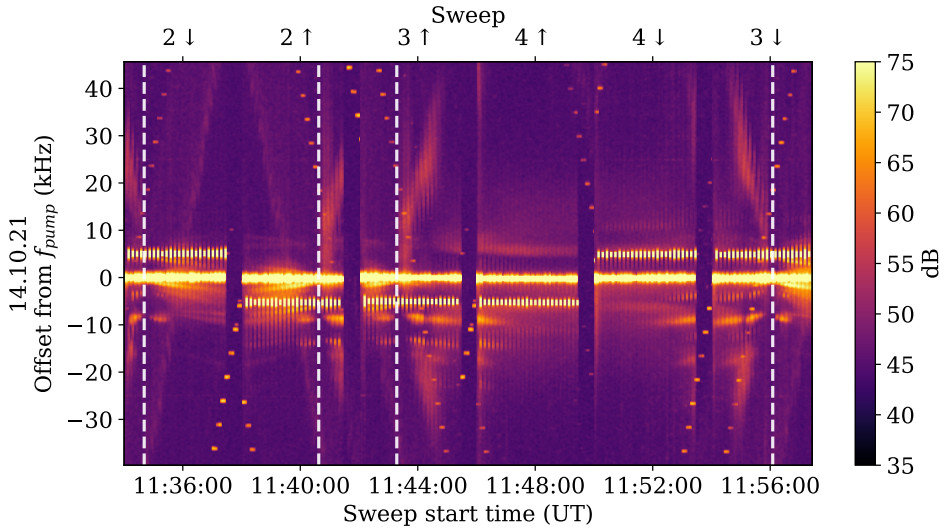

Figure 4.7: SEE spectrogram from the experiment done on the 14th of October 2021. The frequency axis shows the offset from HF pump frequency f_{pump}. The white dashed lines show where the HF pump frequency passes the third double resonance frequency.

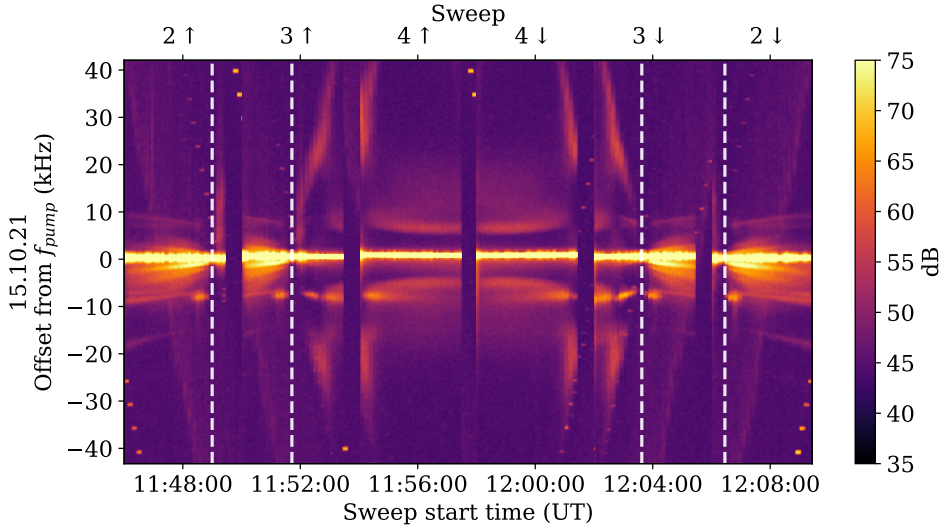

Figure 4.8: SEE spectrogram from the experiment done on the 15th of October 2021. The frequency axis shows the offset from HF pump frequency f_{pump}. The white dashed lines show where the HF pump frequency passes the third double resonance frequency.

in ionospheric electron heating when the frequency is swept up and down through the third double resonance frequency.

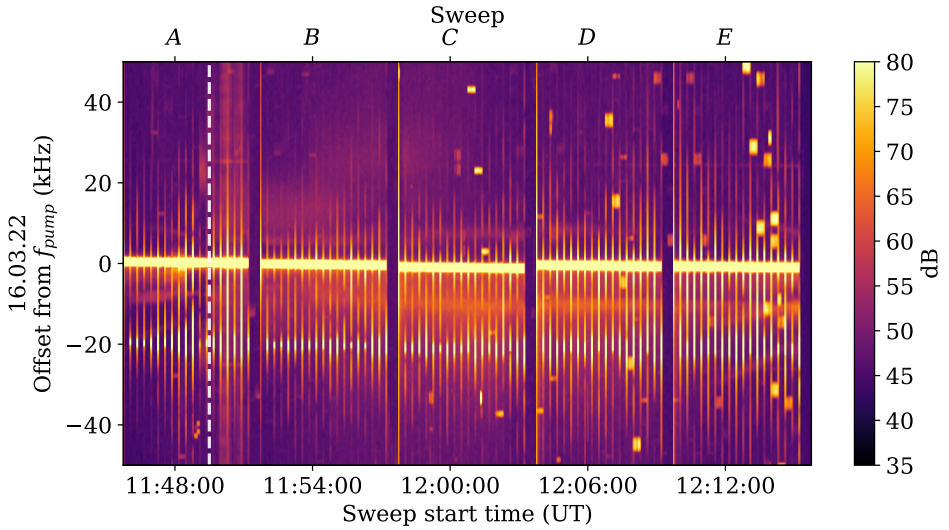

Figure 4.9: SEE spectrogram from the experiment done on the 16th of March 2022. The frequency axis shows the offset from HF pump frequency f_{pump}. The white dashed lines show where the HF pump frequency passes the third double resonance frequency.

Figure 4.9 shows an excerpt from the time-frequency spectrogram from the experiment done on the 16th of March 2022 and include, in order, sweeps A, B, C, D and E. Despite the signatures being less clear than in the spectrograms from October 2021, we note that we pass the third double resonance in sweep A. This is indicated by the dashed white line. However, we see no indications of passing the fourth double resonance. DM are visible for the entire spectrogram, expect where we pass the third double resonance. Unfortunately, this means that we do not have grounds for comparing electron heating around the third and fourth double resonance. Because the fourth double resonance is not passed and the third double resonance is only passed a few times compared to the number of passes in the experiments done in October 2021, the data from the 16th of March is omitted from the further analysis.

5

Data Analysis Method

This chapter details the method which was used to model the heat source of interest, $Q_{\mathrm{HF}}(t, z)$. In short, the method can be summarized as follows. First, estimates for background heat sources $Q_{\mathrm{o}}(z)$ are found through non-linear least squares fitting of model electron temperatures to the experimentally observed temperatures during HF OFF periods. Next, estimates for Q_{HF} are found following the same procedure as for Q_0, only for each step in time, or frequency, during HF ON periods. Second, the electron temperature models are found by integrating the one-dimensional electron energy equation without convection for the electron temperature, using the fitted heat sources. Third, the parameter uncertainties of the fitted parameters are estimated. However, before the parameter fitting can be performed, several necessary preprocessing steps are required.

This chapter is structured in the following way. First the preprocessing of the raw data is described. Next the method for solving the electron energy equation is presented, along with chosen boundary conditions. Following that, the methods used for estimating the heat background heat source Q_0 and HF heat source Q_{HF} are detailed. Finally, the method for estimating the parameter uncertainties is presented.

5.1 Preprocessing

Several steps of data preprocessing were necessary before modeling the electron temperature and estimating the heat sources Q_0 and Q_{HF}: (1) Analysis of the UHF radar data with GUISDAP, (2) filtering out HFIL, (3) estimating thermospheric and ionospheric neutral and ion densities with MSIS and IRI models and (4) filtering the observed ionospheric parameters. These steps are described briefly below.

The data from the three experiments in October 2021 was analyzed using GUISDAP (Grand Unified Incoherent Scatter Design and Analysis Package) [25], which is used for estimating n_e, T_e, T_i and v_i from raw data from the EISCAT radars. The analysis was done with an integration time of five seconds. This short integration time is chosen to match the frequency stepping of the experiments. In October 2021, the HF pump frequency was, as mentioned, stepped in steps of five seconds, which means that the maximum integration time we could use is five seconds. By default, GUISDAP uses range gates that increase in size with altitude. To maintain the range resolution necessary to detect the narrow observed T_e enhancements around the UHR height, we overrode this with range gates of 6 km for all altitudes. This also means that we do not need to consider variable range gate sizes in the further analysis.

As described in section 2.4.2, HFIL give rise to inaccurately large n_e and T_e estimates. Therefore, it is necessary to remove the measurements corresponding to these HFIL. The removal was done by visual inspection of every single ion spectrum in every 2-minute HF ON period. A visual inspection should be sufficient since the HFIL are clearly distinguishable from non-enhanced ion lines, as shown in Figure 2.10. All measurements in n_e and T_e corresponding to HFIL were replaced with interpolated values based on the remaining data.

Models for the background atmosphere and thermospheric and ionospheric ion compositions were collected from the Mass Spectrometer and Incoherent Scatter radar (MSIS) model [12] and the International Reference Ionosphere (IRI) model [11]. These models are necessary for estimating energy loss to neutrals and ions when solving the electron energy equation. The magnetic field strength was collected from the International Geomagnetic Reference Field (IGRF) model [10] and was used for calculating the electron cyclotron frequency.

At the time when the data analysis was started, the MSIS model for October 2021 was unavailable, and the model for October 2020 was therefore used in the analysis. This should yield accurate seasonal variation. Figure 5.1 show MSIS neutral densities from the 8^{th} of October 2020 and 2021. It is clear that the densities from 2021 are slightly larger than those from 2020, especially at

higher altitudes. However, at around the reflection height at approximately 210 km, the increase in n_{N_2} and n_{O_2} is about 15% while the increase in n_O is about 5%. This can be explained by an increase in solar activity between 2020 and 2021 as we are currently in the beginning stages of the current solar cycle [37], where the solar activity increases. The density of heavier neutral constituencies, like N_2, increase at high altitudes with increased solar activity [5].

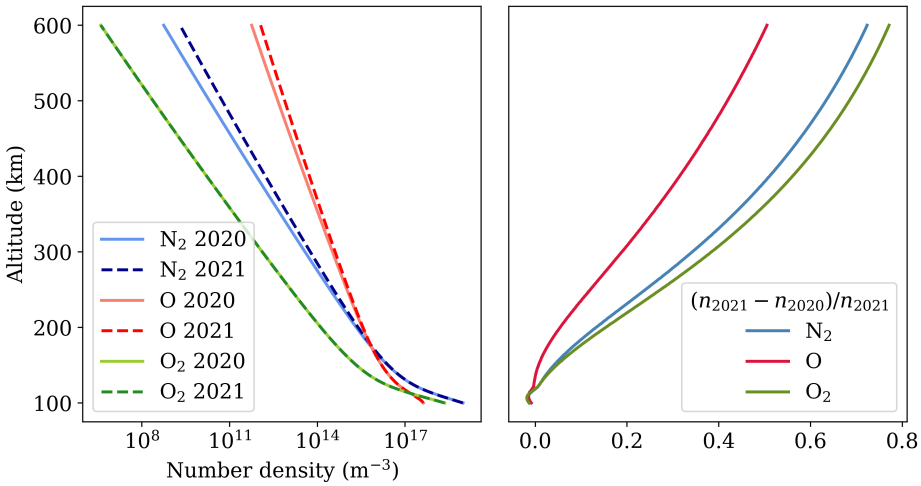

Figure 5.1: Comparison of MSIS neutral densities from 2020 and 2021. The left panel shows neutral densities from 2020 (solid) and 2021 (dashed). The right panel shows the relative difference between the densities from 2020 and 2021.

Figure 5.2 shows the difference in cooling rates for an enhanced electron temperature profile (shown in Figure 2.8) using MSIS neutral densities for 2020 and 2021. The cooling rates increase slightly when using the model for 2021 which is expected when the neutral densities increase. However, the increase is small and slowly increasing with altitude. The increase in total loss to neutrals around the peak cooling altitude is only 8 % when using the 2021 model instead of the 2021 model. Because the difference is small and the difference between the loss rates increase only slightly with altitude, it is safe to assume that using the 2020 model for our 2021 experiment will not affect the shape of the resulting HF heat sources. However, the magnitudes of the resulting heat rates will be affected by a small correction factor.

The GUISDAP estimates for T_i and n_e were noisy due to the short integration time and fine altitude resolution. Therefore, the T_i and n_e estimates were filtered. The filtering is done because T_i and n_e are used for calculating the coefficients of the electron energy equation (equation 2.13), and numerical

PDE solvers can be sensitive to sharp gradients in these coefficients. T_i and n_e were filtered using a cubic splines interpolation with a maximum number of knots $n_{\text{knots}} = 41$. The ideal number of knots were chosen from an average of the minima of several criteria that were compared, namely the Akaike Information Criterion (AIC), the Bayesian Information Criterion (BIC), the fits of two estimated probability density functions, and finally the size of the deviation of the estimated standard deviation from 1.

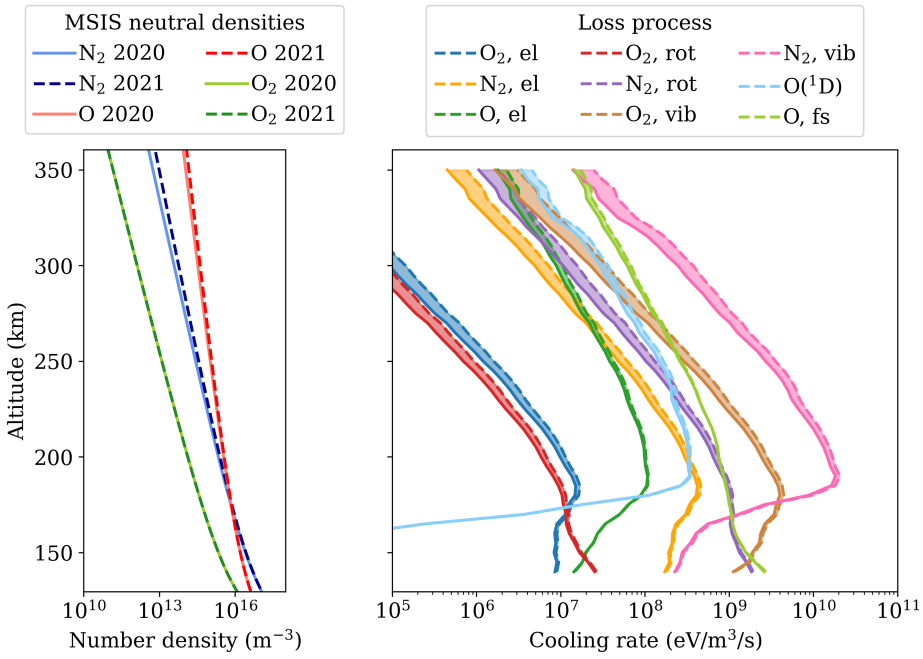

Figure 5.2: Electron energy losses to neutrals using MSIS densities for October 2020 (solid) and 2021 (dashed).

In addition to the steps described above, we attempted to estimate n_e from the plasma lines. This was attempted because n_e estimates from the plasma line spectra can yield a much smaller uncertainty than the resulting n_e from the GUISDAP analysis [29]. However, this was unfruitful. As explained in section 2.4.2, the plasma lines are weak and difficult to measure. The plasma line spectra were only visible in some time intervals throughout the experiments and only with an integration time of 120 seconds. Therefore we were forced to use the standard GUISDAP electron density estimates.

5.2 Solving the electron energy equation

Equation 2.13 cannot be solved directly for the heat sources Q_{HF} and Q_0. This is because EISCAT measurements of n_e, T_e and T_i are noisy, which leads to significantly high error propagation in the gradient terms. Instead, parameterizations for Q_{HF} and Q_0 are assumed. The free parameters $\boldsymbol{P}$ for each HF ON or HF OFF period are fitted by solving equation 2.13 for the modeled temperature $\tilde{T}_e$ and minimizing the error between the observed T_e and the modeled $\tilde{T}_e$ through weighted non-linear least squares minimization, that is

$$\boldsymbol{P} = arg\min_{P} \sum (\tilde{T}_e - T_e)^2 w(T_e) \tag{5.1}$$

where the weight w is

$$w(T_e) = \frac{1}{\sqrt{\sigma(T_e)}} \tag{5.2}$$

where $\sigma(T_e)$ is the standard deviation of the observed T_e. Weighting the summation ensures that the most certain observations have a larger influence on the minimization process while less emphasis is put on the more uncertain measurements. Note that the root of the standard deviation is taken, instead of the square which is typically used in weighing. This is done because the standard deviations of our HF enhanced temperatures are large compared to our background temperatures. Using the square of the standard deviation would therefore seriously out-weight the enhanced T_e. This is undesirable. The best solution to this issue would be to possibly use another maximum likelihood function instead of least-squares. However, finding the optimal maximum likelihood function is far beyond the scope of this thesis. The approach using non-linear least squares was developed by Senior et al. [35] and Bryers et al. [6] for steady state and extended to the time dependent case by Leyser et al. in 2020 [22].

Equation 2.13 is integrated iteratively for T_e using a Green's function approach with a second order Runge-Kutta method. For the sake of explanation, it is convenient to rewrite equation 2.13 as follows

$$A(t, z, \tilde{T}_e)\frac{\partial \tilde{T}_e}{\partial t} = F(t, z, \tilde{T}_e)\frac{\partial^2 \tilde{T}_e}{\partial z^2} + S(t, z, \tilde{T}_e) \tag{5.3}$$

where A is the heat capacity, F is the heat conductivity, $S = Q - L$ is the difference

between the electron heating and cooling rates, and $\tilde{T}_e$ is the solution: the modeled electron temperature.

For each half-time step for each iteration in the Runge-Kutta scheme, heat transfer due to diffusion is included in the solution through multiplication with a *Green's function matrix* G_M, which is a function of the diffusion coefficient F. This method was developed by Gustavsson et al. in 2010 [17]. Note that if the heat transfer due to convection was not negligible, the Green's function matrix would be a function of both the diffusion coefficient F and some convection coefficient.

5.2.1 Shape of the PDE solution

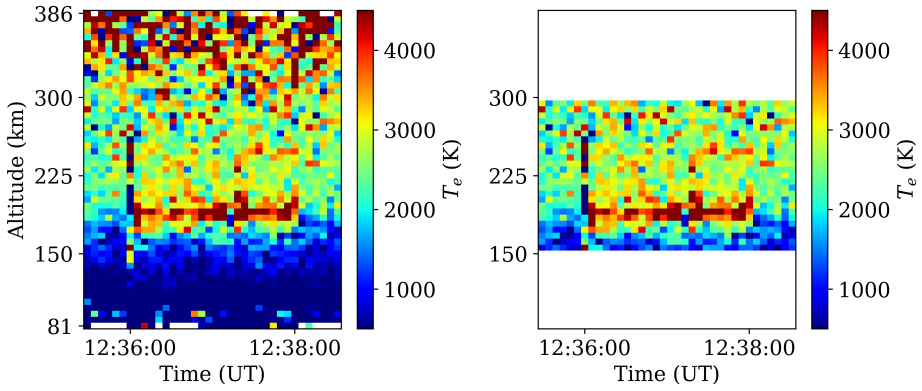

Figure 5.3: Observed temperatures during a HF pulse on the 14th of October 2021 (left) and the slice in altitude used when solving the electron energy equation (right).

For the PDE solution we chose an altitude range of 150 km to 300 km. Because the region of enhanced T_e in our experiments are not as wide in altitude as in some night-time experiments (e.g. [31]), this was unproblematic. From the observation (Figures 4.1 - 4.4) it is clear that the range covers the temperature enhancements well. The relatively low upper boundary was necessary to keep the parameter fitting scheme from attempting to fit HF and background parameters to high temperature noise at high altitudes. Leaving the noisy, high altitudes in the analysis and parameter search could lead to the fitting scheme fitting inaccurate heat sources to this noise.

Figure 5.3 shows observed temperatures during a HF ON period on the 14th of October 2021 and the altitude range of interest that is used to fit the modeled temperatures. It is clear that the temperature enhancements are kept safely

within the altitude range, and that high temperature noise at high altitudes is cropped out.

5.2.2 Time step size dependence

The size of the time step dt in our Runge-Kutta scheme is adaptive and is calculated based on the current temperature $\tilde{T}_e^C$. Larger $\tilde{T}_e^C$ leads to smaller dt^D and smaller $\tilde{T}_e^C$ leads to larger dt^D. Expressed via the diffusion coefficient $D = F(t, z, \tilde{T}_e^C)$, the dependency of dt^D is

$$dt^D \propto \frac{1}{\sqrt{4D}} \tag{5.4}$$

Further, the maximum time step is found as the maximum of the diffusion dependent dt^D and time interval of the solution divided by 5000. Finally, the maximum time step $dt_{\max}$ is set to the half of this value, that is

$$dt_{\max} = \frac{1}{2} \max \left[dt^D, \frac{(t_{\text{initial}} - t_{\text{final}})}{5000} \right] \tag{5.5}$$

This constraint is applied to reduce computation time, and in general the constraint given in 5.5 works well. However, in some cases the time step dt can be forced to be larger than it should be according to its temperature dependence, i.e. we need a smaller dt to solve the PDE accurately. An illustration of this is shown in Figure 5.4. It is clear that a larger dt can yield physically inaccurate temperatures when solving 5.3, most severely in the case of *negative* temperatures. The top panel shows curves where the same heating-cooling (shown in the second panel) is applied, but with different time steps $dt_1 = 5 \cdot 10^{-7}$ and $dt_2 = 2 \cdot 10^{-6}$. We clearly see that dt_2 yields negative temperatures, while dt_1 does not. Both these time steps are smaller than $dt_{\max} = 5 \cdot 10^{-4}$, calculated from equation 5.5 with $t_{\text{final}} - t_{\text{initial}} = 5$ s. This $dt_{\max}$ is significantly larger than both dt_1 and dt_2.

Not applying the constraint in equation 5.5 will lead to significantly larger computation times when doing the analysis and parameter search. However, such large computation times are incompatible with the short deadline for this project. Instead, a constraint was put on the integrated temperature $\tilde{T}_e$ after each addition of heating-cooling. This constraint is shown in Figure 5.4. It is assumed that the temperature can (1) not decrease by more than 1000 K over each step of the solver and that it can (2) not be below 500 K. Solutions $\tilde{T}_e$ that cross this constraint curve are cropped. This is also shown in Figure

5.4. Though effective, this is not the best method for solving this issue, e.g. it would be more accurate to also include a constraint on higher temperatures. For instance, constraint no. 1 that is used on decreasing temperatures could also be applied to increasing temperatures.

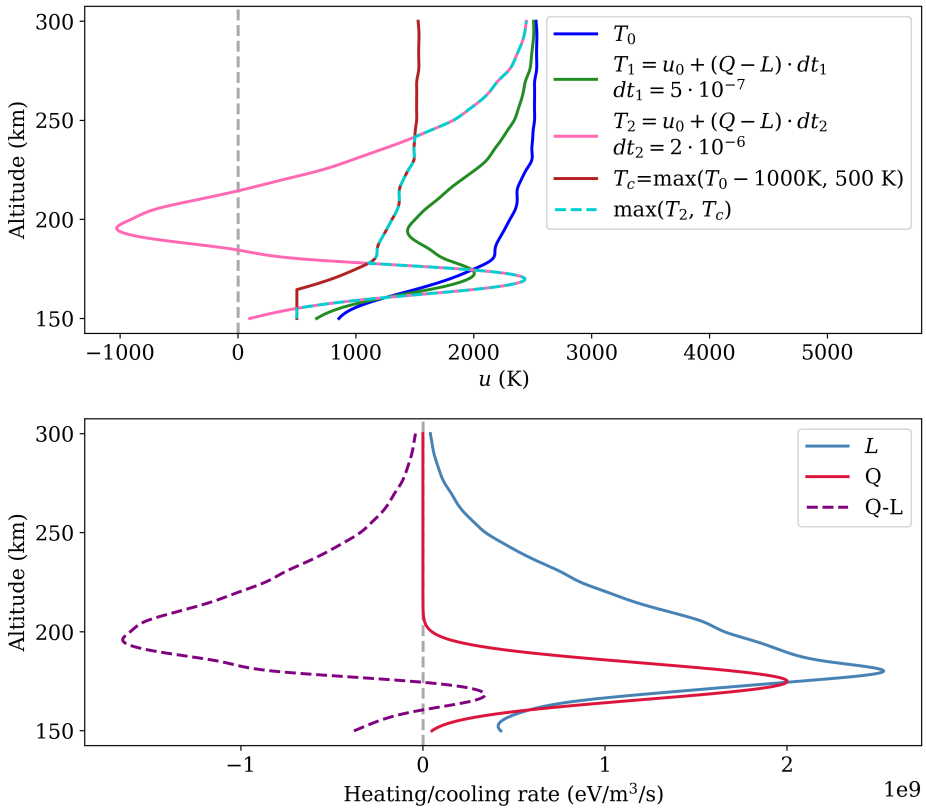

Figure 5.4: The dependence on time step size dt when integrating equation 5.3. The bottom panel shows a heat source Q (red) and a loss rate L (blue), as well as the total heating-cooling rate $Q - L$ (dashed purple). The top panel show an initial condition temperature profile T_0 (blue), resulting temperature curves after applying heating-cooling with a time step dt of (1) $5 \cdot 10^{-7}$ (green) and (2) $2 \cdot 10^{-6}$ (pink), constraint curve T_c (red) and the result of cropping T_2 by T_c (dashed turquoise).

5.2.3 Boundary conditions

The PDE solution is bound by upper and lower boundary conditions. Ideally the upper boundary condition is that the gradient of the electron temperature is zero, that is

$$\frac{\partial}{\partial z} T_e(z_{\text{upper}}) = 0 \tag{5.6}$$

This is a valid boundary condition under the assumption that z_{upper} is at the height where the gradients in the electron temperature is approximately zero during both HF OFF and HF ON periods.

A gradient boundary condition is not always suitable [16]. Because of the high noise levels in the measurements at high altitudes, the maximum altitude $z_{\text{upper}} = 300$ km when solving equation 5.3 is significantly lower than the $z_{\text{upper}} = 500$ km used by Senior et al.[35].

As an alternative we used a fixed value K_{UB} as the upper boundary condition, that is

$$T_e(z_{\text{upper}}) = K_{\text{UB}} \tag{5.7}$$

where the constant K_{UB} is given by the mean of the upper observed temperatures on the interval on which we are solving equation 2.13. In some cases, a fixed value K_{UB} is also unsuitable. If the enhancements in temperature reach the top of the PDE altitude range, the upper boundary condition will not remain constant. However, as it is shown in Figure 5.3, this is not the case for our experiments.

The neutral temperature T_n can be used as the lower boundary condition, that is

$$T_e(z_{\text{lower}}) = T_n(z_{\text{lower}}) \tag{5.8}$$

It is visible in Figure 2.3 that the electron temperature and the neutral temperature is approximately equal below approximately 120 km. However, as the bottom of the PDE altitude range is 150 km, this boundary condition is unsuitable.

As for the upper boundary condition, the lower boundary condition is also a fixed value which is

$$T_e(z_{\text{lower}}) = K_{\text{LB}} \tag{5.9}$$

where the constant K_{LB} is the mean of the lower observed temperatures on the current interval. The assumption that the temperatures at the bottom of the altitude range remains constant is valid because the observed temperature enhancements does not reach altitudes $\leq$ 170 km. This is visible in Figure 5.3 and in the observed parameters (section 4.1).

5.3 Background heat source

In order to be able to estimate Q_{HF}, it is necessary to first estimate the background heat source Q_0. The estimate of Q_0 is based on HF OFF periods, that is periods where we have no HF heating and therefore only background heating. If we have quiet geophysical conditions, the background heat source only varies with solar zenith angle. Therefore, we can assume that we have steady state conditions during the second half of each two-minute HF OFF period. This means that we assume that Q_0 remains constant with time in these periods, and it is therefore only necessary to make one estimate for Q_0 per HF OFF period.

The heat source Q_0^i for each HF OFF period i is assumed to be on the form

$$Q_0^i = C_0^i \cdot Q_{BG}^i \tag{5.10}$$

where Q_{BG}^i is an estimation of the background heat source made directly from the observed ionospheric parameters and C_0^i is a scaling factor. The methods to find Q_{BG}^i and C_0^i are described below.

First an initial estimate Q_{BG}^i is made based on the observed parameters during HF OFF period i. This estimate is made by solving the electron energy equation for the background heat source under the assumption that Q_{HF} is zero, which clearly is an acceptable assumption during HF OFF periods. This results in

$$Q_{BG}^i = \frac{3}{2} k_B n_e^i \frac{\partial T_e^i}{\partial t} - \frac{\partial}{\partial z}\left(\kappa_e \frac{\partial T_e^i}{\partial z}\right) + L_{BG}^i \tag{5.11}$$

where n_e^i is the observed electron density, T_e^i and T_i^i are the observed electron and ion temperatures and L_{BG}^i is the electron cooling rates calculated from the observed n_e^i, T_e^i and T_i^i as well as the background atmosphere and ionosphere models. Further, we assume that Q_{BG}^i can be parameterized as a Chapman function. The parameters to this Chapman function are found by fitting the

parameters to the initial estimate for Q^i_{BG}.

The scaling factor C^i_0 is found by non-linear least squares fitting, where the modeled temperatures for each HF OFF period i, $\tilde{T}^i_e$, is fitted to the observed temperatures T^i_e. The best fitted C^i_0 minimizes the error between the modeled temperature and the observed temperature

$$C^i_0 = arg\min_{C_0} \sum (\tilde{T}^i_e - T^i_e)^2 w^i(T^i_e) \tag{5.12}$$

where the weight $w^i(T^i_e)$ is given by equation 5.2.

When searching for the scaling factor C_0, another scaling factor is also fitted. This is an upper boundary condition scaling factor CdT_e. This is necessary because the estimate Q_{BG} only considers internal ionospheric heat gain and energy loss, and heat flux down at the top boundary is therefore not included. To include the effect of this heat flux, the scaling factor CdT_e is included. This allows the parameter fitting scheme to adjust the temperature at the upper boundary to include changes due to this heat flux. Rewriting equation 5.12 to include the boundary condition scale factor CdT_e results in the complete background parameter error minimization

$$\boldsymbol{P}^i_{\mathrm{BG}} = arg\min_{\boldsymbol{P}_{\mathrm{BG}}} \sum (\tilde{T}^i_e - T^i_e)^2 w^i(T^i_e) \tag{5.13}$$

where $\boldsymbol{P}^i_{\mathrm{BG}} = \begin{bmatrix} C^i_0 & CdT^i_e \end{bmatrix}$.

5.3.1 Initial condition

As explained previously, it is safe to assume that we have steady state conditions during each 2-minute HF OFF period. Because we can assume steady state, we use the mean of the observed T_e for each HF OFF period as the initial condition for $\tilde{T}_e$ when solving for each HF OFF period. The mean is taken for the last half of each HF OFF period. This ensures that the heating effects have dissipated and that we have returned to steady state conditions.

5.4 HF heat source

To model the HF heat source Q_{HF} we assume that the heat source is a two-sided Gaussian with individual half-widths above and below the peak altitude z_{peak}

$$Q_{\mathrm{HF}}(z) = Q_{\mathrm{peak}} \exp -\zeta^2 \tag{5.14}$$

where

$$\zeta = \begin{cases} (z - z_{\mathrm{peak}})/\Delta z_U & z > z_{\mathrm{peak}} \\ (z - z_{\mathrm{peak}})/\Delta z_L & z \leq z_{\mathrm{peak}} \end{cases} \tag{5.15}$$

where z_{peak} is the peak altitude, Δz_L and Δz_U are the half-widths below and above the peak altitude and Q_{peak} is the peak heating rate. In this model of the HF heat source, we do not include a rise time, τ, as done by Leyser et al. [22]. Their experience was that it was difficult to estimate τ from GUISDAP estimates with a five second integration time. To estimate τ we would also need to consider several succeeding steps in time, which is not possible because we consider only one five second step in time at once. However, as we are investigating frequency dependence when passing the double resonance within a pulse, the rise time is of no interest for our purposes.

Just as for the background heat source Q_0, the parameters of Q_{HF} are found by non-linear least square fitting. The minimization for each HF ON period i and five second time step j can be expressed as

$$\boldsymbol{P}^i_{\mathrm{HF,\,j}} = arg \min_{\boldsymbol{P}_{\mathrm{HF,\,j}}} \sum (\tilde{T}^i_{e,j} - T^i_{e,j})^2 w^i_j(T^i_j) \tag{5.16}$$

where $\boldsymbol{P}^i_{\mathrm{HF,j}} = \begin{bmatrix} Q^i_{\mathrm{peak,j}} & z^i_{\mathrm{peak,j}} & \Delta z^i_{D,j} & \Delta z^i_{U,j} \end{bmatrix}$.

The parameters $\boldsymbol{P}^i_{\mathrm{HF,j}}$, from here on denoted $\boldsymbol{P}^i_{\mathrm{j}}$, are shown in Figure 5.5. We assume that the parameters $\boldsymbol{P}^i_j$ are similar to the parameters in the previous step $\boldsymbol{P}^i_{j-1}$. Because of this similarity we use parameters $\boldsymbol{P}^i_{j-1}$ as initial guesses for the next set of parameters $\boldsymbol{P}^i_j$.

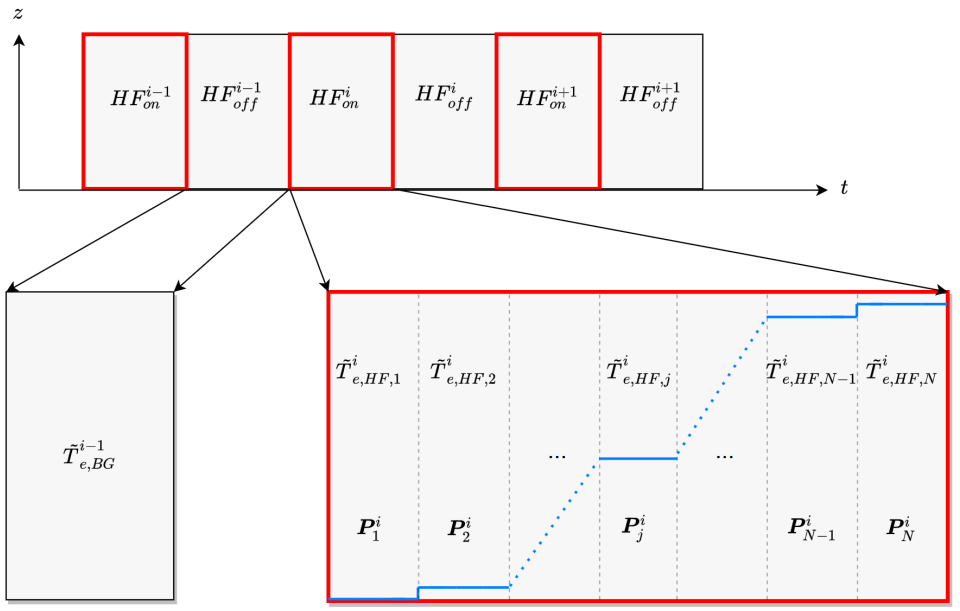

Figure 5.5: Parameters $\boldsymbol{P}^{i}_{j}$ for each five second time interval j in each HF ON period i. $T^{i-1}_{e,BG}$ is the modeled electron temperatures from the previous HF OFF pulse $i-1$ and is used as the initial condition for $T^{i}_{e,HF,1}$ when searching for parameters $\boldsymbol{P}^{i}_{1}$. The blue steps show the steps in frequency.

As shown in Figure 5.3, the data that we are trying to fit the model to is noisy. The noisy data results in seemingly random half-widths and z_{peak} with no connection to the previously found parameters. To attempt to resolve this issue the parameters of step j was allowed to vary within a region around the parameters in step $j-1$. The parameters in step $j=1$ were allowed to vary within a significantly larger region, including all reasonable values for the parameters. The smaller, constrained region can be expressed as

$$\boldsymbol{P}^{i}_{\text{j, region}} = \boldsymbol{P}^{i}_{j-1} \pm \delta \boldsymbol{P} \tag{5.17}$$

Where $2\delta\boldsymbol{P}$ is the size of the smaller region.

If a parameter increases toward the upper bound of the initial region, the upper bound of the new smaller interval $P + \delta P$ can be larger than the upper bound of the initial region. The same can happen for the new lower bound $P - \delta P$ if the parameter P decreases toward the lower bound of the initial region. This is not desirable as the initial interval is meant to cover all excepted or reasonable values for the parameter P. To resolve this issue the smaller regions are put

under the constraint that their upper bounds cannot exceed the upper bound of the initial region. Similarly, their lower bounds cannot be lower than the lower bound of the initial region. The resulting intervals after cropping at the initial bounds are shown as red, dashed rectangles in Figure 5.6. These intervals were used in the parameter search done in this thesis.

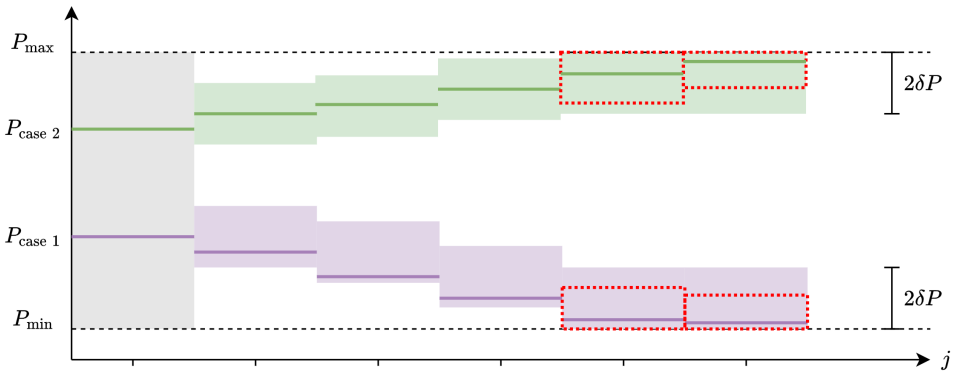

Figure 5.6: Parameter intervals based on the previous parameter P. $P_{\max}$ and $P_{\min}$ show the upper and lower bounds on the initial interval. $P_{\text{case 1}}$ (purple) and $P_{\text{case 2}}$ (green) illustrate two cases for the parameter search. In case 2 the parameter P increases toward the initial upper bound. The new interval is clipped at the upper bound and extended in the lower end to keep the width of $2\delta P$. Case 1 show the same as case 2, only when the parameter P decreases toward the lower initial bound. For both cases the dashed, red boxes show intervals that are cropped, but not extended.

However, the constraint raises a new possible issue. If the parameter P is considerably close to one of the initial bounds, the new interval can become very narrow. A too narrow interval will not give enough room for the next parameter to vary sufficiently. To alleviate this, a better and improved scheme could be implemented. The new intervals could be put under a second constraint: that is the new interval must have size $2\delta P$. This means that the bounds of the smaller regions can be shifted to fit a $2\delta P$ sized region inside the initial region. Figure 5.6 show two cases for how the two constraints can play out. Even though the improved scheme was not implemented for this thesis, we assume that the values for $\delta \boldsymbol{P}$ are large enough to avoid destructively narrow intervals.

This scheme of making smaller intervals was done for all the HF ON parameters except Q_{peak}. This is because we expect rapid decreases or increases in the total heating as we pass the double resonance.

5.4.1 Initial conditions

During HF ON periods, steady-state conditions can obviously not be assumed. For each HF ON period we use two different initial conditions, one for the first time step after a HF OFF period, and one for each time step into the pulse. For the first step after a HF OFF period, the last column in the preceding modeled $\tilde{T}^{i-1}_{e,BG}$ is used as the initial condition. This is used because we can assume that we have continuity between each HF OFF period and the following HF ON period. For each following time step into each HF ON pulse, the modeled $\tilde{T}_e$ from the previous time step is used as the initial condition. That is, $\tilde{T}^{i}_{e,HF,j}$ is used as the initial condition for $\tilde{T}^{i}_{e,HF,j+1}$. The modeled temperatures for each period i and step j as well as HF OFF temperatures $\tilde{T}^{i}_{e,BG}$ are show in Figure 5.5.

5.5 Parameter uncertainties

The evaluation of the uncertainty and validity of the model parameters was done in three steps. First, we calculate the covariance matrix for each set of parameters. Next, the variances of each set of parameters were extracted and the correlation between the parameters in each set was calculated. Finally, the relative uncertainty for each parameter in each set of parameters is found based on the parameter itself and its variance. Each set of parameters contain both the HF OFF and HF ON parameters which yield vectors P^i of length 6:

$$\boldsymbol{P}^i = \begin{bmatrix} C_0 & CdT_e & Q_{\text{peak}} & z_{\text{peak}} & \Delta z_D & \Delta z_U \end{bmatrix} \tag{5.18}$$

in which the background parameters C_0 and CdT_e are the means of the parameters found in the HF OFF periods preceding and following HF ON period i.

The covariance matrix for a set of parameters is calculated from the Jacobian matrix of the parameter set and the observed errors in the electron temperatures from the GUISDAP analysis, that is

$$\Sigma = \left(\boldsymbol{J}^T \boldsymbol{e}_{\text{Te}} \boldsymbol{J}\right)^{-1} \tag{5.19}$$

where Σ is the covariance matrix which gives the variance of each parameter on its diagonal, and the covariance between the parameters on the entries off the diagonal. $\boldsymbol{e}_{\text{Te}} = \text{diag}(1/\sigma(Te)^2)$ is the observed uncertainty in the electron

temperatures from the GUISDAP estimates and $\boldsymbol{J}$ is the Jacobian matrix for the current set of parameters which is

$$\boldsymbol{J_j^i} = \frac{\partial \tilde{T}_{e,HF}(z)}{\partial \boldsymbol{P}^i_j} = \begin{bmatrix} \frac{\partial \tilde{T}^i_{e,HF,j}(z_{\text{top}})}{\partial \boldsymbol{P^i_{j,1}}} & \cdots & \frac{\partial \tilde{T}^i_{e,HF,j}(z_{\text{top}})}{\partial \boldsymbol{P^i_{j,6}}} \\ \vdots & \ddots & \vdots \\ \frac{\partial \tilde{T}^i_{e,HF,j}(z_{\text{bottom}})}{\partial \boldsymbol{P^i_{j,1}}} & \cdots & \frac{\partial \tilde{T}^i_{e,HF,j}(z_{\text{bottom}})}{\partial \boldsymbol{P^i_{j,6}}} \end{bmatrix} \tag{5.20}$$

where $\frac{\partial \tilde{T}_{e,HF}(z)}{\partial \boldsymbol{P}^i_j}$ is the variation with each parameter. The variation is calculated by finding the difference between the modeled temperatures with the optimal parameter set and a model with a set of parameters where the optimal parameters are shifted by one percent in random directions.

The correlation matrix is found from the covariance matrix and is defined as

$$\boldsymbol{Corr}(\boldsymbol{P}^i) = \text{diag}(\Sigma^{\boldsymbol{i}})^{-\frac{1}{2}}\, \Sigma^i\, \text{diag}(\Sigma^{\boldsymbol{i}})^{-\frac{1}{2}} \tag{5.21}$$

The correlation matrix contains information on how the different parameters correlate. Its entries are all on the interval $[-1, 1]$ where 1 means perfect correlation and -1 means perfect negative correlation. Negative correlation means that one parameter increases when another parameter decreases.

The relative uncertainty of each parameter is found by scaling the standard deviation of each parameter by the parameter itself, that is

$$e^{\boldsymbol{i}}_{\text{rel,j}} = \frac{\sqrt{\text{var}(\boldsymbol{P}^{\text{i}}_{\text{j}})}}{|\boldsymbol{P}^{\boldsymbol{i}}_{\boldsymbol{j}}|} \tag{5.22}$$

where the standard deviation $\sqrt{\text{var}(\boldsymbol{P}^{\text{i}}_{\text{j}})}$ is found from the diagonal of the covariance matrix for the current parameter set.

6

Results and discussion

Results from the modeling and analysis following the methods described in chapter 5 are presented in this chapter. First modeled background temperatures and background heat sources are presented. Next, modeled temperature enhancements and HF heat sources are presented. Following that, uncertainty estimates for the parameters are presented including correlation matrices, relative uncertainties, a discussion of the heat source shapes and a discussion of possible overfitting. Finally, results of the analysis of the frequency dependence when sweeping the frequency up and down are presented.

6.1 Background models

Figures 6.1, 6.3 and 6.5 show modeled background electron temperatures for the experiments done on the 8^{th}, 14^{th} and 15^{th} of October, respectively. The inserted axes in the three figures show zooms of selected HF OFF periods. In general, the modeled background temperatures are a good match for the observed background temperatures.

We note that temperatures at the top boundary are varying with a few hundred Kelvin. This can be explained by a combination of (1) variable modeled background heating between the periods and (2) the upper boundary condition scaling factor CdT_e. For most HF OFF periods, CdT_e was found to be on the interval $[0.8, 1.2]$. However, significantly larger values were found toward

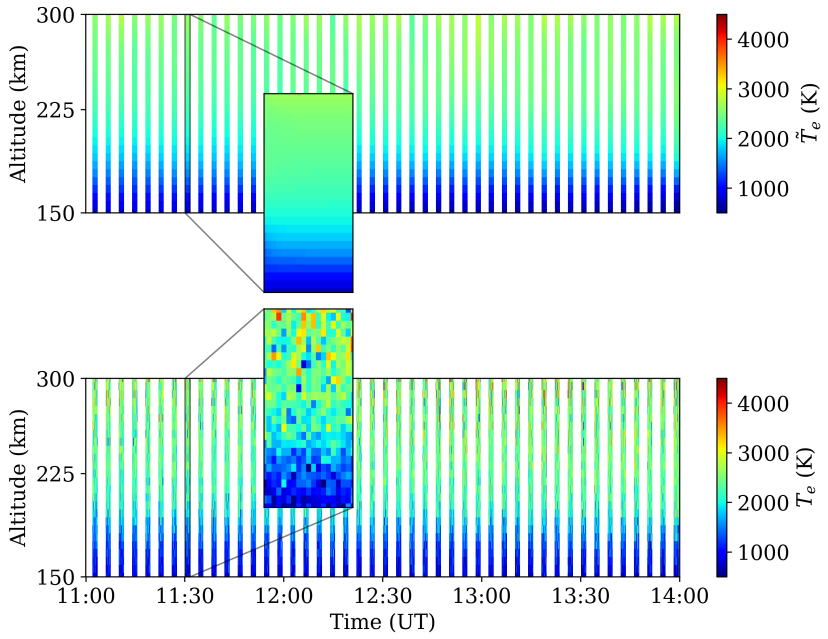

Figure 6.1: Modeled temperature $\tilde{T}_e$ (top) and observed T_e (bottom) panel for the 8th of October 2021. The inserted axes show closer views of HF OFF period 8.

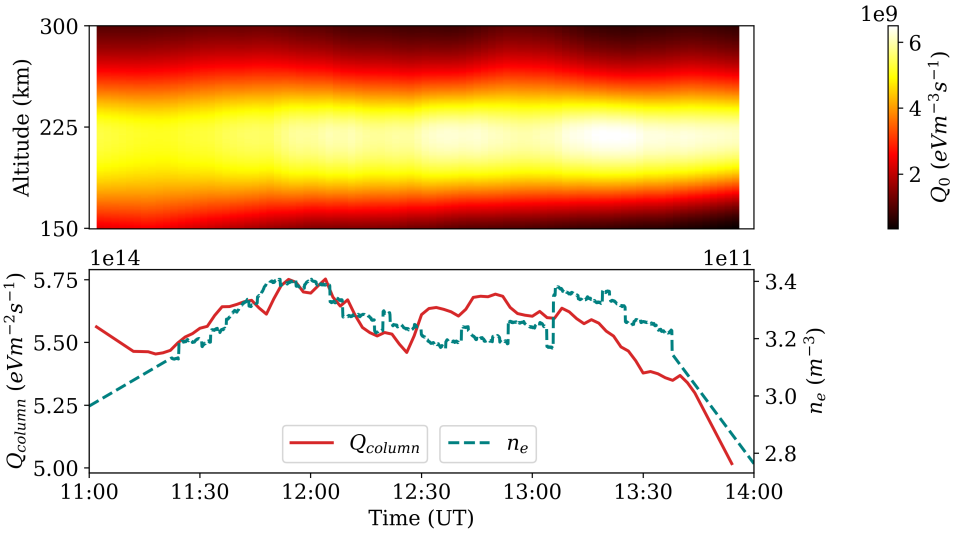

Figure 6.2: Background heat source Q_0 (top panel) and column integrated heat source Q_{column} for the 8th of October 2021.

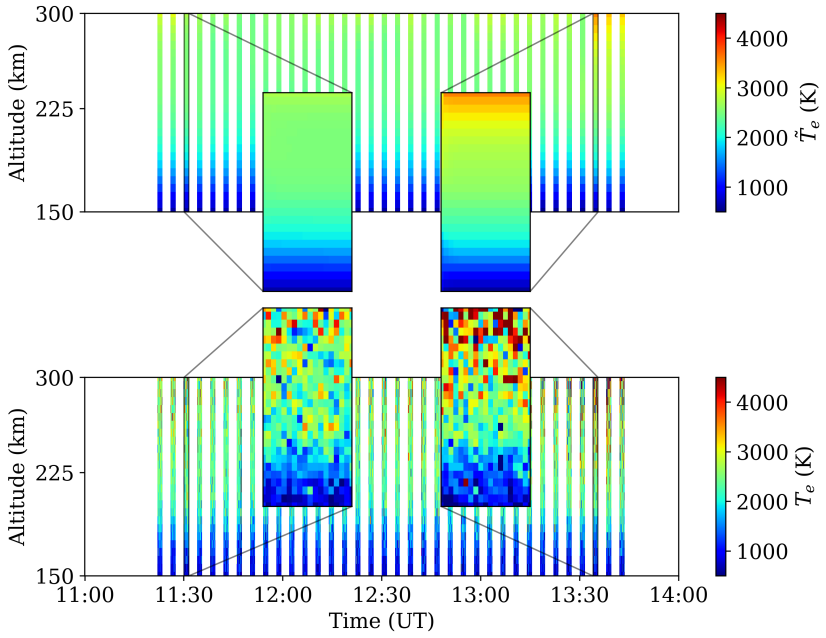

Figure 6.3: Modeled temperature $\tilde{T}_e$ (top) and observed T_e (bottom) panel for the 14$^{\text{th}}$ of October 2021. The inserted axes show closer views of HF OFF period 8 (left) and HF OFF period 39 (right).

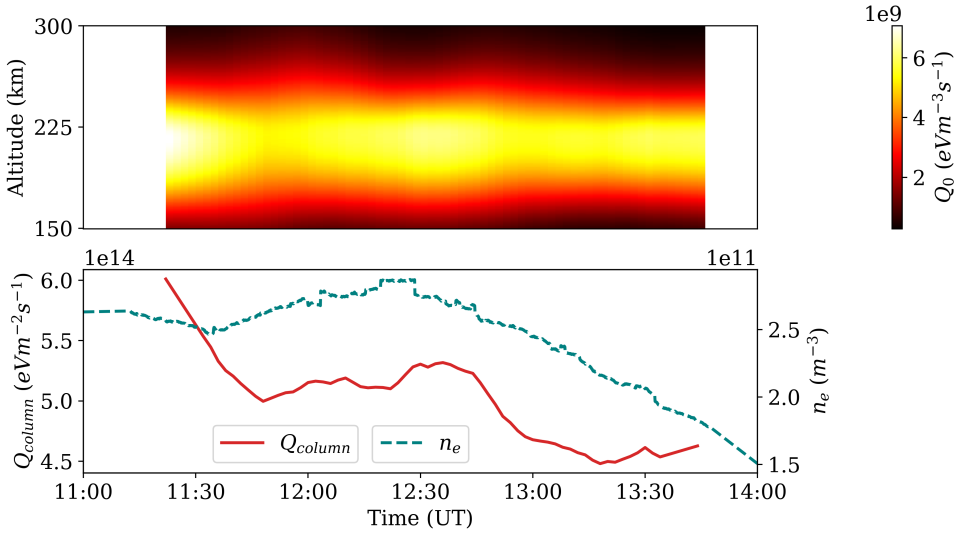

Figure 6.4: Background heat source Q_0 (top panel) and column integrated heat source Q_{column} for the 14$^{\text{th}}$ of October 2021.

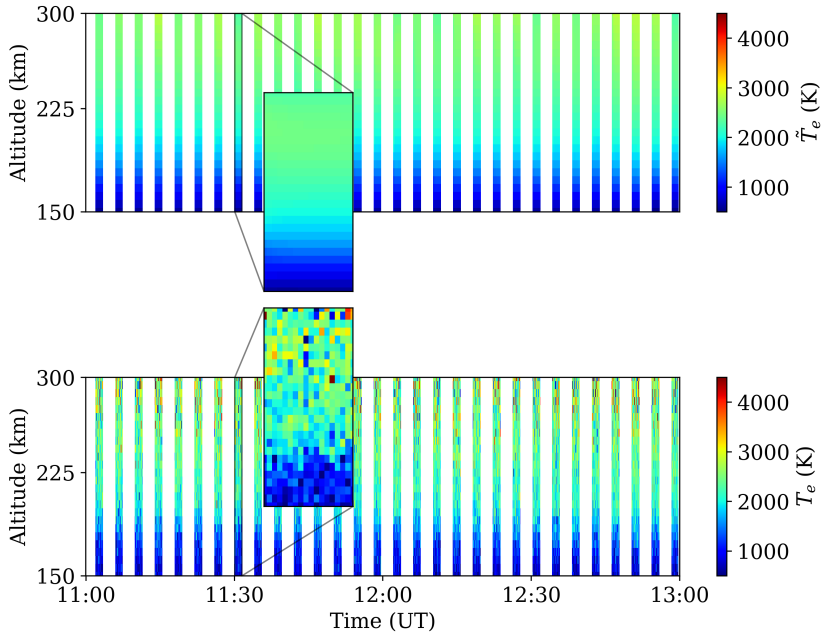

Figure 6.5: Modeled temperature $\tilde{T}_e$ (top) and observed T_e (bottom) panel for the 15th of October 2021. The inserted axes show closer views of HF OFF period 8.

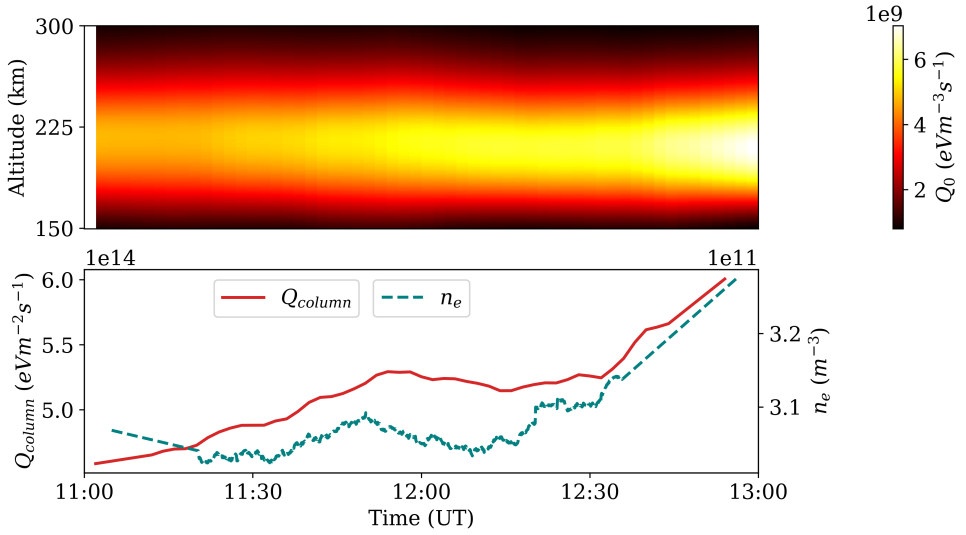

Figure 6.6: Background heat source Q_0 (top panel) and column integrated heat source Q_{column} for the 15th of October 2021.

the end of the experiment done on the 14th of October 2021. As explained in section 4.1 the electron density decreased rapidly yielding "high temperature" noise at high altitude. It is possible that the large CdT_e values in the last three HF OFF periods are fitted to this noise. However, we cannot rule out that the higher temperatures are plausible, due to thermal contact with high energy electrons in the inner magnetosphere. Nonetheless, it is likely that the higher temperatures are mostly due to noise.

Figures 6.2, 6.4 and 6.6 show fitted background heating rates for the experiments done on the 8th, 14th and 15th of October, respectively. The top panel in each figure shows the heating rate as a function of time and altitude and the bottom panel show the column integrated heating rate as a function of time as well as the observed electron densities at approximately 220 km, where the heating rates peak. Both panels are slightly smoothed to make it easier to see the general shapes of the heating rates and their evolution with time.

For the 8th of October we see that the heating rate is narrowing with time and that the peak heating rate is increasing. This can be explained by a decrease in heat conduction which means that the heat will be more narrowly distributed around the peak altitude. However, the column integrated heating rate is decreasing with time which is expected due to the experiment duration from 11:00 UT to 14:00 UT which corresponds to 13:00 to 16:00 local time and because the electron density decreases. From equation 2.13 it is clear that if Q_{HF} is zero, an increase in electron density n_e will result in an increase in the background heating Q_0.

As expected, the column integrated heating rate is also decreasing with time for the experiment done on the 14th of October. For this experiment the background heating rate is narrowing with time as well as the peak heating rate is decreasing. Contrary to the 8th and the 14th, the heating rate for the 15th of October increases in width with time and the peak heating rate increases. The column integrated heating rate also increases slightly over the course of the experiment. This is because the electron density is increasing.

6.2 HF ON models

The results of the modeling of HF ON heat sources are presented in this section. First, models of heat sources and temperatures far away from the double resonance frequency is presented. Second, modeled heat sources and temperatures where we pass the double resonance is presented.

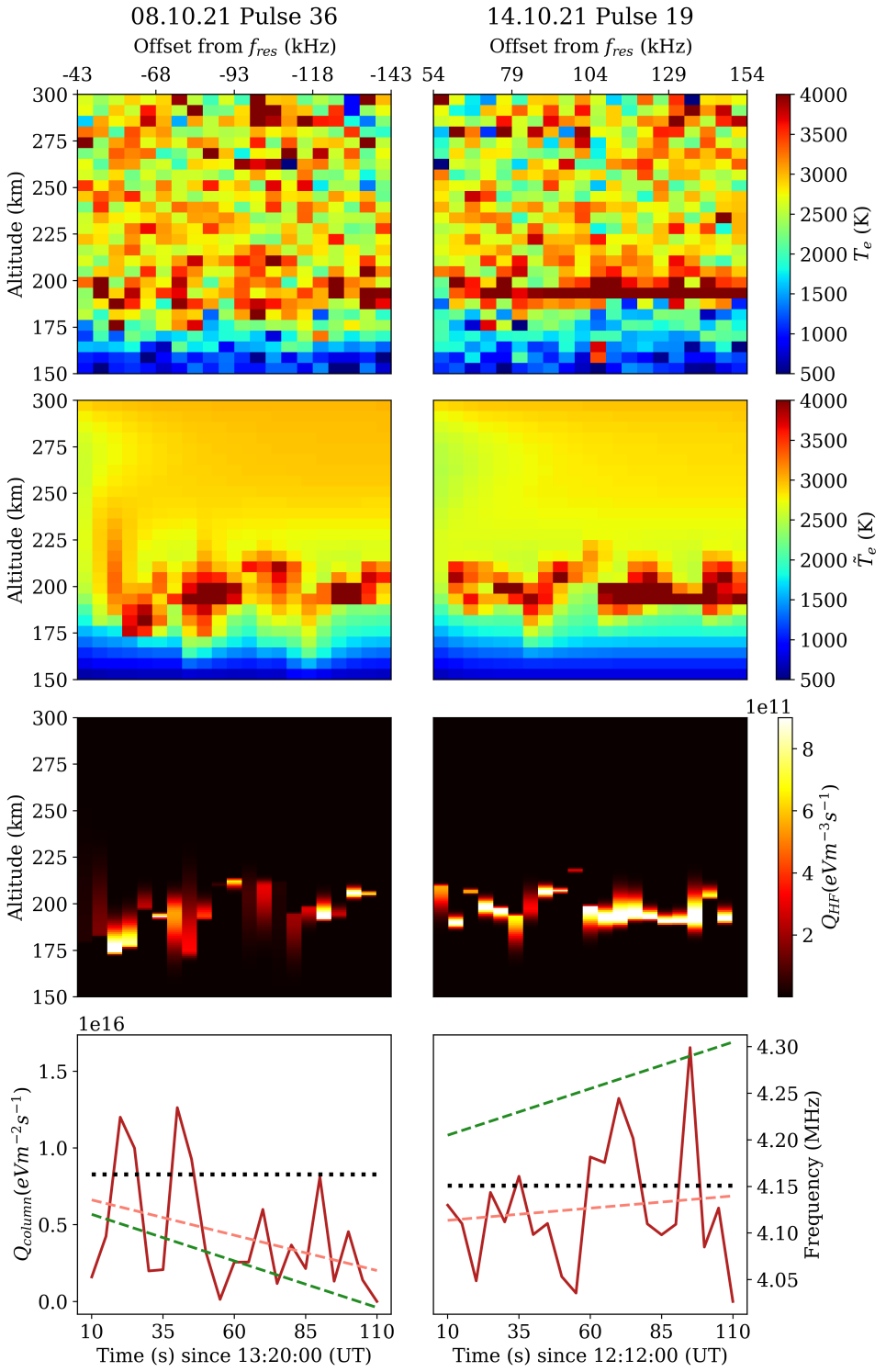

Figure 6.7: Observed temperatures (top row), modeled temperatures (second row), modeled HF heat sources (third row) and modeled column integrated heating rates as well as a linear fit of the column integrated heating rates (bottom row) for pulse no. 36 on the 8th of October 2021 (left column) and pulse no. 19 on the 14th of October 2021. The dotted black line shows the third double resonance frequency while the green dashed line shows the HF pump frequency.

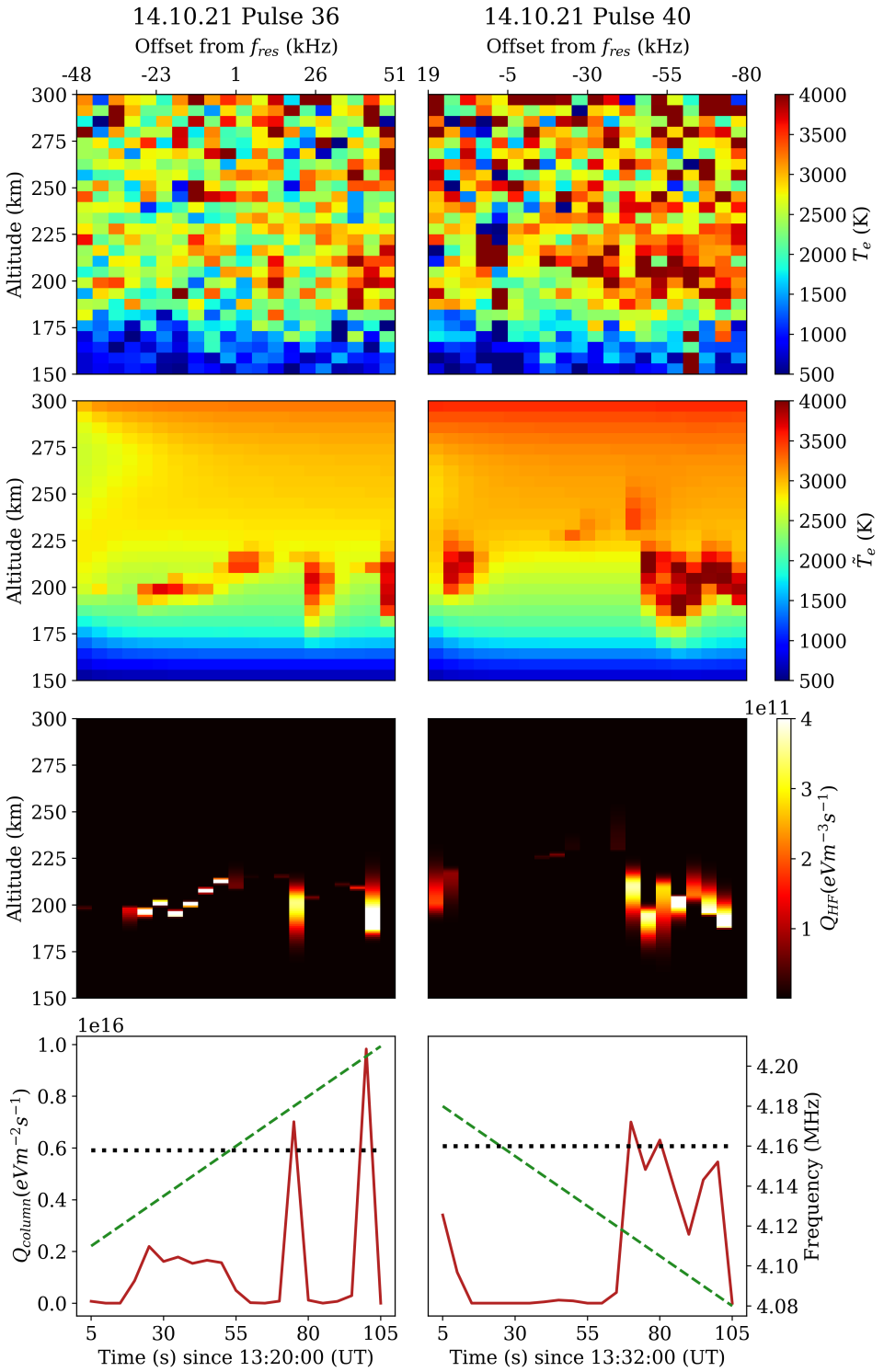

Figure 6.8: Observed temperatures (top row), modeled temperatures (second row), modeled HF heat sources (third row) and modeled column integrated heating rates (bottom row) for pulse no. 18 and pulse no. 40 on the 29th of October 2021. The dotted black line shows the third double resonance frequency while the green dashed line shows the HF pump frequency.

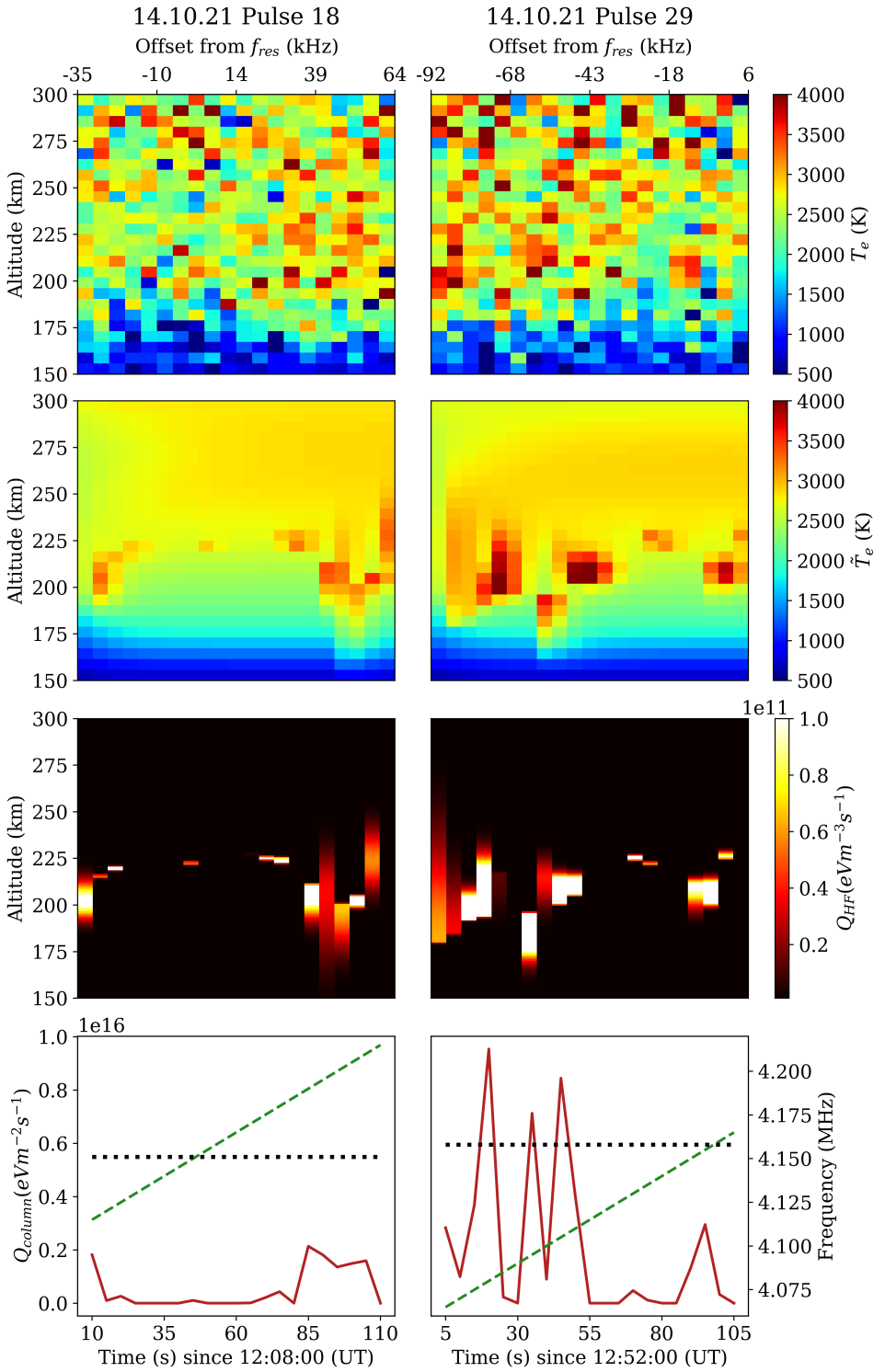

Figure 6.9: Observed temperatures (top row), modeled temperatures (second row), modeled HF heat sources (third row) and modeled column integrated heating rates (bottom row) for pulse no. 36 and pulse no. 40 on the 14th of October 2021. The dotted black line shows the third double resonance frequency while the green dashed line shows the HF pump frequency.

6.2.1 Heating away from the double resonance

Figure 6.7 shows T_e, $\tilde{T}_e$, Q_{HF} and column integrated heating rates where the HF pump frequency does not pass the third double resonance. The two pulses shown are the pulses starting at 13:20:00 UT on the 8$^{\mathrm{th}}$ of October 2021, where the pump frequency is decreasing and 12:12:00 UT on the 14$^{\mathrm{th}}$ of October 2021, where the pump frequency is increasing.

In both pulses we see clear enhancements of the model temperatures above the background electron temperatures throughout. We also have a clear heating rate through the entire pulse. This matches well what we would expect away from a double resonance frequency as we have no suppression of UH and EB phenomena (see section 2.3.5) which therefore gives heating throughout the pulse.

Linear fits to the column integrated heating rates for both pulses are shown with the column integrated heating rates in the bottom panel of Figure 6.7. Although the variances of the column integrated heating rates are high, the linear fits might indicate that when the frequency is increased/decreased the heating rates increase/decrease. This would be expected, as the ERP of the transmitted pump wave increases with pump frequency.

In general, the modeled temperatures are not perfect reproductions of the observed temperatures. However, the fact that we see the same even trend of the temperature enhancements in both the modeled temperatures and in the observed temperatures indicate that the method has performed sufficiently well, and we can assume that the parameter fitting scheme and integration scheme for finding the model temperatures will also work sufficiently well for pulses where the HF pump frequency passes the double resonance frequency.

6.2.2 Heating around the double resonance

Figure 6.8 shows T_e, $\tilde{T}_e$, Q_{HF} and column integrated heating rates where the pump frequency passes the double resonance. The two pulses shown are the pulses starting at 13:20:00 UT, where the pump frequency is increasing and 12:12:00 UT, where the pump frequency is decreasing. Both pulses are from the experiment done on the 14$^{\mathrm{th}}$ of October 2021. In both pulses we clearly see that we have minima in the heating rates around the double resonance frequency. The offset from the pump frequency is shown at the top of each column in Figure 6.8. For pulse no. 40 (right column), we can clearly see that the width of the minima around the double resonance is approximately 60 kHz. This is a good match with the width found by Gustavsson et al. [16].

In both modeled pulses shown in Figure 6.8 we note that the temperatures at the top boundary are significantly higher than the modeled temperatures shown in Figure 6.7. We also note that the top boundary temperatures are higher for pulse 40 than for pulse 36. A possible explanation for the higher modeled temperatures is that the pulses in 6.8 are based on temperatures from the last part of the experiment done on the 14th of October 2021. As discussed in section 4.1, we observed plasma inflow from the night-side toward the end of this experiment. This resulted in a rapidly decreasing electron density which in turn gave "high temperature" noise at decreasing altitudes. To alleviate this, the altitude range of the PDE solution was cropped, but clearly the maximum altitude would need be lower to completely crop out the noisy high-altitude temperatures. The inclusion of this "high temperature" noise have likely affected the parameter optimization. It is possible that the fitted boundary condition scale factors are too high because of the included noise at high altitudes. This is also visible in Figure 6.3.

Figure 6.9 shows two pulses starting at 12:08:00 UT and 12:52:00 UT on the 14th of October 2021. In these two pulses the HF pump frequency pass the third double resonance from below. In both modeled heat sources, we see minima around the third double resonance. The minimum in pulse no. 18 is especially clear when we look at the column integrated heating rate. The minimum has an approximate width of 65 kHz which is close to the width of the interval in pulse no. 40 shown in Figure 6.8.

In all 6 presented pulses we note that the heat sources are highly variable, both in terms of the peak altitude and the half-widths. The peak altitudes in the second part of pulse 40 on the 14th of October 2021 are shifting with up to 20 km between each five second step in time. However, the noise levels in the corresponding observed temperatures are high, and it is not clear which altitude the enhancements in temperature peak. This has possibly resulted in the parameter fitting scheme fitting z_{peak} to noise. The parameter fitting scheme is especially sensitive to noise because only one column in the observed temperatures, which corresponds to one five second step in time, is considered in each error minimization. A single point that clearly is noise when looking at the entire pulse at the same time can appear as a high temperature at that altitude in the column and therefore influence the parameter fitting. Compared to pule 19 on the 14th of October 2021 we see that the peak altitude is more stable with time where the enhancements in the observed temperature are more easily distinguishable from the noise in the second half of the pulse.

We see the same trend in the half-widths where the noise level is high relative to the observed enhancements. This is clearly visible throughout pulse 36 on the 8th of October 2021. We note a wide array of heat source shapes; seemingly one-sided and symmetric, both narrow and wide in altitude. One the other

hand, the half-widths are more predictable with time in the second half of pulse 19 from the 14th of October 2021, where again the enhancements are more easily distinguishable from the noise. The high variability of both the peak altitudes and the half-widths is a symptom of the high noise which has likely led to overfitting [38]. Overfitting means that the fitted parameters are influenced by noise in the data. This obstacle is revisited in section 6.3.4 where possible methods to avoid overfitting the heat HF source parameters are discussed.

Further, the challenge of accurately fitting the HF parameters grows as small variations in $Q_{\mathrm{HF}}(z)$ are lost when integrating the ionospheric parameters to an altitude resolution of 6 km. A reason for the narrow enhancements can be the fact that the peak enhancement altitude is low. In figure 4.1 we see that our temperature enhancements peak at around 190 km. Higher peak altitudes of well above 210 km were observed by [15, 17, 22]. Lower peak altitudes lead to higher cooling rates (see Figure 2.8). Higher cooling rates lead to the enhancements disappearing faster, which also makes it more challenging to fit the parameters. In addition, HFIL causes information around the reflection altitude to be lost. Because the temperature enhancements are narrow in altitude, it would possibly be better to use range gates with size 3 km, like done by Gustavsson et al. [16], to get better information on the altitude variation of our heat sources. However, because our maximum integration time for the experiments detailed in this thesis is five seconds, larger range gates were necessary to reduce measurement noise.

6.3 Parameter uncertainties

In this section estimates for parameter uncertainties calculated as explained in section 5.5 are presented. First, a selection of correlation matrices is presented. Next, relative uncertainties in a selection of parameter sets are presented, as well as their distributions. Lastly the heat source shapes and possible overfitting is discussed.

6.3.1 Correlation matrices

Figure 6.10 show a selection of 8 correlation matrices that together illustrate the variable correlations observed in the correlation analysis. Even though the correlations between the parameters vary with pulse number and time step, we note some possible trends. First, the background scaling parameters C_0 and CdT_e generally anti-correlate, although weakly in some cases. This is expected as an increase in C_0 leads to an increase in $\tilde{T}_e$ at all altitudes, although

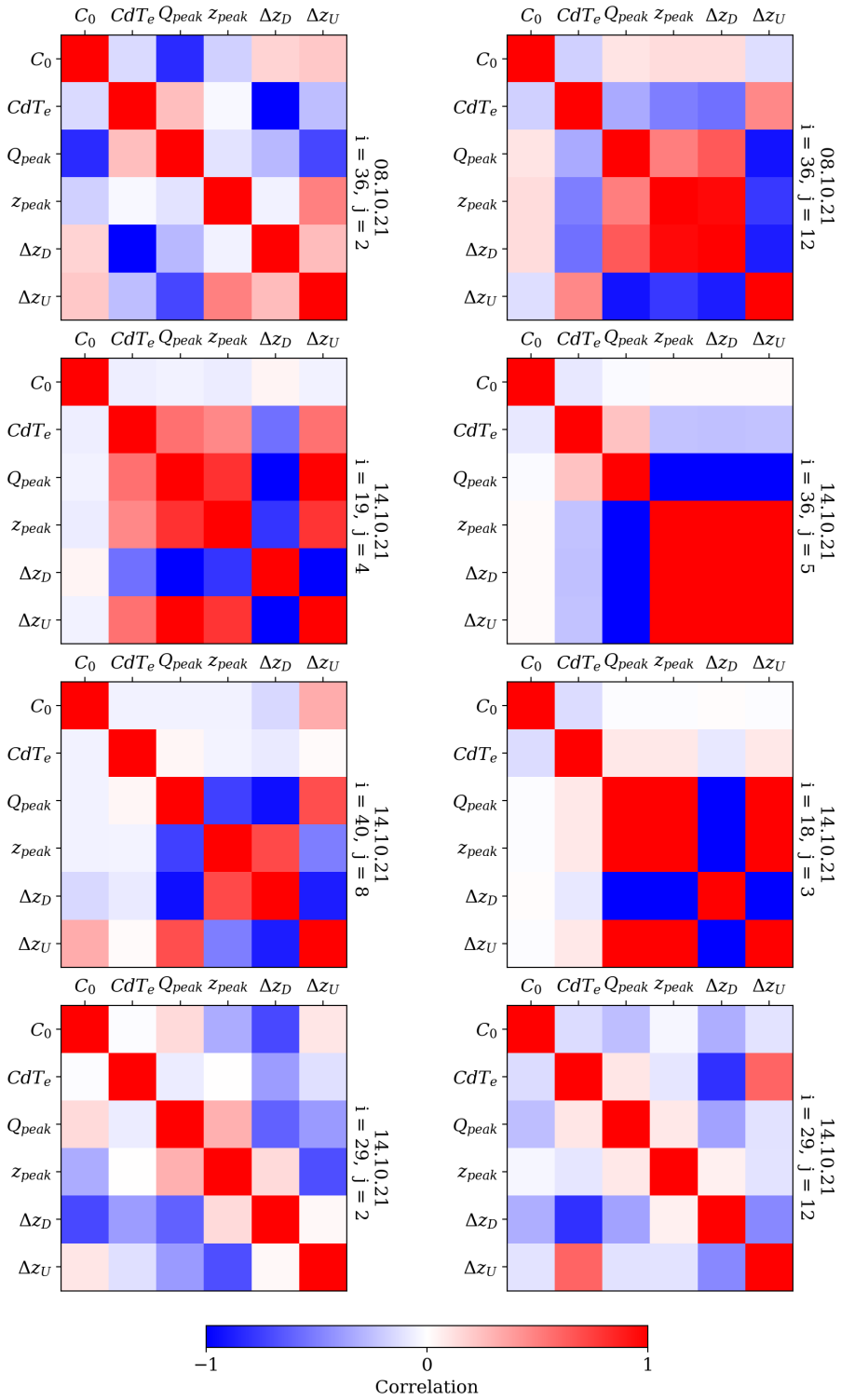

Figure 6.10: A selection of correlation matrices. The corresponding dates, pulse numbers i and time steps j is shown on the right side of each matrix.

mainly around 225 km where the Chapman shaped Q_0 peaks. If there is have a slight increase in $\tilde{T}_e$ at the top boundary, CdT_e must decrease to explain the same temperature at the top boundary. We also note that the scaling parameter C_0 in most cases anti-correlate with most of the HF ON parameters. This is also expected. If the background heat source is scaled up, a lower total HF heat source is needed to explain the enhanced temperatures.

Further, in 6 of the selected covariance matrices, Δz_D and Δz_U anti-correlate. This is expected. When the size of either Δz_D or Δz_U increase, a decrease in the size of the opposite parameter will conserve the total width of the heat source. However, the two remaining matrices show that Δz_D and Δz_U and in one case *perfectly*. This is curious as it contradicts our expectation. Another explainable correlation that we see in some matrices, e.g. the left matrix in the top row in Figure 6.10, is that z_{peak} correlate with Δz_U and anti-correlate with Δz_D. This is reasonable because if z_{peak} increases, Δz_U must decrease and Δz_D must increase to preserve the width of the heat source. However, we do not see this correlation in all our parameter sets.

The correlations not discussed thus far are show no apparent trends. The highly variable correlations in the parameter sets might indicate that the parameters are characterized by some degree of randomness.

6.3.2 Relative uncertainties

Next, the relative uncertainties for each parameter are considered. Figure 6.11 show the relative uncertainties for 3 sets of parameters. The date, pulse number and time step are shown on the right side of each plot. It is clear that we have some trends in the relative uncertainties.

Above all the relative uncertainties for C_0, CdT_e and z_{peak} are exceptionally low. This is definitely an indication that the three parameters are well fitted to the data. For C_0 and CdT_e we must remember that ion densities from the MSIS model are used when calculating the electron loss rates, and we therefore assume that the atmospheric ion densities during out experiments are well explained by the retrieved model. However, if uncertainty in the model was included in the analysis, we would expect the uncertainties in C_0 and CdT_e to be larger. In Figures 6.7, 6.9 and 6.8 it is visible that the enhancements in temperature are narrow in altitude. This means that it is relatively uncomplicated to accurately place z_{peak} in the correct 6 km range gate during the parameter search. This explains why the relative uncertainties in z_{peak} are low compared to the other HF parameters.

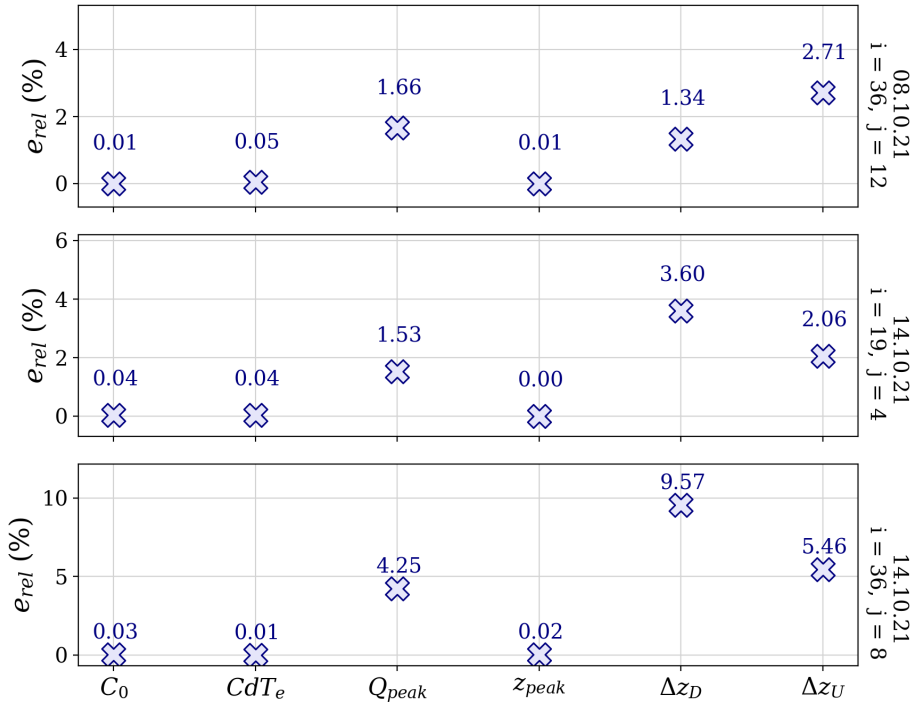

Figure 6.11: A selection of relative uncertainties e_{rel}. The corresponding dates, pulse numbers i and time steps j is shown on the right side of each plot.

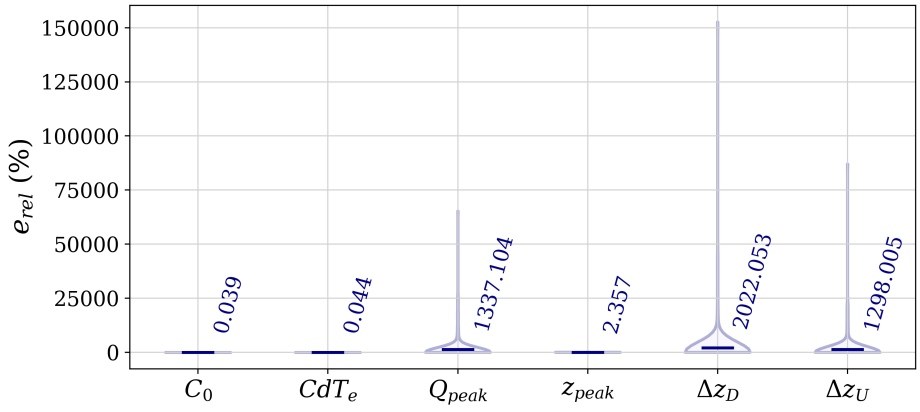

Figure 6.12: Distributions of relative uncertainty per parameter. The blue text shows the mean relative uncertainties.

Figure 6.12 shows the distributions of relative uncertainties for all the parameter sets. First and foremost, it is clear that half of the means are extremely high, with

a maximum mean of 2022% for Δz_D. However, we see that the distributions are extremely narrow for increasing relative uncertainties. This indicate that some outliers have influenced the distributions. The distributions will be revisited later in this chapter.

6.3.3 HF heat source shape

The distributions of relative uncertainties of the half-widths Δz_D and Δz_U presented in section 6.3.2 are clearly heavily influenced by outliers. Because of this, Δz_D and Δz_U, and the general shapes of the heat sources Q_{HF} will be further investigated in this section. A scatterplot of all (Δz_U,Δz_D) pairs in the parameter sets is shown in the left panel in Figure 6.13. Normal distributions calculated from estimated means and standard deviations from the (Δz_U,Δz_D)-distribution overlaying histograms of the (Δz_U,Δz_D) values are shown in the right panel, where it is clear that the spread in the (Δz_U,Δz_D)-distribution cannot be neatly described by the two estimated normal distributions. However, we note that the distribution for Δz_D is slightly narrower than the distribution for Δz_U with a higher count of low values. The distribution for Δz_U have also a higher count of large values up to 50 km.

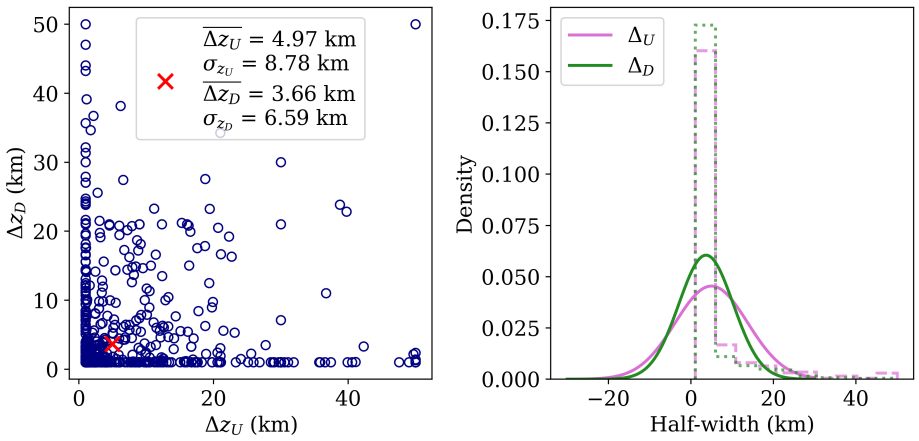

Figure 6.13: The left panel show the distribution of half-widths Δz_U and Δz_D. The red cross shows the mean pair of half-widths. The legend shows the mean values and the estimated standard deviation. The right panel show histograms of the two half-widths and normal distributions with the estimated means and standard deviations from the distribution in the left panel.

Further, from the distribution in the left panel in figure 6.13, it is clear that the majority of the half-widths are small, i.e. less than 10 km. This is expected

from the narrow observed T_e enhancements. However, we also see a large number of half-widths up towards 50 km. Interestingly, the bulk of these larger half-widths are paired with a smaller half-width. This means that there are several heat sources Q_{peak} in the estimates that are extremely skewed, both upwards and downwards in altitude. To find the conditions under which these very large half-widths occur, the relation between the peak heating rate Q_{peak} and the half-widths was investigated. A scatterplot of Q_{peak} against Δz_D and Δz_U is shown in Figure 6.14.

Two interesting trends can be seen in Figure 6.14. First an foremost, we note that *all* the maximum half-widths at around and at 50 km coincide with $Q_{\text{peak}} \approx 0$. When this is the case the remaining HF heat source parameters do not matter: the total heat source ≈ 0. This can, and have seemingly, resulted in arbitrary heat source shapes where $Q_{\text{peak}} \approx 0$. It is also highly likely that this arbitrary selection of half-widths when $Q_{\text{peak}} \approx 0$ also has resulted in smaller half-widths. This means that it is safe to assume that the HF parameters where $Q_{peak} \approx 0$ are arbitrary to some degree.

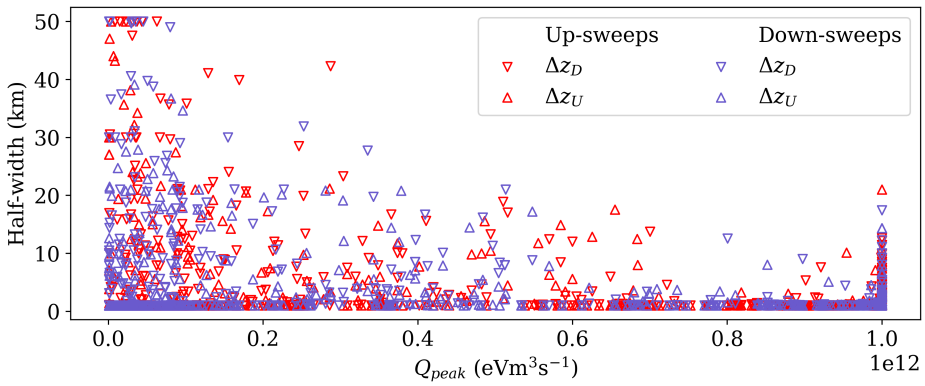

Figure 6.14: Half-widths Δz_D (upside-down triangles) and Δz_U (triangles) for up-sweeps (red) and down-sweeps (purple) plotted against Q_{peak}.

The second interesting trend is that there also is an increase in half-width size where $Q_{peak} = \max(Q_{\text{peak}})$. It is of interest to determine where these heat sources occur. This was done by checking for parameter sets where either $\Delta z_D > 13$ km or $\Delta z_U > 13$ km while $Q_{\text{peak}} > 9.5 \times 10^{11}$ eVm^{-3}s^{-1}. Two examples of pulses in which this condition is met for a parameter set are shown in Figure 6.15. The left panel shows pulse no. 38 and the right panel show pulse no. 41, both from the 8$^{\text{th}}$ of October 2021. The heat sources that meet the aforementioned condition is the heat source at approximately 90 seconds in the left panel and the heat source at approximately 10 seconds in the right

panel.

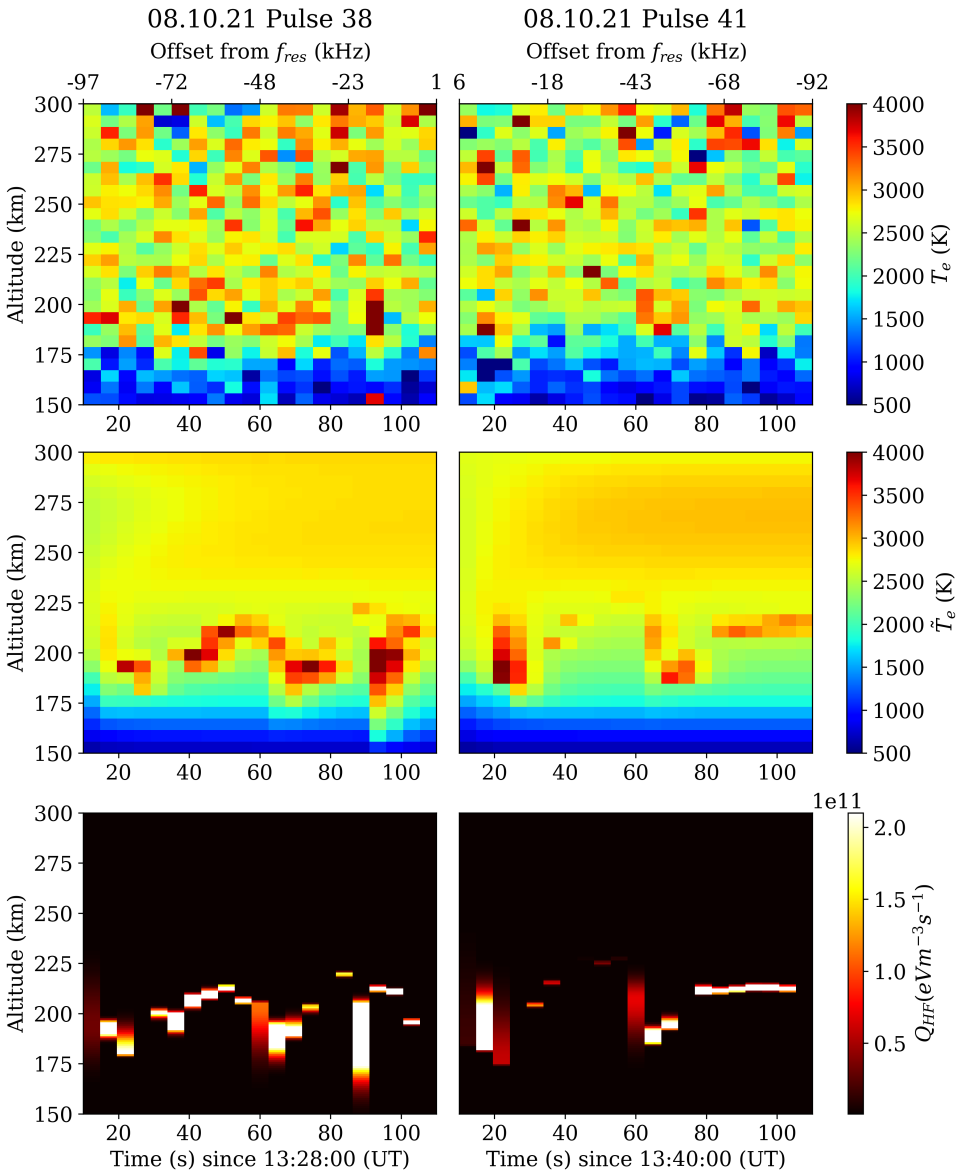

Figure 6.15: Observed temperatures (top row), modeled temperatures (second row) and modeled HF heat sources (third row) for pulse no. 38 (right) and pulse no. 41 (left) on the 29th of October 2021.

First and foremost, both heat sources occur within 20 kHz of the double resonance frequency. It is therefore reasonable to assume that these heat sources are not accurate. Second, we see that the heat sources correspond to what appears to be noise in the observed temperatures, especially since we do not

expect large temperature enhancements close to the double resonance. The parameter fitting has clearly been misguided by the high temperature noise. This has resulted in inaccurate heat sources and therefore inaccurate modeled temperatures. The fact that we get heat sources fitted to the noise, especially the single point in the right panel in Figure 6.15, can be a consequence of using $\sqrt{\sigma}$ in the minimization instead of σ^2. As explained previously, using the root of σ is necessary to avoid out-weighting the HF enhanced temperatures. However, a by-product of this is that noise is not as well out-weighted. This is clear when looking at the observed temperatures and the fitted heat sources. Again, this indicates that another likelihood function could be considered for the optimization, especially in the case of noisy data.

From the observations that the maximum half-widths are paired with $Q_{\text{peak}} \approx 0$ and the indication that a number of the largest half-widths paired with $Q_{\text{peak}} = \max(Q_{\text{peak}})$ is fitted to noise indicate what we can clearly see in the observed temperatures: the electron temperature enhancements are narrow in altitude which also means that the HF heat sources are narrow in altitude. However, it is necessary to take a closer look at the heat source shapes, namely the fact that we have a large number of strongly skewed heat sources that switch directions from one step in time to the next. This can be seen in the left panel in Figure 6.7.

To evaluate the heat source shapes it is convenient to look at the total width w_{HF} around the center altitude, center-of-heating (COH), z_{coh} of the heat source Q_{HF} instead. z_{coh} is calculated as the expectation value of $Q_{\text{HF}}(z)$, that is

$$z_{\text{COH}} = \frac{\int z \cdot Q_{\text{HF}}(z)dz}{\int Q_{\text{HF}}(z)dz} \tag{6.1}$$

while w_{HF} is calculated as the variance of $Q_{\text{HF}}(z)$ around z_{coh}, that is

$$z_{\text{COH}} = \frac{\int (z - z_{\text{coh}})^2 Q_{\text{HF}}(z)dz}{\int Q_{\text{HF}}(z)dz} \tag{6.2}$$

The distribution of total width w_{HF} is shown in Figure 6.23. The size of the histogram bins is 6 km. This is because the altitude resolution in the GUISDAP estimates is 6 km, which means that we cannot accurately distinguish between widths inside intervals of size 6 km. It is clear in Figure 6.23 that the distribution of the total widths is as expected. We see that the bulk of the widths are on the interval from 0 to 6 km, which matches the narrow observed temperature enhancements. We also note that we have only an extremely low count of

outlying widths, that is widths up toward 50 km like were observed in Figure 6.13. Above the interval 18-24 km we only have a minimal count of widths on the interval 30-36 km. This agrees with the (Δz_U,Δz_D)-pairs shown in Figure 6.13. The majority of the larger half-widths are paired with a smaller half-widths, resulting in lower total widths.

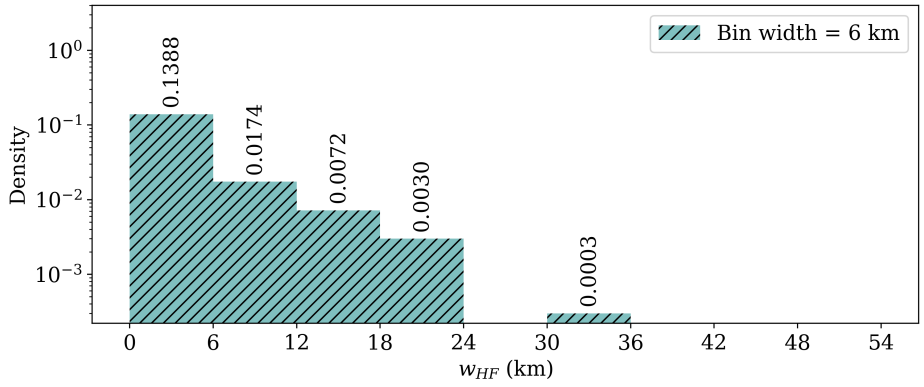

Figure 6.16: Histograms of total heat source width w_{HF} around z_{coh}. Note that the density is on a logarithmic scale.

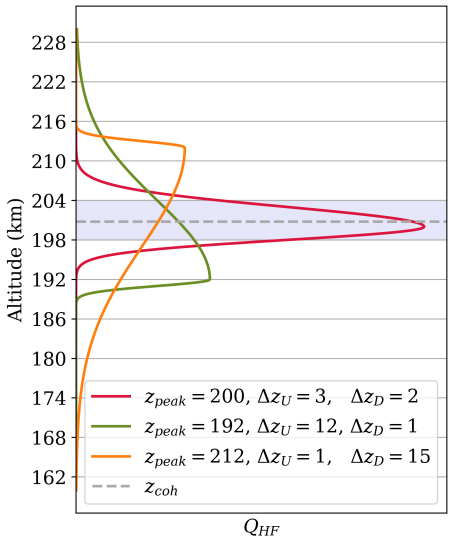

Figure 6.17: Three example heat sources with different z_{peak} and half-widths but with coincident z_{coh} (shown in gray).

The observation that the outlying half-widths are paired with lower half-widths and vanish when considering the total width can be explained by analyzing

the previously mentioned steep gradients in the heat sources. Such steep heat sources can be seen in the right column in Figure 6.7. Three example heat source shapes are shown in Figure 6.17. The three heat sources have different z_{peak} and their half-widths cover two extremes; the orange and green heat sources represent heat sources with a pair of one large and one small half-width. The gray dashed line shows the COH shared by all three heat sources. Therefore, the COH of all three heat sources are covered by the same 6 km range in altitude (shaded with purple). This means that all three heat sources will have their peak heating inside the same 6 km range interval. This can explain the highly variable half-widths; the shapes of the heat sources vary greatly but overall, their COH can fall inside the same 6 km range. This effect is visible in the second quarter of the pulse in the left column in Figure 6.7, where we see that differently skewed heat sources yield similar temperatures.

Relative uncertainties revisited

The information about where the fitted parameters are possibly arbitrary means that we can revisit the relative uncertainties. Figure 6.18 shows the distributions of the relative uncertainties per parameter, under the conditions that $\Delta z_D < 40$ km, $\Delta z_D < 40$ km and $Q_{\text{peak}} > 10^{11}$ eVm^{-3}s^{-1}. These conditions are applied because it is clear that when $Q_{\text{peak}} \approx 0$ part of fitted parameters can be arbitrary.

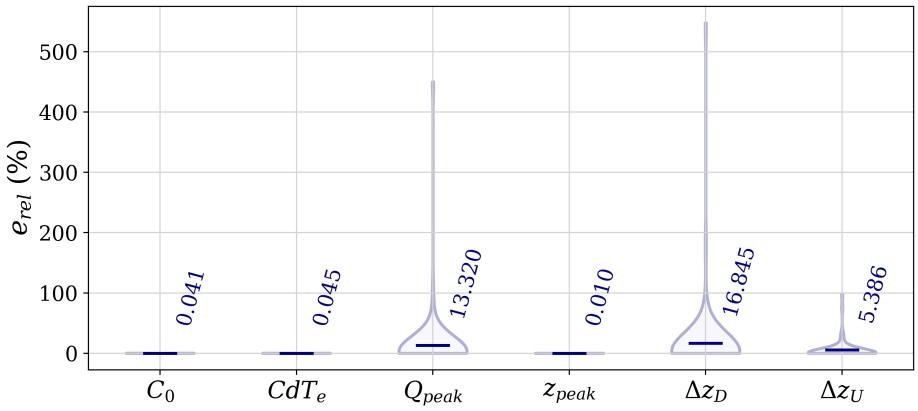

Figure 6.18: Distributions of relative uncertainties per parameter under the conditions that $\Delta z_D < 40$ km, $\Delta z_D < 40$ km and $Q_{\text{peak}} > 10^{11}$ eVm^{-3}s^{-1}.

The distributions shown Figure 6.18 are clearly different for the distributions shown in Figure 6.12. Most notable is the fact that the means of each HF parameter uncertainty distributions are significantly lower. It is therefore safe

to assume that the high means and skewed shapes of the distributions in Figure 6.12 are caused by the erroneous parameters when $Q_{\text{peak}} < 10^{11}$ eVm^{-3}s^{-1}. Therefore, we can also assume that the constrained distributions are better representatives for the actual uncertainties in the non-arbitrary parameters. The new distribution means are 13.3% for Q_{peak}, 16.9% for Δz_D and 5.39% for Δz_U. Though we still have some outlying points in the distributions for Q_{peak} and Δz_D, the means indicate that the parameters are well fitted to the data. However, it is important to reiterate that the parameters might be overfitted.

6.3.4 Parameter space size and overfitting

As mentioned previously, it is possible that the fitted parameters are *overfitted*. This means that the parameters are well fitted to the data and therefore also to the measurement noise. This means that the fitted HF heat sources does not *necessarily* describe the HF heating in the experiment, because the parameters are influenced by noise.

Overfitting can occur when the parameter space is too large [38]. This means that to lessen the risk of overfitting the chosen parameter space could be smaller. A suggestion to reduce the size of the parameter space is to replace the two-sided Gaussian $Q_{\text{HF}}(z)$ by a symmetric Gaussian with half-width Δz, i.e.

$$Q_{\text{HF, symmetric}}(z) = Q_{\text{peak}} \exp\left[-\left(\frac{z - z_{\text{peak}}}{\Delta z} \right)^2 \right] \tag{6.3}$$

A symmetric HF heat source is a simplification but would in the case of noisy data reduce the risk of overfitting. However, it would be better, and possible, to conserve the two-sided Gaussian while also reducing the size of the parameter space. This could be done by assuming that the half-widths Δz_U and Δz_D can both be expressed by the same half width Δz and scaled by two known factors α and β. This results in an alternative heat source $Q_{\text{HF, }\alpha\beta}$.

$$Q_{\text{HF},\alpha\beta}(z) = Q_{\text{peak}} \exp -\zeta^2_{\alpha\beta} \tag{6.4}$$

where

$$\zeta_{\alpha\beta} = \begin{cases} (z - z_{\text{peak}})/\alpha\Delta z & z > z_{\text{peak}} \\ (z - z_{\text{peak}})/\beta\Delta z & z \leq z_{\text{peak}} \end{cases} \tag{6.5}$$

where the factors α and β could be decided by previously done estimates for Q_{HF} in similar conditions. Forcing the half-widths to be related by α/β, e.g. with $\alpha = 0.5$ and $\beta = 2$, would also solve the issue of steep gradients in the heat sources, like some of the heat sources shown in the left column in Figure 6.7.

However, we believe that the analysis with the parameter space used in this analysis is a good method that would have performed well in the case of less noisy data. This is clear from the difference between the left and right columns in Figure 6.7. The method performs better with higher enhancements in the observed temperatures. Higher enhancements could be achieved with a higher ERP. This would be possible if the ionospheric conditions would allow us to conduct our experiments around the fourth double resonance with Array 1 of the heating facility (shown in Figure 3.1) in October 2021. The conditions in March 2022 were good with an F-layer critical frequency foF_2 of over 6 MHz which means that Array 1, which has a minimum frequency of 5.3 MHz could have been used. However, due to technical difficulties only a small number of rows in Array 1 were operational during the experiment, and Array 2 was used instead. When using Array 1 the maximum theoretical ERP is 1200 MW which is significantly larger than the maximum ERP in our experiments which was 258 MW. In addition, a lower D-region absorption would lead to higher enhancements as more of the pump wave power reach the UHR altitude.

6.4 Frequency dependence analysis

In this section the analysis of the frequency dependence of the parameters when sweeping the pump frequency up and down is finally presented. A total of 52 modeled heat sources were used in the analysis, 28 where the HF pump frequency is stepped upwards and 24 where the HF pump frequency is stepped downwards. The heat sources used in the analysis are first and foremost heat sources from pulses where we have visible temperature enhancements in the EISCAT measurements. Further, acceptable models were selected through visual inspection of the modeled temperatures against the corresponding observed temperatures. Pulses where it was apparent that the modeling and parameter search were unsuccessful were omitted in the analysis.

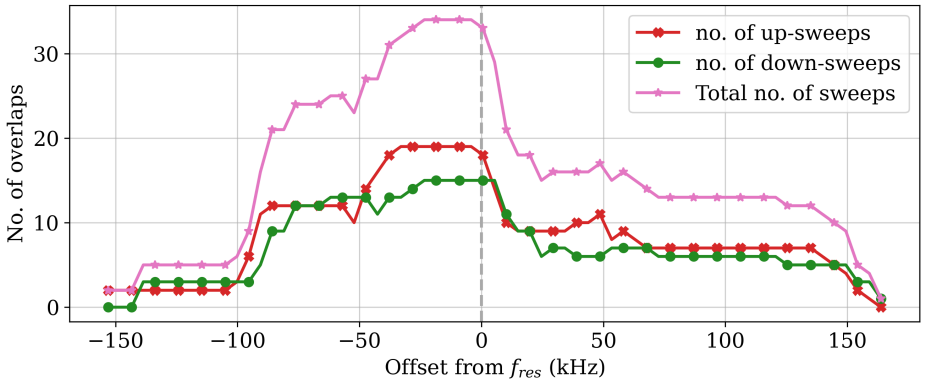

Figure 6.19: Number of overlapping sweeps as a function of frequency offset from the third double resonance frequency f_{res}.

Figure 6.19 show the number of overlapping sweeps per frequency as a function of frequency offset from the third double resonance frequency. It is clear that we have approximately the same number of up-sweeps and down-sweeps data points per frequency, with only a minor predominance of up-sweeps. It is also interesting and important to note that the number of overlapping sweeps drastically decrease just above the double resonance. The rapid decrease can be explained by the experiment design. In the SEE spectrogram excerpts (section 4.2) we see that we often pass the double resonance very early or late in a pulse. It is clear that in the pulses used in the analysis we have a high number of pulses where the double resonance frequency is likely passed in the highest frequency part of the pulse. This skewness is unfortunate as it would be ideal to have the same number of data points both above and below the double resonance frequency. However, we note that we have at least thirteen data points at all frequencies within an interval of 200 kHz around the double resonance. This should be enough to show possible indications of asymmetry.

6.4.1 Frequency dependence of Q_{column}

First the results of the analysis of the frequency dependence of Q_{column} when sweeping the frequency up and down is presented. Figure 6.20 shows two-dimensional histograms of the column integrated heating rates as a function of frequency offset for down-sweeps (green), and up-sweeps (red). As expected, we see clear minima in the column integrating heating rate as the pump frequency pass the double resonance frequency. The means of each frequency bin are traced in purple. The minima at zero offset from the double resonance frequency is also possible to see from these means, even though the variances

are large. Though characterized by noise, a possible trend might be traced over the histograms. These trends are shown as dashed lines in Figure 6.20 and cover approximately 99 % of max(Q_{column}). It is important to note that the trends in the histograms are ambiguous, especially below 0 offset during up-sweeps. However, the traces presented in Figure 6.20 represent two possible interpretations.

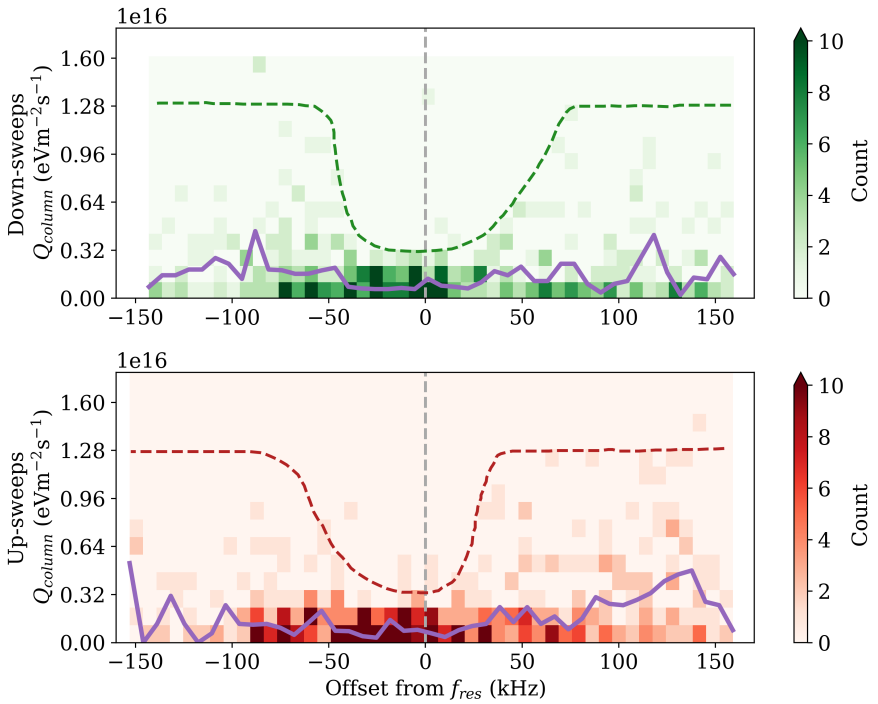

Figure 6.20: 2D histograms of column integrated heating rates as a function of offset from the third double resonance frequency. The top panel shows the histogram for down-sweeps and the bottom panel shows the histogram for up-sweeps. The dashed line shows an indication of the trend in Q_{column} as the pump frequency pass the double resonance frequency. The purple lines show the mean of each frequency bin. Note that the higher counts in the bottom left part of each histogram is explained by the higher number of overlapping sweeps in this frequency region.

The traces for up-sweeps and down-sweeps are presented in Figure 6.21. First and foremost, the traces are asymmetric with frequency. Also, the traced curves are not symmetric around zero frequency offset. It is seemingly wider below than above the double resonance frequency. Second, for both up-sweeps and down-sweeps Q_{column} is reduced by approximately 85 % at the minima. A reduction of 85 % in Q_{HF} indicates that at least 85 % of the total heating

is resonant heating. This is a larger percentage than found by Bryers et al. [6] who found that resonant heating is at most 5 times larger than the non-resonant heating (see section 2.3.2). However, Gustavsson et al. [16] found that the column integrated heating rate is reduced by approximately 90 % when the pump frequency is close to the third double resonance.

Interestingly, the curve for the up-sweeps is steeper above the double resonance frequency than the curve for the down-sweeps. Below the double resonance frequency, the curve for the down-sweeps is steepest. This possible indication means that the heating decreases slowly toward zero offset from the double resonance, while the heating increases rapidly after passing zero offset.

This possible trend might be counter intuitive. A possible naive expectation would be for the trend to be opposite. After passing the double resonance, one would expect a slower increase in heating as the striations increase gradually until saturation is reached. Likewise, one would expect a strong decrease in the heating when we approach zero offset, as UH waves no longer are excited, and the striations disappear. The opposite of our possible trend was seen in Honary et al. (1995) [18]. The increase in the anomalous absorption of the heater wave, which is linked to resonant heating, is steeper for down-sweeps than for up-sweeps above zero offset from the double resonance frequency.

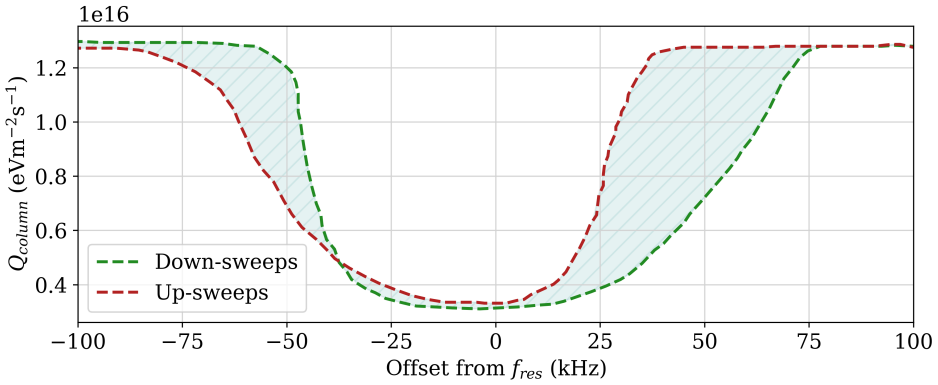

Figure 6.21: Traces of the shapes of Q_{column} from Figure 6.20 for up-sweeps (red) and down-sweeps (green).

However, the trend of a steeper increase when passing the double resonance is experimentally observed by Carozzi et al. [8] in the BUM intensity when sweeping the pump frequency up and down through the fourth double resonance. Comparing the BUM intensity above the double resonance frequency, they observed that the intensity for up sweeps were consistently higher than for down-sweeps. This matches what we see in the traces of the column inte-

grated heat sources in Figure 6.21 above $f_{\text{pump}} - f_{\text{res}} = 0$. They suggest that an explanation for the observed hysteresis effect is differences in how striations in the electron density are generated slightly above and below the double resonance frequency. These differences also lead to differences in the anomalous absorption. It is also of interest to mention that the hysteresis effects observed by Carozzi et al. were visible within an $\approx$ 40 KHz interval. Our interval is $\approx$ 75 KHz wide. This can be explained by the fact that we are sweeping through the third double resonance frequency instead of the fourth double resonance frequency. As discussed in section 2.3.5 the size of the forbidden regions in the dispersion relation solution spaces for UH and EB waves decrease in size with increasing harmonic number n. This means that it is reasonable to except a larger interval around the third double resonance.

The same hysteresis effect in BUM strength when sweeping the HF pump frequency up and down through the fourth double resonance frequency was also observed by Najmi et al. in 2014 [28]. They suggest that the hysteresis effect in BUM can be explained by large-scale striations in the electron density that will scatter the pump wave.

The high level of noise in the data used in the analysis results in likely overfitted parameters. Also, our parameters show sign of randomness, which is most prominent in the correlation matrices (section 6.3.1) and distribution of half-widths (section 6.3.3). Because of this we cannot draw a solid conclusion from the traced curves in Figure 6.21. Our enhancements in T_e are not large compared to $\sigma(T_e)$ which means that the relative uncertainties in our parameters are larger than what they would be for a more successful experiment. This means that our possible trends are not especially statistically significant. However, the differences Q_{column} for up-sweeps and down-sweeps provide a possible indication that there might be hysteresis effects in electron heating when sweeping the pump frequency up and down, namely that the column integrated heating rate is consequently larger for up-sweeps than for down sweeps above the double resonance. At the very least, the possibly observed trends does not rule out the possibility of asymmetry and hysteresis effects in electron heating around the third double resonance frequency.

6.4.2 Frequency dependence of w_{tot} and z_{COH}

Because it is difficult to see unambiguous trends in Q_{col} around the double resonance, the frequency dependence analysis was repeated for two parameters separately, namely the center of heating z_{coh} and the total width w_{tot}. These two parameters are chosen because they are better representations of the shape of the heat sources, rather than z_{peak} and half-widths Δz_D and Δz_U. This is explained in section 6.3.3.

Figure 6.22 shows histograms of z_{coh} for down-sweeps and up-sweeps. As expected, z_{coh} is typically around 200 km. This matches the altitudes of the observed temperature enhancements (section 4.1). These histograms are also characterized by noise, but we see some possible trends. The first trend of note is the widths of the distributions for z_{coh} when sweeping the pump frequency down through the double resonance frequency. Though vague, it seems that the distribution is most narrow just above the double resonance. It also seems that the distribution is widening when $f_{\text{pump}} - f_{\text{res}} \gtrapprox 60$ kHz. Below the double resonance the distribution maintains its width up until the double resonance, widening only slightly around $f_{\text{pump}} - f_{\text{res}} \approx -50$ kHz.

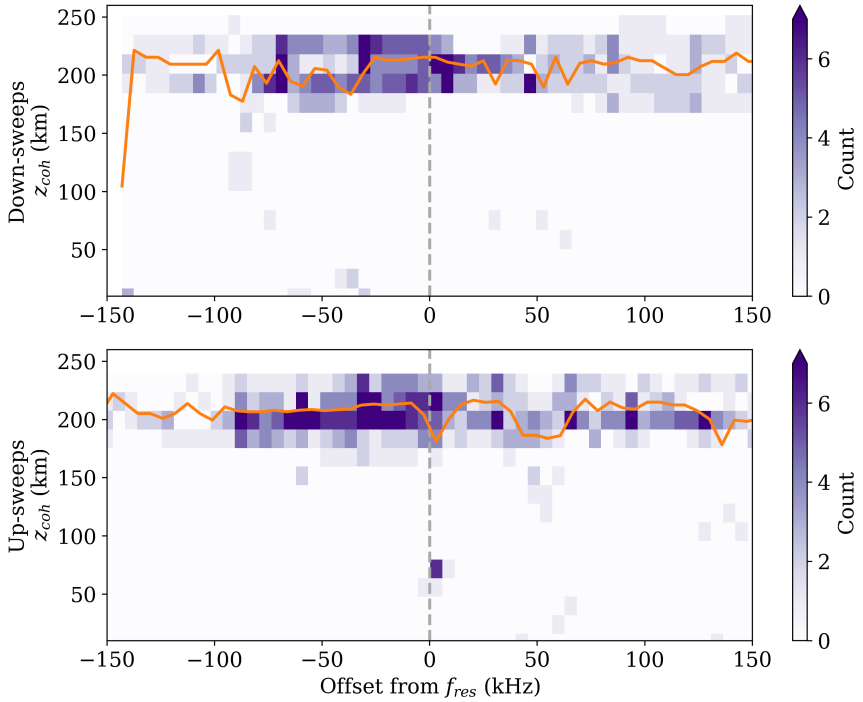

Figure 6.22: Histograms of z_{coh} as a function of frequency offset from the third double resonance f_{res}. Note that the higher counts in the left part of each histogram is explained by the higher number of overlapping sweeps in this frequency region.

The distribution for z_{coh} when sweeping the pump frequency up through the double resonance frequency is seemingly different. We note no clear narrowing of the distribution around the double resonance. Also, the width of the distribution is approximately equal above and below the double resonance apart from a slight possible widening on the interval $f_{\text{pump}} - f_{\text{res}} \in [-50, 0]$ kHz. It is also interesting to note that we have a highly concentrated point at

approximately 75 km where $f_{\text{pump}} \approx f_{\text{res}}$, or just above. The histograms for both up-sweeps and down-sweeps have some outlying points, but it is interesting that this specific point have such a high count. However, we can assume that this higher concentration of outliers is simply a coincidence.

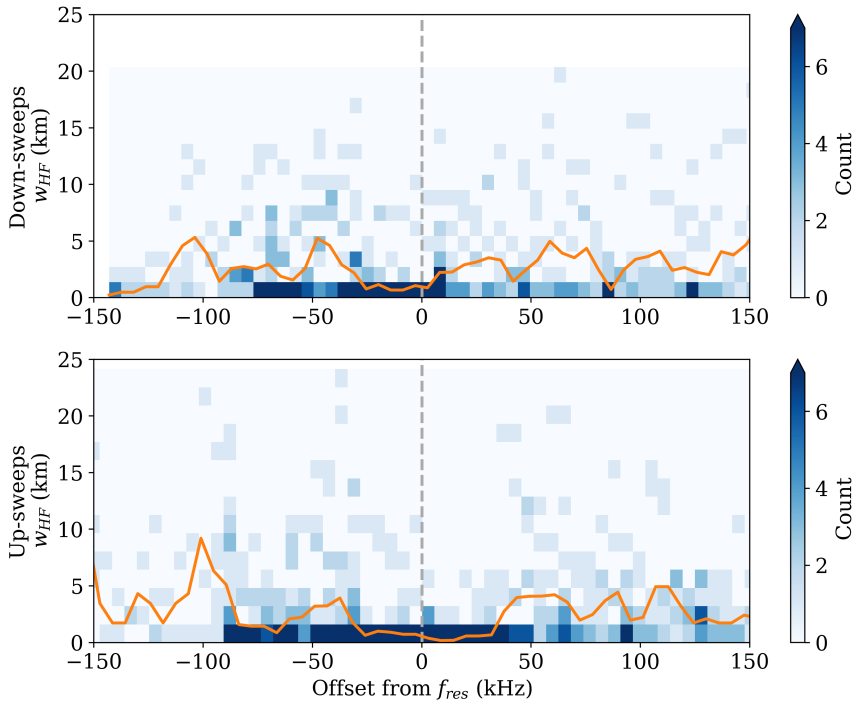

Figure 6.23: Histograms of w_{HF} as a function of frequency offset from the third double resonance f_{res}. Note that the higher counts in the bottom left part of each histogram is explained by the higher number of overlapping sweeps in this frequency region.

Corresponding histograms for the total heat source width w_{HF} are shown in Figure 6.23. Again, we cannot draw conclusions from these histograms. However, we can see some indications of possible trends in w_{HF} when the pump frequency passes the double resonance frequency from below and above. First and foremost, the distributions for w_{HF} are widespread and it is difficult to distinguish possible patterns from the noisy distributions. However, there is an indication that the distribution narrows above $f_{\text{pump}} - f_{\text{res}} = 0$ for up-sweeps. This means that the total width of the HF heat source might decrease when the double resonance is passed from below, before w_{HF} is allowed to increase again. This narrowing cannot be seen in the down-sweeps. For the up-sweeps we also see that the distribution is narrow for offsets $f_{\text{pump}} - f_{\text{res}} > 100$ kHz, whereas the same trend cannot be seen for the down-sweeps.

The same possible trends are possible to see from the means, plotted in orange over the histograms. We clearly see a symmetric minimum around zero offset for up-sweeps. The minimum is approximately 70 kHz wide. For down-sweeps the minimum is smaller, and only below zero offset. This further indicate that the HF heat-source only narrows below the double resonance when sweeping the frequency down while it does not narrow significantly above the double resonance frequency. However, for up-sweeps, the HF heat source narrows significantly some time before passing the double resonance, and it stay narrow for some time after passing the double resonance. Again, due to the high variances the possible trends are not statistically significant, but they do not rule out the possibility of these trends existing in the electron heating when passing the third double resonance frequency.

7

Summary and conclusion

For this thesis three EISCAT Heating experiments were performed to investigate the frequency dependence of ionospheric electron heating around the third double resonance frequency when stepping the pump frequency up and down. The third double resonance frequency was passed in both up-sweeps and down-sweeps in all three experiments. We observed electron temperature enhancements up to 2000 K above background temperatures, clearly variable with frequency. A fourth experiment was conducted with the intent to investigate the frequency dependence of ionospheric electron heating when sweeping the pump frequency up through the third and fourth double resonance frequencies. Unfortunately, this experiment was unsuccessful, and it was therefore omitted from the analysis done for this thesis.

The ionospheric electron heating during the three experiments was modeled by assuming parameterizations for the background heat source and the HF pump heat source. The parameters for these parameterizations were found iteratively by integrating the electron energy equation for $\tilde{T}_e$ and minimizing the error between $\tilde{T}_e$ and the observed T_e through non-linear squares minimization. This minimization was first performed for HF OFF periods under the assumptions of steady state. Further, the parameters of the HF heat sources were found for each five second step into each HF ON period, consequently matching the frequency steps in the observations. The fitted heat sources typically produced acceptable matches to the observed temperatures when solving the electron energy equation with the fitted parameters.

Unfortunately, the experiment data had a high noise level. This is because the F-layer critical frequency $foF2$ were too low for Array 1 to be used, and Array 2 which has a lower ERP was used instead. The D-region density varied during our experiments, leading to absorption of the pump wave during parts of our experiments. The high noise level in our experiment data lead to our fitted parameters being influenced by the noise. This means that our parameters do not necessarily explain the ionospheric heating during our experiments well. This unfortunately means that we cannot draw any conclusions from our model, as the variances are large and statistical significance of our analysis results is therefore questionable.

Finally, the frequency dependence was investigated in the column integrated heating rates, and also for parameters w_{HF} and z_{coh} separately. Although we cannot confidently say that our parameters and models accurately explain the ionospheric heating during our experiment due to the high variances and noise influence, we note some possible trends as a function of frequency swept through the third double resonance frequency from below and above. These indications include possible asymmetry in the column integrated heating rates, namely that the slope of Q_{column} is steepest below f_{res} for down-sweeps and steepest for up-sweeps above f_{res}. Above the double resonance frequency the column integrated heat rates for up-sweeps where larger than the heat rates for down-sweeps. This possible hysteresis effect matches the hysteresis effect found in BUM strength when sweeping the frequency up and down though the fourth double resonance, illustrated by Carozzi et al. in 2002 [8] and Najmi et al. in 2014 [28]. Second, we see indications that the distribution of z_{coh} possibly widen above f_{res} during down-sweeps, but not during up-sweeps. Third, we note slight indications that the total width w_{HF} have a possibly symmetric minima around f_{res} during up-sweeps, while the minima can only be seen below f_{res} during down sweeps.

7.1 Future work

First and foremost, the experiment done in October 2021 could be repeated around the fourth double resonance frequency. This would allow us to use Array 1 of the EISCAT Heating facility. Using Array 1 would result in a significantly larger ERP which means that the enhancements in temperature would be more easily separated from the noise in the measurements. This would hopefully result in less ambiguous analysis results and could therefore either confidently confirm or contradict the possible trends in the frequency dependence of ionospheric electron heating indicated in this work. Repeating the sweep-experiments around the fourth double resonance would also give grounds for investigating possible differences in the frequency dependence of ionospheric

electron heating around the third and fourth double resonance frequencies, which unfortunately was unsuccessful in March 2022.

Another aspect of the ionospheric electron heating around the third double resonance could also be investigated with the type of experiment done for this thesis but was omitted from the analysis. Because the sweeps are overlapping, the HF pump frequency passes the third double resonance at different times into each pulse. This gives ground for investigating the dependence on the pulse duration before passing the double resonance frequency. This could possibly be analyzed using the data from the experiments detailed in this thesis.

Bibliography

[1] Akbari, H., LaBelle, L. W., Newman, D. L. Langmuir turbulence in the auroral ionosphere: Origins and effects. *Frontiers in Astronomy and Space Sciences*, 7, 2021.

[2] Ashrafi, M., Kosch, M. J., Honary, F. Heater-induced altitude decent of the EISCAT UHF ion line enhancements: Observations and modelling. *Advances in Space Research*, 38(11):2645–2652, 2006.

[3] Bittencourt, J. A. *Fundamentals of Plasma Physics*. Springer Science + Business Media, 2004. ISBN: 978-1-4419-1930-4.

[4] Bjørnå, N. *Lecture notes in AGF-304 Radar diagnostic of space plasma*.

[5] Brekke, A. *Physics of the Upper Polar Atmosphere*. Springer+Praxis, 2013. ISBN: 978-3-642-27400-8.

[6] Bryers, C. J., Kosch, M., Senior, A., Rietveld, M., and Singer, W. A comparison between resonant and nonresonant heating at EISCAT. *Journal of Geophysical Research: Space Physics*, 118:6766–6776, 2013.

[7] Bryers, C., Kosch, M., Senior, A., Rietveld, M., and Yeoman, T. EISCAT observations of pump-enhanced plasma temperature and optical emission excitation rate as a function of power flux. *Journal of Geophysical Research: Space Physics*, 117(A9), 2012.

[8] Carozzi, T. D., Thidé, B., Grach, S. M., Leyser, T. B., Holz, M., Komrakov, G. P., Frolov, V. L., and Sergeev, E. N. Stimulated electromagnetic emissions during pump frequency sweep through fourth electron cyclotron harmonic. *Journal of Geophysical Research*, 107(A9), 2002.

[9] Chen, Francis F. *Introduction to Plasma Physics and Controlled Fusion. Volume 1: Plasma Physics*. Springer Science + Business Media, 1984. ISBN:978-1-4419-3201-3.

[10] NASA Community Coordinated Modeling. Dgrf/igrf geomagnetic field model 1945 - 2025 (igrf-13) and related parameters. https://ccmc.gsfc.nasa.gov/modelweb/models/igrf_vitmo.php, Last accessed: 27.02.22.

[11] NASA Community Coordinated Modeling. International reference ionosphere - iri (2016) with igrf-13 coefficients. https://ccmc.gsfc.nasa.gov/modelweb/models/iri2016_vitmo.php, Last accessed: 03.05.22.

[12] NASA Community Coordinated Modeling. Msis-e-90 atmosphere model. https://ccmc.gsfc.nasa.gov/modelweb/models/msis_vitmo.php, Last accessed: 03.05.22.

[13] Farley, D. T. and Hagfors, T. Unpublished manuscript, 1999.

[14] Grach, S.M., Thidé, B., and Leyser, T. B. Plasma waves near the double resonance layer in the ionosphere. *Radiophysics and Quantum Electronics*, 37(5), 1994.

[15] Gustavsson, B., Leyser, T. B., Kosch, M., Rietveld, M. T., Steen, Å ., Brändström, B. U. E., and Aso, T. Electron Gyroharmonic Effects in Ionization and Electron Acceleration during High-Frequency Pumping in the Ionosphere. *Physical Review Letters*, 97, 2006.

[16] Gustavsson, B., Rexer, T., Vierinen, J., Leyser, T. B., Grydeland, T., Rietveld, M. T., McKay, D., Floer, M. Rise and fall of electron temperatures: variation of ionospheric electron-heating by HF radio wave pumping around the third double resonance. Unpublished manuscript.

[17] Gustavsson, B., Rietveld, M. T., Ivchenko, N. V., and Kosch, M. J. Rise and fall of electron temperatures: Ohmic heating of ionospheric electrons from underdense HF radio wave pumping. *Journal of Geophysical Research*, 115, 2010.

[18] Honary, F., Stocker, A. J., Robinson, T. R., Jones, T. B., and Stubbe, P. Ionospheric plasma response to HF radio waves operating at frequencies close to the third harmonic of the electron gyrofrequency. *Journal of Geophysical Research*, 100:21489–21501, 1995.

[19] Jones, T. B. and Robinson, T. A hysteresis effect in the generation of field-aligned irregularities by a high-power radio wave. *Radio Science*, 18(6):835–839, 1983.

[20] Kosch, M., Gustavsson, B., Heinselman, C., Pedersen, T., Rietveld, M., Spaleta, J., Wong, A., Wang, W., Mutiso, C., Bristow, B., and Hughes, J.

First incoherent scatter radar observations of ionospheric heating on the second electron gyro-harmonic. *Journal of Atmospheric and Solar-Terrestrial Physics*, 71(17-18):1959–1966, 2009.

[21] Leyser, T. B. Stimulated Electromagnetic Emissions by High-Frequency Electromagnetic Pumping of the Ionospheric Plasma. *Space Science Reviews*, 98:223–328, 2001.

[22] Leyser, T. B., Gustavsson, B., Rexer, T., and Rietveld, M. T. The dependence of F-region electron heating on HF radio pump power: Measurements at EISCAT Tromsø. *Annales Geophysicae*, 38(5):297–307, 2020.

[23] Leyser, T.B. *Stimulated Electromagnetic Emissions in the Ionosphere*. PhD thesis, Swedish Institute of Space Physics, Uppsala Division, September 1989.

[24] Lieberman, Michael J. and Lichtenberg, Allan J. *Principles of Plasma Discharges and Materials Processing*. John Wiley & Sons, Ltd, 2005. ISBN: 0-471-72001-1.

[25] Lihtinen, Markku S. and Huuskonen, Asko. General incoherent scatter analysis and GUISDAP. *Journal of Atmospheric and Solar-Terrestrial Physics*, 58(1-4):435–452, 1996.

[26] Lofös, H., Ivchenko, N., Gustavsson, B., Leyser, T.B. and Rietveld, M.T. . Underdense F-region heating by X-mode. 2008.

[27] Najmi, A., Eliasson, B., Shao, X., Milikh, G., Sharma, A. S., and Papadopoulos, K. Vlasov simulations of electron acceleration by radio frequency heating near the upper hybrid layer. *Physics of Plasmas*, 24(102904), 2017.

[28] Najmi, A., Milikh, G., Secan, J., Chiang, K., Psiaki, M., Bernhardt, P., Briczinski, S., Siefring, C., Chang, C. L., Papadopoulos, K. Generation and detection of super small striations by F region HF heating. *Journal of Geophysical Research: Space Physics*, 119:6000–6011, 2014.

[29] Rexer, Theresa. *Radio wave propagation through the ionosphere: Plasma experiments at the topside ionosphere*. PhD thesis, UiT Arctic University of Norway, September 2021.

[30] Rietveld, M. Eiscat's ionospheric heating facility including dynasonde. `https://www.eiscat.uit.no/html/heater.html`, Accessed: 25.03.22.

[31] Rietveld, M., Kosch, M., Blagoveshchenskaya, N., Kornienko, V., Leyser,

T., and Yeoman, T. Ionospheric electron heating, optical emissions and striations induced by powerful HF radio waves at high latitudes: Aspect angle dependence. *Journal of Geophysical Research*, 108(A4), 2003.

[32] Robinson, T. R. The excitation of plasma waves and irregularities in the ionosphere by means of high power radio waves. *Plasma Physics and Controlled Fusion*, 30(1):45–56, 1988.

[33] Robinson, T. R., Honary, F., Stocker, A. J., Jones, T. B. and Stubbe, P. First EISCAT observations of the modification of F-region electron temperatures during RF heating at harmonics of the electron gyro frequency. *Journal of Atmospheric and Terrestrial Physics*, 58(1-4):385–395, 1996.

[34] Schunk, Robert and Nagy, Andrew. *Ionospheres: Physics, Plasma Physics, and Chemistry*. Cambridge Atmospheric and Space Science Series. Cambridge University Press, 2. edition, 2009. ISBN: 978-1-108-46210-5.

[35] Senior, A., Rietveld, M., Yeoman, T., and Kosch, M. The dependence of F-region electron heating on HF radio pump power: Measurements at EISCAT Tromsø. *Journal of Geophysical Research*, 117, 2012.

[36] Shoucri, M. M., Morales, G. J., and Maggs, J. E. Ohmic heating of the polar F region by HF pulses. *Journal of Geophysical Research*, 89:2907–2917, 1984.

[37] NOAA Space Weather Prediction Center. Solar cycle progression. `https://www.swpc.noaa.gov/products/solar-cycle-progression`, Accessed: 03.05.22.

[38] Theodoridis, S. and Koutroumbas, K. *Pattern Recognition (fourth edition)*. Academic Press, 2009. ISBN: 978-1-59749-272-0.

[39] Wright, D. M., Davies, J. A., Yeoman, T. K., Robinson, T. R., Shergill, H. Saturation and hysteresis effects in ionospheric modification experiments observed by the CUTLASS and EISCAT radars. *Annales Geophysicae*, 24:543–553, 2014.